

JPL Publication 96-4, Vol. 2

# Summaries of the Sixth Annual JPL Airborne Earth Science Workshop March 4–8, 1996

Volume 2. AIRSAR Workshop

Yunjin Kim  
Editor

March 4, 1996



National Aeronautics and  
Space Administration

Jet Propulsion Laboratory  
California Institute of Technology  
Pasadena, California

JPL Publication 96-4, Vol. 2

# Summaries of the Sixth Annual JPL Airborne Earth Science Workshop March 4–8, 1996

Volume 2. AIRSAR Workshop

Yunjin Kim  
Editor

March 4, 1996



National Aeronautics and  
Space Administration

Jet Propulsion Laboratory  
California Institute of Technology  
Pasadena, California

This publication was prepared by the Jet Propulsion Laboratory, California Institute of Technology, under a contract with the National Aeronautics and Space Administration.

Reference herein to any specific commercial product, process, or service by trade name, trademark, manufacturer or otherwise, does not constitute or imply its endorsement by the United States Government or the Jet Propulsion Laboratory, California Institute of Technology.

## ABSTRACT

This publication contains the summaries for the Sixth Annual JPL Airborne Earth Science Workshop, held in Pasadena, California, on March 4–8, 1996. The main workshop is divided into two smaller workshops as follows:

- The Airborne Visible/Infrared Imaging Spectrometer (AVIRIS) workshop, on March 4–6. The summaries for this workshop appear in Volume 1.
- The Airborne Synthetic Aperture Radar (AIRSAR) workshop, on March 6–8. The summaries for this workshop appear in Volume 2.



**Page intentionally left blank**

## TABLE OF CONTENTS

Determination of the Optimal Polarimetric Contrast Enhancement (OPCE) Coefficient from the 2 x 2 Coherent Sinclair [S] and the Partially Coherent 4 x 4 Kennaugh [K] Matrices and Its Interpretation in Terms of the Polarimetric Entropy Coefficients (PEC: $H/A/\alpha$ ) in POL-SAR Image Analysis.....	1
<i>Wolfgang-M. Boerner, Harold Mott, Mitsuro Tanaka, and Yoshio Yamaguchi</i>	
On Soil Moisture Retrieval and Target Decomposition.....	3
<i>Pascale C. Dubois and Jakob van Zyl</i>	
Repeat Pass Aircraft Interferometry Results at Portage Lake, Maine and Innisfail, Australia .....	9
<i>Scott Hensley, Jeff Klein, Paul Rosen, Elaine Chapin, Søren Madsen, and Frank Webb</i>	
Geocoding of AIRSAR/TOPSAR SAR Data .....	35
<i>Francesco Holecz, Yunling Lou, and Jakob van Zyl</i>	
Measurement of Ocean Surface Slope by AIRSAR .....	43
<i>J.S. Lee and D. L. Schuler</i>	
The NASA/JPL Airborne Synthetic Aperture Radar System.....	51
<i>Yunling Lou, Yunjin Kim, and Jakob van Zyl</i>	
On the Capabilities of Using AIRSAR Data in Surface Energy/Water Balance Studies.....	57
<i>Jose F. Moreno and Sasan S. Saatchi</i>	
An Automated Mapping Processor Using C-Band Interferometric SAR Data .....	67
<i>E. Rodriguez, T.R. Michel, J.M. Martin, and B. Houshmand</i>	
First Results of the TOPSAR C-Band/L-Band Interferometer: Calibration and Differential Penetration .....	77
<i>Paul A. Rosen and Scott Hensley</i>	
Measurements of Ocean Features with AIRSAR.....	91
<i>David Sheres and Walt Osterman</i>	
Estimation of Local Incident Angles for Bare Surface Using Only SAR Measurements and Its Applications .....	93
<i>Jiancheng Shi and J. Dozier</i>	
Modeling Wetland Vegetation Using Polarimetric SAR.....	95
<i>K. Clint Slatton, Melba M. Crawford, James C. Gibeaut, and Roberto O. Gutierrez</i>	

## TABLE OF CONTENTS (continued)

AIRSAR Data for Geological and Geomorphological Mapping in the Great Sandy Desert and Pilbara Regions of Western Australia .....	105
<i>Ian J. Tapley</i>	
Improved Regolith-Landform and Geological Mapping Using AIRSAR Data as an Aid to Mineral Exploration in the North-Eastern Goldfields Region, Western Australia .....	107
<i>Ian J. Tapley</i>	
Performance of Polarimetric Processing Techniques Using NAWC P-3 SAR Imagery .....	109
<i>J.G. Teti, Jr., R. R.-Y. Lee, J. S. Verdi, and W.-M. Boerner</i>	
The Information Content of Interferometric Synthetic Aperture Radar: Vegetation and Underlying Surface Topography .....	111
<i>Robert N. Treuhaft</i>	
Wideband Interferometric Sensing and Imaging Polarimetry—and Its Relevance to Wide Area Military Surveillance and Environmental Monitoring of the Terrestrial and Planetary Covers.....	119
<i>James Salvatore Verdi, Otto Kessler, and Wolfgang-Martin Boerner</i>	
GeoSAR: A Radar-Based Terrain Mapping Project.....	121
<i>Robert Yoha</i>	

**DETERMINATION OF THE OPTIMAL POLARIMETRIC CONTRAST ENHANCEMENT (OPCE) COEFFICIENT FROM THE 2x2 COHERENT SINCLAIR [S] AND THE PARTIALLY COHERENT 4x4 KENNAUGH [K] MATRICES AND ITS INTERPRETATION IN TERMS OF THE POLARIMETRIC ENTROPY COEFFICIENTS (PEC:  $H/A/\alpha$ ) IN POL-SAR IMAGE ANALYSIS**

**Wolfgang-M. Boerner<sup>1</sup>, Harold Mott<sup>2</sup>, Mitsuro Tanaka<sup>3</sup> and Yoshio Yamaguchi<sup>4</sup>**

1. UNIVERSITY OF ILLINOIS AT CHICAGO, UIC-EECS/CSN, M/C 154  
CHICAGO, IL / USA 60607-7018, T&F: +[1](312)996-5480
2. UNIVERSITY OF ALABAMA AT TUSCALOOSA, UAT-ECE,  
TUSCALOOSA, AL / USA 35487-0286, T/F: +[1](205)348-1759/6959
3. UNIVERSITY OF OITA in KYUSHU, UO-ECE/ISL,  
OITA, KYUSHU, JAPAN 870-11, T/F: +[81](975)69-3111 x796/67-2790
4. NIIGATA UNIVERSITY, NU-ENG.COL.-INFO.ENG.,  
NIIGATA-SHI, JAPAN 950-21, T&F: +[81](25)262-6752

In polarimetry strict distinction must be made between optical polarimetry, defined for the forward propagation case in terms of the Jones/Mueller matrix calculus, versus radar polarimetry, defined for the (back)scattering case in terms of the Sinclair/Kennaugh matrix formulations. In this analysis, the optimal polarimetric contrast between a desirable (target) and undesirable (clutter) scattering feature is determined for radar polarimetry for which it is often desirable to select radar antenna polarization that maximize the contrast in received powers from such two distinct classes of scatterers. For example, a terrain-mapping POL-SAR imager may use polarization state manipulations to maximize the contrast between forested areas and farmland, whereas in a combined TOP-POL-SAR ↔ POL-MTI imager, the polarization states may be chosen to optimize the "stealthy" aircraft target return relative to heterogeneous dense, dynamically changing background clutter. The fixed antenna polarization of such systems chosen for contrast optimization for either purpose may result in a target return that is small compared to external noise or internal receiver noise, clutter and speckle; and it may therefore be more appropriate to determine in a real-time image data take post-processing mode the polarization(s) that maximize(s) the signal-to-noise and its ratio with respect to speckle and clutter. A complete analysis of methods for the Sinclair [S], the Graves [G] and the Kennaugh [K] matrices is provided for all of the scattering scenarios discussed here. Also, it is shown why such a procedure applied to the covariance matrices [ $\Sigma^{3,4}$ ] for either the three(3)-dimensional reciprocal symmetric or the four (4)-dimensional bistatic (non-reciprocal) case is not useful; and that a group-theoretic expansion in terms of the "canonical eigenvalues" of the covariance matrix will instead provide the closely associated Polarimetric Entropy Coefficients (PEC  $H/A/\alpha$ ) of Cloude. Specifically, it is demonstrated that with the prior implementation of Cloude's PEC (Polarimetric entropy  $H$ , polarimetric anisotropy  $A$ , derived from the eigenvalues of [ $\Sigma$ ], and the polarimetric canonical target phase  $\alpha$  derived from the associated eigenvectors), it is possible to specify which class of OPCE coefficients is the most effective one for truly optimal contrast enhancement. Various examples utilizing most recent image data take sets of the NAWC/ERIM-P3-UWB-TOPIF'E-POLSAR and the NASA-JPL-AIRSAR, as well as the NASA/DARA/DASI-SIR-C/X-SAR shuttle imaging systems will be presented for demonstrating the utility of the PEC and OPCE concepts in POL-SAR image analysis.

**Page intentionally left blank**

# ON SOIL MOISTURE RETRIEVAL AND TARGET DECOMPOSITION

Pascale C. Dubois(\*,\*\*) and Jakob van Zyl(\*)

(\*): Jet Propulsion Laboratory, California Institute of Technology  
4800 Oak Grove Drive, Pasadena, CA 91109

(\*\*) Currently, visiting scientist with the Centre d'Etude des Environnements Terrestre et Planetaires, 78 Velizy, France

E-mail: Pascale.dubois@cetp.ispl.fr Ph: 0 11 33 1 39 25 49 35

## 1. INTRODUCTION

In an earlier study, an empirical model was developed to infer soil moisture and surface roughness from radar data [1]. The inversion technique was extensively tested over bare surfaces by comparing the estimated soil moisture to *in situ* measurements. The overall RMS error in the soil moisture estimate was found to be 3.5 % and the RMS error in the RMS height estimate was less than 0.35 cm absolute for bare or slightly vegetated surfaces. However, inversion results indicate that significant amounts of vegetation cause the algorithm to underestimate soil moisture and overestimate RMS height. Among the areas over which the inversion cannot be applied, the areas with intermediate vegetation cover are of particular interest as both the vegetation and the underlying bare surface affect the backscatter. This paper concentrates mostly on these areas. Using the full polarimetric information and the Cloude target decomposition approach [2], three different components of the target backscattering can be isolated. One of these three components can be identified as the surface component in the case of intermediate vegetation cover. Once the surface component of the scattering is isolated, the bare surface inversion can then be applied.

## 2. SOIL MOISTURE RETRIEVAL FOR BARE SURFACES

The soil moisture retrieval method presented in [1] relies on the two following equations describing the hh-polarized and vv-polarized backscattering coefficients  $\sigma_{hh}^o$  and  $\sigma_{vv}^o$  as a function of  $\theta$ , the incidence angle,  $\varepsilon$ , the real part of the dielectric constant,  $h$ , the Root Mean square (RMS) height of the surface,  $k$ , the wave number and  $\lambda$ , the wavelength in cm:

$$\begin{aligned}\sigma_{hh}^o &= 10^{-2.75 \frac{\cos \theta}{\sin \theta}^{1.5}} 10^{0.028 \varepsilon \tan \theta} (kh \sin \theta)^{1.4} \lambda^{0.7} \\ \sigma_{vv}^o &= 10^{-2.35 \frac{\cos \theta}{\sin \theta}^3} 10^{0.046 \varepsilon \tan \theta} (kh \sin \theta)^{1.1} \lambda^{0.7}\end{aligned}\tag{1}$$

The RMS height of the surface and the dielectric constant can easily be inverted from these two relations. Once the dielectric constant is known, the volumetric soil moisture can be computed using the Hallikainen curves [3] or the Brisco curves[4]. The inversion accuracy was extensively tested over a variety of sensors and sites as described in Figure 1. The overall RMS errors were found to be less than 0.4 cm in RMS height and 3.5% in soil moisture. The algorithm is optimized for bare surfaces and requires two co-polarized channels at a frequency between 1.5 GHz and 11 GHz. It gives best results for  $kh \leq 2.5$ ,  $\mu_v \leq 35\%$  and  $\theta \geq 30^\circ$ .

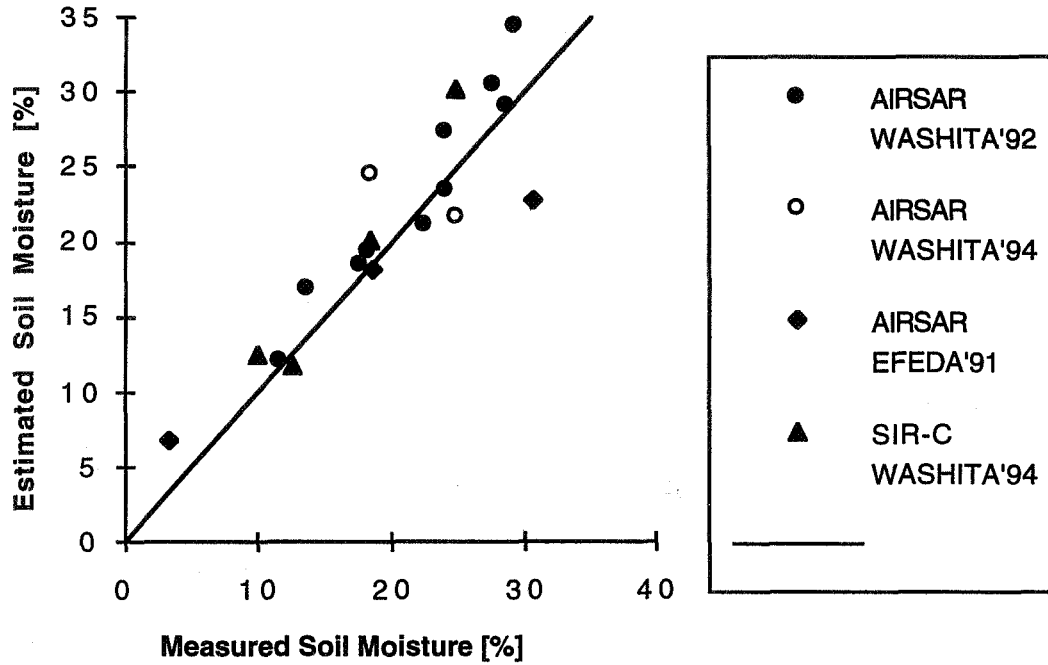


Figure 1: Radar derived soil moisture versus in situ measurements.

Omitting the usually weaker hv-polarized returns makes the algorithm less sensitive to system cross-talk and system noise, simplifies the calibration process and adds robustness to the algorithm in the presence of vegetation. However, inversion results indicate that significant amounts of vegetation ( $NDVI > 0.4$ ) cause the algorithm to underestimate soil moisture and overestimate RMS height. A simple criterion based on the  $\sigma_{hv}^0/\sigma_{vv}^0$  ratio was developed to select the areas where the inversion is not impaired by the vegetation. In the following paragraphs, we will present a way to estimate the soil moisture for surfaces with intermediate vegetation cover.

### 3. CLOUDE DECOMPOSITION

Cloude showed that a general covariance matrix  $[T]$  can be decomposed as follows:

$$[T] = \lambda_1 \bar{k}_1 \cdot \bar{k}_1^\dagger + \lambda_2 \bar{k}_2 \cdot \bar{k}_2^\dagger + \lambda_3 \bar{k}_3 \cdot \bar{k}_3^\dagger + \lambda_4 \bar{k}_4 \cdot \bar{k}_4^\dagger \quad (2)$$

In (2),  $\lambda_i$ ,  $i=1,2,3,4$  are the eigenvalues of the covariance matrix,  $\bar{k}_i$ ,  $i=1,2,3,4$  are the eigenvectors of  $[T]$ , and  $\bar{k}_i^\dagger$  means the *adjoint* (complex conjugate transposed) of  $\bar{k}_i$ . In the monostatic case, for reciprocal media, the covariance matrix has one zero eigenvalue and the decomposition results in at most three covariance matrices on the right-hand side of (2).

Also useful in our discussions later is Cloude's definition of target entropy,



$$H_T = \sum_{i=1}^4 -P_i \log_4(P_i) \quad \text{where} \quad P_i = \frac{\lambda_i}{\sum_{j=1,4} \lambda_j} \quad (3)$$

As pointed out by Cloude, the target entropy is a measure of target disorder, with  $H_T = 1$  for random targets and  $H_T = 0$  for simple (single) targets.

The covariance matrix for azimuthally symmetrical natural terrain in the monostatic case was shown [5] to follow the general form:

$$[T] = c \begin{pmatrix} 1 & 0 & \rho \\ 0 & \eta & 0 \\ \rho^* & 0 & \zeta \end{pmatrix} \quad \text{where} \quad (4)$$

$$c = \langle S_{hh} S_{hh}^* \rangle, \quad \rho = \frac{\langle S_{hh} S_{vv}^* \rangle}{\langle S_{hh} S_{hh}^* \rangle}, \quad \eta = \frac{2\langle S_{hv} S_{hv}^* \rangle}{\langle S_{hh} S_{hh}^* \rangle} \quad \text{and} \quad \zeta = \frac{\langle S_{vv} S_{vv}^* \rangle}{\langle S_{hh} S_{hh}^* \rangle} \quad (5)$$

The superscript \* means complex conjugate, and all quantities are ensemble averages. The parameters  $c$ ,  $\zeta$ ,  $\rho$  and  $\eta$  all depend on the size, shape and electrical properties of the scatterers, as well as their statistical angular distribution. It is easily shown that the eigenvalues of  $[T]$  are [6]

$$\lambda_1 = \frac{c}{2} \left( \zeta + 1 + \sqrt{(\zeta - 1)^2 + 4\rho\rho^*} \right) \quad (6)$$

$$\lambda_2 = \frac{c}{2} \left( \zeta + 1 - \sqrt{(\zeta - 1)^2 + 4\rho\rho^*} \right) \quad (7)$$

$$\lambda_3 = c\eta \quad (8)$$

Because  $[T]$  is a Hermitian matrix, the three eigenvalues are real and greater than zero.

The corresponding three eigenvectors are

$$\bar{k}_1 = \sqrt{\frac{(\zeta - 1 + \sqrt{\Delta})^2}{(\zeta - 1 + \sqrt{\Delta})^2 + 4\rho\rho^*}} \begin{pmatrix} \frac{2\rho}{(\sqrt{\Delta} + (\zeta - 1))} \\ 0 \\ 1 \end{pmatrix} \quad (9)$$

$$\bar{k}_2 = \sqrt{\frac{(\zeta - 1 - \sqrt{\Delta})^2}{(\zeta - 1 - \sqrt{\Delta})^2 + 4\rho\rho^*}} \begin{pmatrix} \frac{-2\rho}{(\sqrt{\Delta} - (\zeta - 1))} \\ 0 \\ 1 \end{pmatrix} \quad (10)$$

$$\bar{k}_3 = \begin{pmatrix} 0 \\ 1 \\ 0 \end{pmatrix} \quad (11)$$

where

$$\Delta = (\zeta - 1)^2 + 4\rho\rho^*. \quad (12)$$

The square root terms in front of the eigenvectors in (9-10) are there for normalization purposes and are always positive. We note that  $\Delta$  is positive and that  $\sqrt{\Delta}$  is always greater than  $|\zeta - 1|$ . Also note that we can write

$$\frac{k_{11}}{k_{21}} = -D \frac{(\sqrt{\Delta} - (\zeta - 1))}{(\sqrt{\Delta} + (\zeta - 1))} \quad (13)$$

where D includes the square-root factors in front of the vectors in (9, 10) and is therefore always positive. It is easy to see then that the ratio in (13) is always real and negative. This means that the first two eigenvectors represent scattering matrices that can be interpreted in terms of odd and even numbers of reflections when  $\text{Arg}(\rho)$  is close to zero. This is the case for scattering dominated by the surface scattering term.

#### 4. SOIL MOISTURE RETRIEVAL FOR INTERMEDIATE VEGETATION COVER

When surface scattering dominates, these conditions given by van Zyl [7] are met:

$$\text{Re}(\rho) \geq \frac{\eta}{2}, \quad \frac{\eta}{2} \leq 1 \text{ and } \text{Arg}(\rho) \approx 0 \quad (14)$$

The first eigenvalue,  $\lambda_1$  corresponds then to the surface scattering term as  $k_{11}$  is positive. It was pointed out in [1] that the presence of vegetation causes the inversion to underestimate the soil moisture and overestimate the roughness. In the following paragraph, we show that applying the inversion on the cross-sections corresponding to the first eigenvalue corrects this tendency by resulting in a higher soil moisture and a lower RMS height estimate than the straightforward inversion on the cross-sections corresponding to the original covariance matrix.

From (14), we know that  $\rho$  is a positive real. We can then write (9) and (10) as:

$$\bar{k}_1 = \frac{1}{A} \begin{pmatrix} \alpha \\ 0 \\ 1 \end{pmatrix}, \quad \bar{k}_2 = \frac{1}{B} \begin{pmatrix} -\beta \\ 0 \\ 1 \end{pmatrix} \text{ and } \bar{k}_3 = \begin{pmatrix} 0 \\ 1 \\ 0 \end{pmatrix} \quad (15)$$

where

$$\alpha = \frac{2\rho}{\sqrt{\Delta} + (\zeta - 1)} \text{ and } \beta = \frac{2\rho}{\sqrt{\Delta} - (\zeta - 1)} \quad (16)$$

$A, B, \alpha$  and  $\beta$  are real and positive.

The original covariance matrix and the HH to VV ratio can be written as:

$$[T] = \begin{pmatrix} \frac{\lambda_1}{A^2}\alpha^2 + \frac{\lambda_2}{B^2}\beta^2 & 0 & \frac{\lambda_1}{A^2}\alpha + \frac{\lambda_2}{B^2}\beta \\ 0 & \lambda_3 & 0 \\ \frac{\lambda_1}{A^2}\alpha + \frac{\lambda_2}{B^2}\beta & 0 & \frac{\lambda_1}{A^2} + \frac{\lambda_2}{B^2} \end{pmatrix} \quad (17)$$

$$\frac{\sigma_{hh}^o}{\sigma_{vv}^o} = \frac{\frac{\lambda_1}{A^2}\alpha^2 + \frac{\lambda_2}{B^2}\beta^2}{\frac{\lambda_1}{A^2} + \frac{\lambda_2}{B^2}} = \alpha^2 + \frac{\frac{\lambda_2}{B^2}(\beta^2 - \alpha^2)}{\frac{\lambda_1}{A^2} + \frac{\lambda_2}{B^2}} \quad (18)$$

The covariance matrix corresponding to the first eigenvalue is:

$$[T]_1 = \begin{pmatrix} \frac{\lambda_1}{A^2}\alpha^2 & 0 & \frac{\lambda_1}{A^2}\alpha \\ 0 & 0 & 0 \\ \frac{\lambda_1}{A^2}\alpha & 0 & \frac{\lambda_1}{A^2} \end{pmatrix} \text{ and } \frac{\sigma_{hh}^o}{\sigma_{vv}^o} = \alpha^2 \quad (19)$$

As long as  $\zeta$  is greater than 1,  $\beta \geq \alpha$  and the HH to VV ratio of the full covariance matrix is larger (closer to 1) than the HH to VV ratio of surface component of the covariance matrix. It follows that the soil moisture estimated from the first component of the decomposition will be higher than the soil moisture estimated from the full covariance matrix. It is also straightforward to see that the  $\sigma_{hh}^o$  is larger for the original matrix than for the first component, resulting in a lower estimated value of the RMS height in the case of the surface component only.

## 5. CONCLUDING REMARKS

This paper describes a method to widen the domain of applicability of a soil moisture inversion algorithm previously published to include areas of intermediate vegetation cover. This method was tested on AIRSAR and SIR-C images and the results will be presented during the Workshop. In particular the following points will be clarified.

The method applies to surfaces with an azimuthal symmetry, with  $\frac{\sigma_{hh}^o}{\sigma_{vv}^o} \leq 1$  and  $\text{Arg}\langle S_{hh} S_{vv}^* \rangle \approx 0$ .

We will show that these conditions are met by most natural surfaces.

In [1], the authors introduce the HV to VV ratio as a vegetation detector. We will evaluate how this criterion can be interpreted in the light of the Cloude decomposition and analyze the value of the decomposition step by identifying those surfaces rejected under the HV to VV ratio criterion for which the decomposition method allows an estimation of the soil moisture.

## 6. ACKNOWLEDGMENT

This work was performed at the Jet Propulsion Laboratory, California Institute of Technology and at the CETP, Centre d'Etude des Environnements Terrestre et Planetaires, Velizy, France

under contract with the National Aeronautics and Space Administration.

## 7. REFERENCES

- [1] P.C. Dubois, J. van Zyl and T. Engman, "Measuring soil moisture with imaging radars, " IEEE Transactions on Geoscience and Remote Sensing, Vol. 33, No. 4, July 1995.
- [2] S.R. Cloude, "Uniqueness of target decomposition theorems in radar polarimetry," Presented at the NATO Advanced Research Workshop, Bad Windsheim, Germany, September 1988.
- [3] M.T. Hallikainen, F. T. Ulaby, M.C. Dobson, M.A. El-Rayes, and L. Wu, "Microwave dielectric behavior of wet soil- Part I: Empirical models and experimental observations," IEEE Transactions on Geoscience and Remote Sensing, Vol. 23, pp25-34, July 1985.
- [4] B. Brisco, T.J. Pultz, R.J. Brown, G.C. Topp, M.A. Hares, and W.D. Zebchuck, "Soil moisture measurements using portable dielectric probes and time-domain reflectometry," Water Resource Research, Vol. 28, pp 1339-1346, 1992.
- [5] M. Borgeaud, R.T. Shin and J.A. Kong, "Theoretical models for polarimetric radar clutter," Journal of EM Waves and Applications, Vol. 1, pp. 73-91, 1987.
- [6] J.J. van Zyl, "Application of Cloude's target decomposition to imaging radar polarimetry," Presented at the SPIE meeting in San Diego, CA, July 1992.
- [7] J.J. van Zyl, "Unsupervised classification of scattering behavior using radar polarimetric data," IEEE Transactions on Geoscience and Remote Sensing, Vol. 27, pp. 26-47, 1989.

# **Repeat Pass Aircraft Interferometry Results at Portage Lake, Maine and Innisfail, Australia**

Scott Hensley, Jeff Klein\*, Paul Rosen, Elaine Chapin, Søren Madsen and Frank Webb

Jet Propulsion Laboratory  
California Institute of Technology  
4800 Oak Grove Dr.  
Pasadena, CA 91109

\*Rockwell International

## **Abstract**

The NASA/JPL AIRSAR/TOPSAR instruments have the capability of collecting fully polarimetric radar data at three wavelengths (C, L and P-Bands) and dual antenna interferometry at C-Band, and more recently L-Band. In order to understand frequency and baseline dependent scattering effects in vegetated regions repeat pass interferometry data was collected for two vegetated regions in 1993. Portage Lake, Maine is a primarily coniferous forested region with some clear cutting from logging activities in the region. The second site at Innisfail, Australia borders a tropical rain forest and is situated adjacent to some major clear cut regions and banana plantations. Preliminary analysis of repeat pass data collected in these areas shows that the smaller the wavelength the greater the temporal decorrelation between passes, the longer the wavelength the greater the penetration depth for some types of vegetation canopy, yet for some vegetation canopy types, in particular for a banana plantation there appears to be no frequency dependent penetration into the canopy.

Key words: SAR, interferometry, repeat-pass, vegetation

## **Introduction**

Using two complex SAR images acquired from two spatially separated antennas collected simultaneously, single pass interferometry (SPI), or at different times, repeat pass interferometry (RPI), can be processed to yield elevation maps. The NASA/JPL C-band TOPSAR sensor is one example of an SPI interferometer [Zebker et al, 1992]. It is one component of the quadpolarization, three frequency airborne SAR (AIRSAR) operated by JPL. The processing of TOPSAR data into elevation maps is discussed in [Madsen et al, 1993].

It is well known that low frequency radars penetrate foliage better than radars at high frequencies, thus one might expect that interferometric measurements made at lower frequencies would yield height maps closer to the true ground surface. Until recently no multi-frequency SPI interferometric systems were available (TOPSAR has an L-Band interferometer added in 1995), hence this problem could only be addressed using RPI measurements. Moreover, to get interferometric measurements at wavelengths longer than L-band requires the use of RPI data. RPI can be used to generate height maps if 1) the passes are acquired sufficiently close in time to avoid temporal decorrelation, 2) the baseline vector, vector between the two antenna positions, is shorter than the critical baseline length, and 3) the baseline vector between the two passes is sufficiently constant.

Using repeat-pass interferometry data collected from the AIRSAR multi-frequency, multi-polarimetric radar provides a unique data set for studying frequency and polarization dependent phenomena on interferometric measurements in vegetated regions. Repeat pass data was collected near Portage Lake, Maine, a primarily coniferous forested area, and near Innisfail, Australia, a tropical forested area in Queensland. The radar operating parameters for the TOPSAR C-band mode, and the AIRSAR L and P-band polarimetric modes are given in Table I.

**Table I. AIRSAR/TOPSAR System Parameters**

Parameter	C	L	P
Wavelength (m)	.0566	.2422	.6972
Power (w)	1000	5000	1000
Bandwidth (MHz)	40	40	40
Pulse Spacing (m)	.2572	.5144	.5144
Antenna Length (m)	1.5	1.5	1.5
Baseline (m)	2.51	-	-
Altitude (m)	8100	8100	8100
Look Angle (°)	20-60	20-60	20-60
Range (km)	8.5-17	8.5-17	8.5-17
Ground Swath (km)	12	12	12

In order to process RPI data accurate platform position at each pulse event is crucial to determining the interferometric baseline as a function of time [Gray/Farris-Manning 1993]. The NASA/JPL DC-8 is equipped with a Litton INU (subsequently upgraded to a Honeywell H764-G integrated GPS/INU), a TurboRogue differential GPS receiver, and pulse time tags derived from the GOES satellite. The INU data has an update rate of 50 Hz and gives accurate relative position measurements but tends to drift with time. The differential GPS is updated at a 1 Hz rate with estimated position accuracy of 10 cm. Precise platform position information is obtained by combining the INU data with the differential GPS data. These data are linked to the pulse data using the GOES time tag.

## Experiment Description

Two sites were selected for study in 1993 using repeat-pass interferometry, one near Portage Lake in northern Maine and the other near Innisfail in Queensland, Australia. The first site has gently rolling terrain with elevations varying between 200 m and 300 m. The area is covered primarily with coniferous forest much of which is second growth due to widespread logging in the region. Vegetation heights vary from 1 m to 20 m depending on the age and type of vegetation. There are many clear cut areas in varying stages of regrowth as well as open fields used for agriculture, mostly hay as the land is not particularly well suited for commercial farming.

Considerable ground truth is available for this site since it has been used extensively by MIT Lincoln Laboratory for radar foliage penetration experiments in recent years. Measurements include tree height, canopy structure, biomass and dielectric for selected sites within a 20 km<sup>2</sup> area. In addition four 8 foot trihedral reflectors were deployed in open areas and surveyed using TurboRogue GPS receivers to be used as fiducial points in the images.

The NASA/JPL AIRSAR DC-8 flew eight passes over this site on June 24, 1993. Each pass was flown attempting to fly the same path each time in the hopes that at least one pair of passes would be suitable for RPI processing. As the onboard INU did not measure position and velocity accurately enough for RPI processing differential GPS measurements were acquired using a TurboRogue GPS receiver on the plane in conjunction with a reference receiver located near the site (and at the same location used as reference to survey the corner reflectors). Data was collected in the TOPSAR mode at C-band and in the AIRSAR 40 MHz quadpolarization mode at L and P-bands.

The second site is located in Queensland, Australia and is situated along the boundary between a tropical rain forest and a clear cut region with cultivation of some crops such as bananas. The topography varies from relatively flat in open areas to very rugged in the tropical forest. The tropical canopy reaches heights of 30 m to 40 m with occasional clearings due to logging.

Ground truth consists of 4 surveyed 8 foot trihedral reflectors deployed in open areas adjacent to the rain forest. In addition to the corner reflectors used as fiducial points, canopy measurements including tree heights and canopy structure were obtained by MIT Lincoln Laboratory.

The NASA/JPL AIRSAR DC-8 flew eight passes over this site on September 4, 1993. As described previously each pass was flown attempting to fly the same path each time in the hopes that at least one pair of passes would be suitable for RPI processing. Also as before TurboRogue differential GPS measurements were acquired using a TurboRogue GPS receiver on the plane in conjunction with a reference receiver located near the site (and at the same location used as reference to survey the corner reflectors). Data was collected in the TOPSAR mode at C-band and in the AIRSAR 40 MHz quadpolarization mode at L and P-bands.

## Data Processing

Processing of the RPI data consists of four major steps, 1) the TurboRogue differential GPS measurements are combined with the INU data to obtain accurate platform position vectors, 2) the RPI passes over a given site are analyzed to determine which ones (if any) are suitable for interferometric processing, 3) the data are converted to an appropriate coordinate system and processed into interferograms, 4) residual motion measurements are made directly from the data and the scene is processed to a height map.

TurboRogue data collected onboard the aircraft is processed at JPL using JPL derived ephemeris vectors for GPS satellites, and incorporates extensive models for ionospheric and tropospheric delays, yielding position vectors with an estimated accuracy of 10 cm [Webb et al, 1993]. These data are then combined with the INU data by high pass filtering the INU data and combining it with GPS data using a least squares approach as described in [Madsen et al, 1993].

Next pairs of repeat pass lines are examined to find suitable pairs for RPI processing. One pass is arbitrarily chosen as reference and the platform position vectors are converted into a convenient coordinate frame, the "(s,c,h)" coordinate system where s, c and h are respectively the along track, cross track, and altitude coordinates of a "best fit" spherical approximation to the ellipsoid centered at the middle of the track. The (s,c,h) coordinate frame is not a Cartesian frame, but a spherical coordinate system designed to locally approximate the WGS-84 ellipsoid. This reference sphere is chosen to



be locally tangent to the ellipsoid at a reference point called the peg point, and to have radius equal to the radius of curvature in the along track direction as shown in Figure 1.

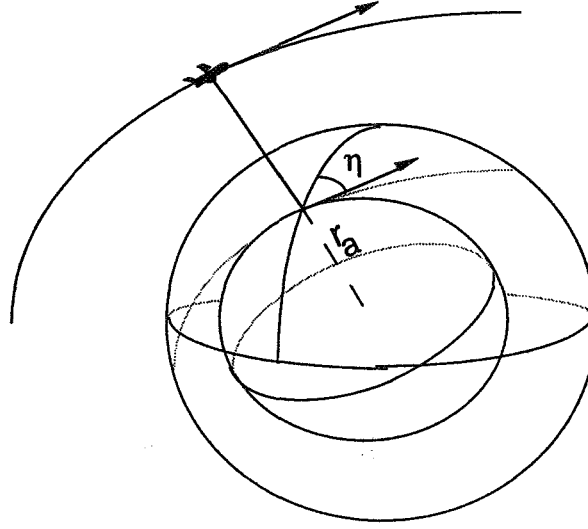


**Figure 1 .** Approximating sphere used to define the (s,c,h) coordinate system.

In the (s,c,h) system s denotes the distance along the reference curve from the peg point, which is a great circle in the approximating sphere, c is the distance along the arc perpendicular to the reference curve, and h is the height above the reference sphere.

The transformation from radar mapping coordinates, (s,c,h), to WGS-84 coordinates, (x,y,z) is described below. The radar mapping coordinates are defined relative to the sphere tangent to the ellipsoid at  $(\theta_0, \lambda_0)$ , having radius  $r_a$  which is the radius of curvature in the along track direction given by

$$r_a = \frac{r_e(\lambda_0) r_n(\lambda_0)}{r_e(\lambda_0) \cos^2(\eta) + r_n(\lambda_0) \sin^2(\eta)}$$

where  $\eta$  is the heading (actually track angle) and  $r_e$  and  $r_n$  are the radii of curvature in the east and north directions respectively given by

$$r_e(\lambda) = \frac{a}{(1 - e^2 \sin^2(\lambda))^{1/2}}, \quad r_n(\lambda) = \frac{a(1 - e^2)}{(1 - e^2 \sin^2(\lambda))^{3/2}}.$$

The point  $(\theta_0, \lambda_0)$  will be referred to as the peg point and the sphere as the approximating sphere. Take the equator of the approximating sphere to be the reference curve (i.e. reference track), assumed to be a great circle on the approximating sphere. The prime meridian to the approximating sphere is the intersection of the approximating sphere and the plane determined by the unit normal vector,  $U$ , to the ellipsoid and the cross track vector  $C = U \times T$  where  $T$  is the unit tangent vector to the reference curve. The radar mapping coordinates (s,c,h) are defined as the distance along the reference curve from the peg point, the distance from the reference curve along a meridian at a distance s from the peg point, and the height above the approximating sphere respectively. Let  $(x', y', z')$  be geocentric coordinates for the approximating sphere where the  $x'$  axis is  $U$ , the  $y'$  axis is

T and the  $z'$  axis is C. Then the transformation from mapping coordinates to  $x'y'z'$  coordinates is

$$\begin{pmatrix} x' \\ y' \\ z' \end{pmatrix} = \begin{pmatrix} (r_a + h) \cos(c_\lambda) \cos(s_\theta) \\ (r_a + h) \cos(c_\lambda) \sin(s_\theta) \\ (r_a + h) \sin(c_\lambda) \end{pmatrix}$$

where  $c_\lambda = c/r_a$  and  $s_\theta = s/r_a$ . The transformation from  $x'y'z'$  to xyz coordinates is an affine transformation of the form

$$\begin{pmatrix} x \\ y \\ z \end{pmatrix} = M_{\text{ENU}}^{\text{xyz}} M_{x'y'z'}^{\text{ENU}} \begin{pmatrix} x' \\ y' \\ z' \end{pmatrix} + O$$

where O is a translation vector,  $M_b^c$  is the transformation matrix from frame b to frame c, and the ENU frame is a basis for the tangent space at the peg point with E a unit vector in the east direction and N a unit vector in the north direction. To obtain the transformation matrix from  $x'y'z'$  to ENU observe that they are related by a rotation about the U (or  $x'$ ) axis by the track angle  $\eta$ . Thus the  $x'y'z'$  to ENU transformation matrix is

$$M_{x'y'z'}^{\text{ENU}} = \begin{bmatrix} 0 & \sin(\eta) & -\cos(\eta) \\ 0 & \cos(\eta) & \sin(\eta) \\ 1 & 0 & 0 \end{bmatrix}.$$

The transformation matrix from ENU to xyz is just the matrix formed by the column vectors of E, N, and U in xyz coordinates. The transformation matrix is

$$M_{\text{ENU}}^{\text{xyz}} = \begin{bmatrix} -\sin(\theta_0) & -\sin(\lambda_0) \cos(\theta_0) & \cos(\lambda_0) \cos(\theta_0) \\ \cos(\theta_0) & -\sin(\lambda_0) \sin(\theta_0) & \cos(\lambda_0) \sin(\theta_0) \\ 0 & \cos(\lambda_0) & \sin(\lambda_0) \end{bmatrix}.$$

The translation vector O is given by

$$O = P - r_a U$$

where  $P = (r_e(\lambda_0) \cos(\lambda_0) \cos(\theta_0), r_e(\lambda_0) \cos(\lambda_0) \sin(\theta_0), r_e(\lambda_0) (1 - e^2) \sin(\lambda_0))$  is the vector from the center of the ellipsoid to the peg point.

After conversion of the platform position vectors to (s, c, h) coordinates of the reference path, the data are aligned in time and the instantaneous baseline vector can be computed. The instantaneous baseline vector is computed as follows. For each point on the reference track the instantaneous imaging plane is computed from the yaw and pitch angles. The intersection of this plane with the second track gives one candidate baseline vector. A second candidate results from taking the imaging plane from the point and finding its intersection on the first track. Finally, the intersection of the imaging plane at this point with the second track is computed. The reference track is given by the average of these four vectors and the normal to the imaging plane determined by the average of the normals to the four imaging planes. This is illustrated in Figure 2. The instantaneous baseline is the difference between the intersections of the imaging plane containing a point on the reference track with each of the two tracks in the RPI pair. Baselines for each

pair of passes are examined for length and convergence rates. RPI pairs with baseline lengths from 15-50 meters and small convergence rates are the most desired.

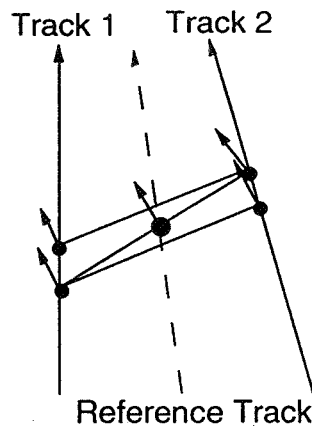


**Figure 2.** Determining the reference path and instantaneous baseline.

After selection of an appropriate RPI pair the data are motion compensated first to dual reference tracks and then to a single reference track as described in [Stevens et al, March 1995]. Using the single reference track approach the offsets between the two single look complex (SLC) images used to form the interferogram should be zero. Height reconstruction uses a modified form of the height reconstruction equations outlined in [Madsen et al, 1993].

## Results

At Portage Lake, Maine one pair of passes taken 30 minutes apart was suitable for RPI processing and the baseline as a function of along track position is shown in Figure 3. Amplitude images of all three passes are shown in Figure 4. Note that the flat open areas have progressively less backscatter as the wavelength increases whereas in the vegetated regions all three frequencies are relatively bright. Figure 5 shows C, L and P-band RPI interferograms. One cycle of color corresponds to  $2\pi$  radians of phase. The flat earth fringes are removed during the motion compensation process except for fringes due to topography and residual baseline errors. Figure 6 shows the TOPSAR generated topographic map. Note the close agreement of the P-band fringes with the TOPSAR height map. The higher azimuth fringing visible in both the C and L-band interferograms is a result of residual baseline errors. The magnitude of residual baseline can be estimated from the along track offsets between the two single look complex images used to form the interferogram. These offsets would be zero if knowledge of the baseline were perfect. A plot of the azimuth offsets as a function of along track position for five ranges is shown in Figure 7. Using a simple sinusoidal model for cross track position error as a function of along track position shows that the magnitude of the residual baseline error is approximately 6 cm. A subsequent paper will discuss estimation of these errors from the data.

A comparison of the interferometric correlation for the three frequencies is quite interesting and is shown in Figure 8. In this figure blue denotes a correlation of .25 or below and yellow a correlation 1.0. Note the almost complete decorrelation of the C-band interferogram in the vegetated areas while the clear cut areas are highly correlated. This can be compared with the TOPSAR correlation map shown in Figure 6 where the

correlation is generally above .9 in all areas. There is a dramatic increase in correlation in the vegetated regions for L and P-bands, however correlation in the flat open areas is quite poor particularly at P-band as a result of the low backscatter. We conclude that the dramatic drop in decorrelation as wavelength decreases is due to temporal decorrelation. Small motions in the leaves and branches on the order of one tenth of a wavelength cause the C-band to decorrelate faster than either L or P-bands.

Because of the relatively short baseline of 15 m, the fringe frequency is quite small and unwrapping the P-band data is not too difficult, however because the baseline is almost completely horizontal the ambiguity height (height change for one cycle of phase) varies from 60 m in the near range to 600 m in the far range. This greatly reduces the height acuity in the far range. Figure 9 shows a P-band RPI height map. The height accuracy varies from 3-30 m from near to far range making height comparisons with the TOPSAR DEM useless in the far range.

For the Innisfail, Australia data one pass was found to be suitable for RPI processing, however the baseline in this case is approximately 100 m. Figure 10 shows the TOPSAR generated DEM and L and P-band RPI interferograms. The TOPSAR DEM is shown in the upper left corner with one cycle of color equal to 150 meters, the ambiguity height at L-band. No attempt was made to remove residual baseline errors from the interferograms, hence there are slight ramps in both range and azimuth. The bright region in the upper left portion of the TOPSAR DEM is a banana plantation. Figure 11a shows a cut through the trees, from which a tree height of approximately 7-8 meters is inferred. After removing a tilt from the unwrapped P-band interferogram a cut through the banana plantation is shown in Figure 11b. Using an ambiguity height of 50 m for P-band the phase difference corresponds to roughly 8 m, in good agreement with the C-band data. Figure 10 shows the difference between the L and P band interferograms where the P-band phase has been scaled by the ratio of the wavelengths to match the L-band fringe rate. A cut through the phase difference plot is shown in Figure 11c. The phase difference corresponds to less than a meter. This indicates there is no differential penetration as a function of wavelength for the banana grove.

## Conclusions

Preliminary analysis of repeat pass data collected in these areas shows that the smaller the wavelength the greater the temporal decorrelation between passes, the longer the wavelength the greater the penetration depth for some types of vegetation canopy, yet for some vegetation canopy types, in particular for a banana plantation there appears to be no frequency dependent penetration into the canopy for the three frequencies.

## Acknowledgments

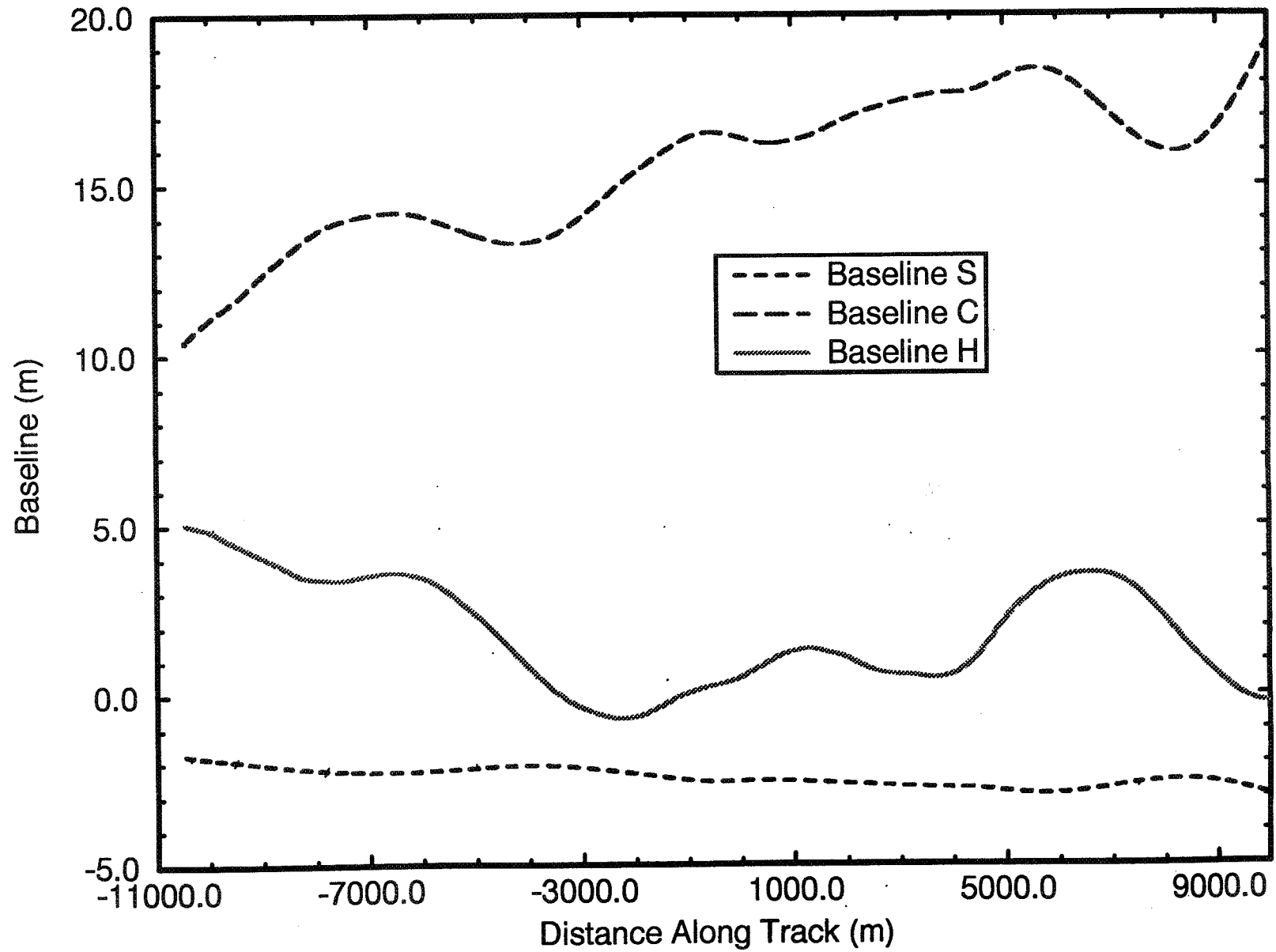
We would like to thank M. Moghaddam and D. Haub for their participation in this experiment, JPL Aircraft Radar Group for collecting this data, and MIT Lincoln Laboratory (particularly R. Downing) for valuable assistance in setting up the experiment. The research described in this paper was carried out by the Jet Propulsion Laboratory, California Institute of Technology, under contract with the National Aeronautics and Space Administration.

## References

- [1] Zebker, H.A. et al, "The Topographic Interferometric Radar Mapping Instrument", *IEEE Trans. on Geoscience and Remote Sensing*, V.30, No. 5, Sept. 1992.
- [2] Madsen, S. N., Zebker, H. A., Martin, J., "Topographic Mapping Using Radar Interferometry: Processing Techniques", *IEEE Trans. on Geoscience and Remote Sensing*, V.31, No. 1, Jan. 1993.
- [3] Gray, A.L. and Farris-Manning, P.J., "Repeat Pass Interferometry with Airborne Synthetic Aperture Radar", *IEEE Trans. on Geoscience and Remote Sensing*, V.31, No. 1, Jan. 1993.
- [4] Webb, F. H. and Zumberge, J. F., *An Introduction to GIPSY/OASIS-II*, JPL D-11088, Jet Propulsion Laboratory, Pasadena, CA, July 1995.
- [5] Stevens, D. R., Cumming, I. G., and Gray, A. L., " Options for Airborne Interferometric SAR Motion Compensation", *IEEE Trans. on Geoscience and Remote Sensing*, V.33, No. 2, Mar. 1995.

**Figure 3.**

Baseline at Portage Lake, Maine



**Page intentionally left blank**



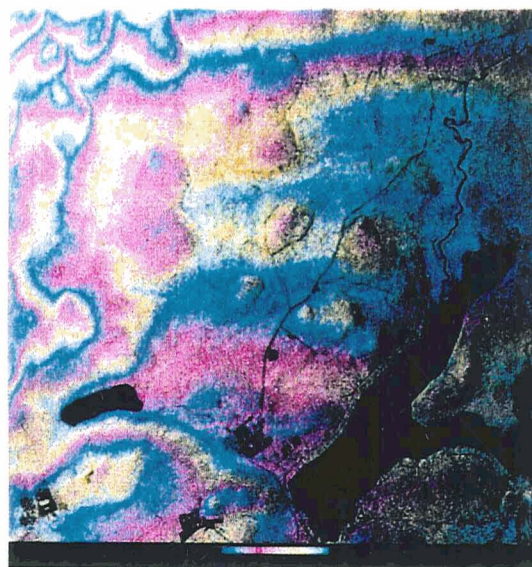
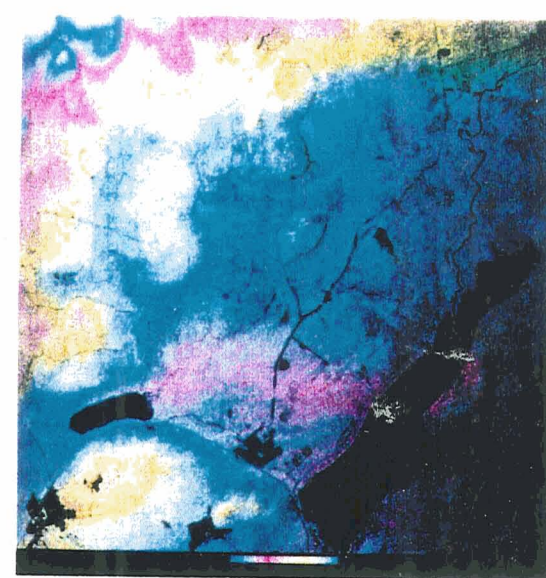
# Amplitude Imagery

**C****L****P**

Figure 4.

**Page intentionally left blank**

# Interferograms

**C-band Repeat****L-band Repeat****P-band Repeat**

**Page intentionally left blank**



# JPL C-BAND TOPSAR HEIGHT AND CORRELATION MAPS Portage Lake, Maine 1993

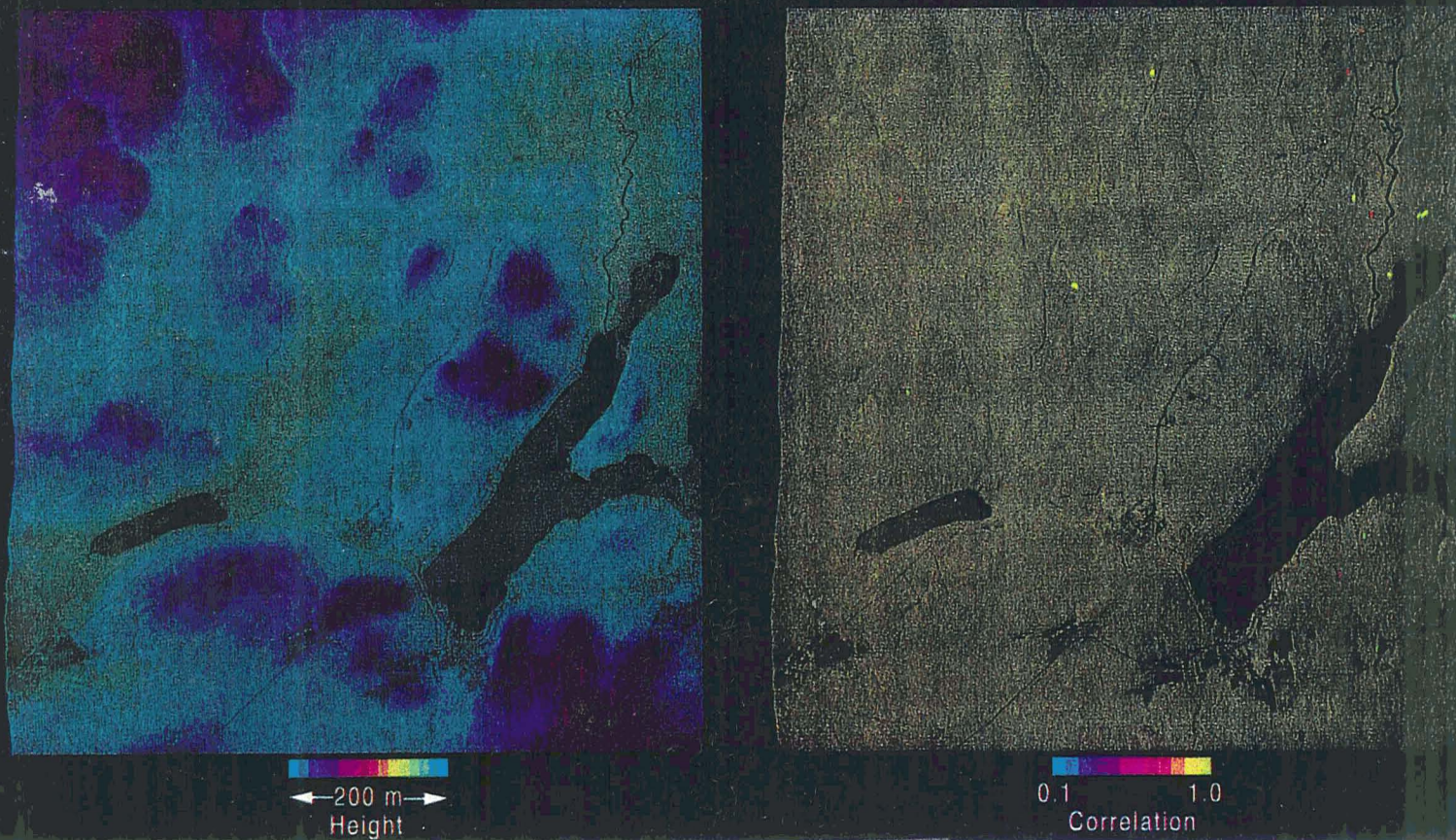
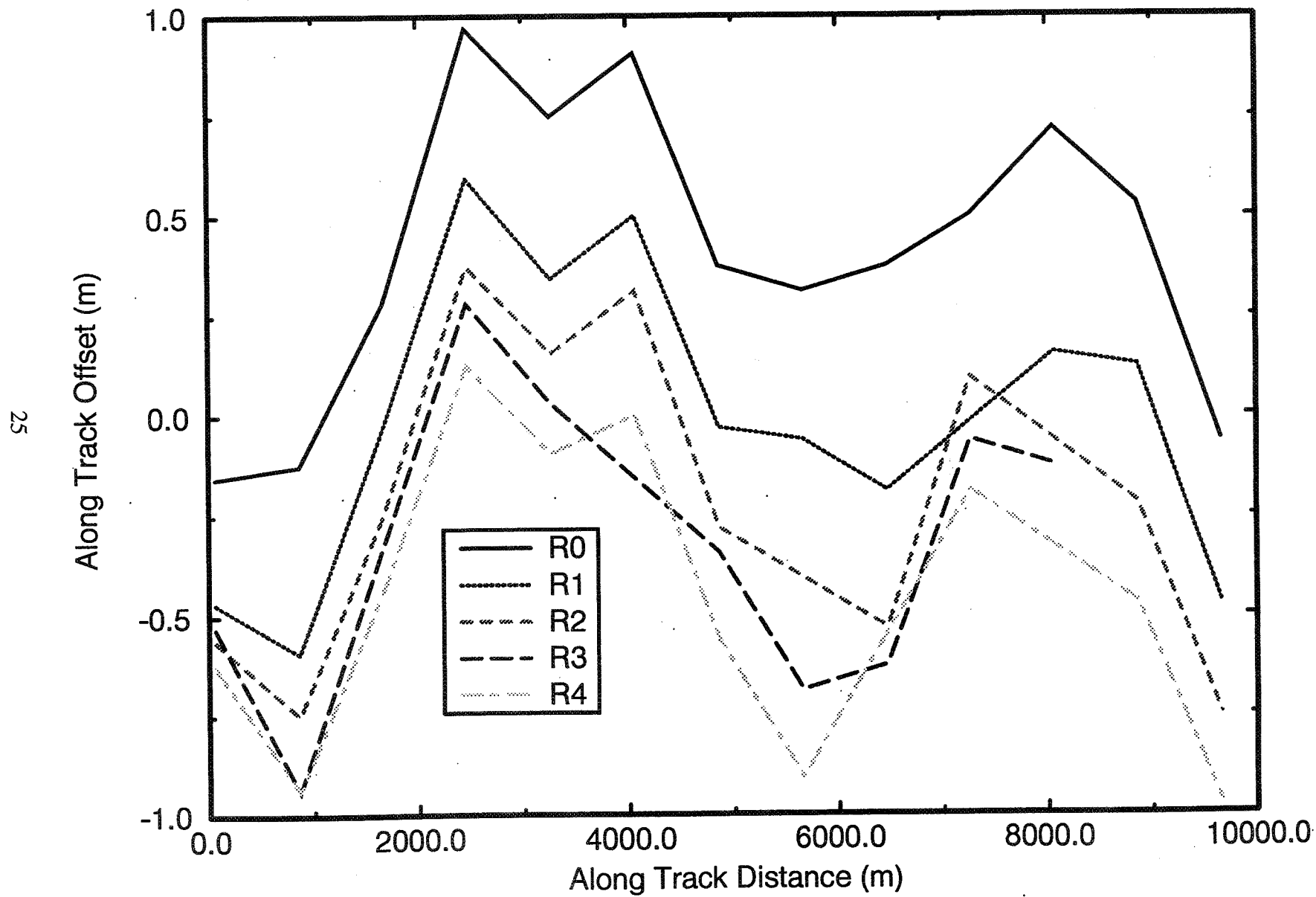


Figure 6.

**Page intentionally left blank**

**Figure 7.**

Along Track Offsets for Fixed Ranges





**Page intentionally left blank**

# **Correlation Maps**

**C-band Repeat****L-band Repeat****P-band Repeat**

**Page intentionally left blank**



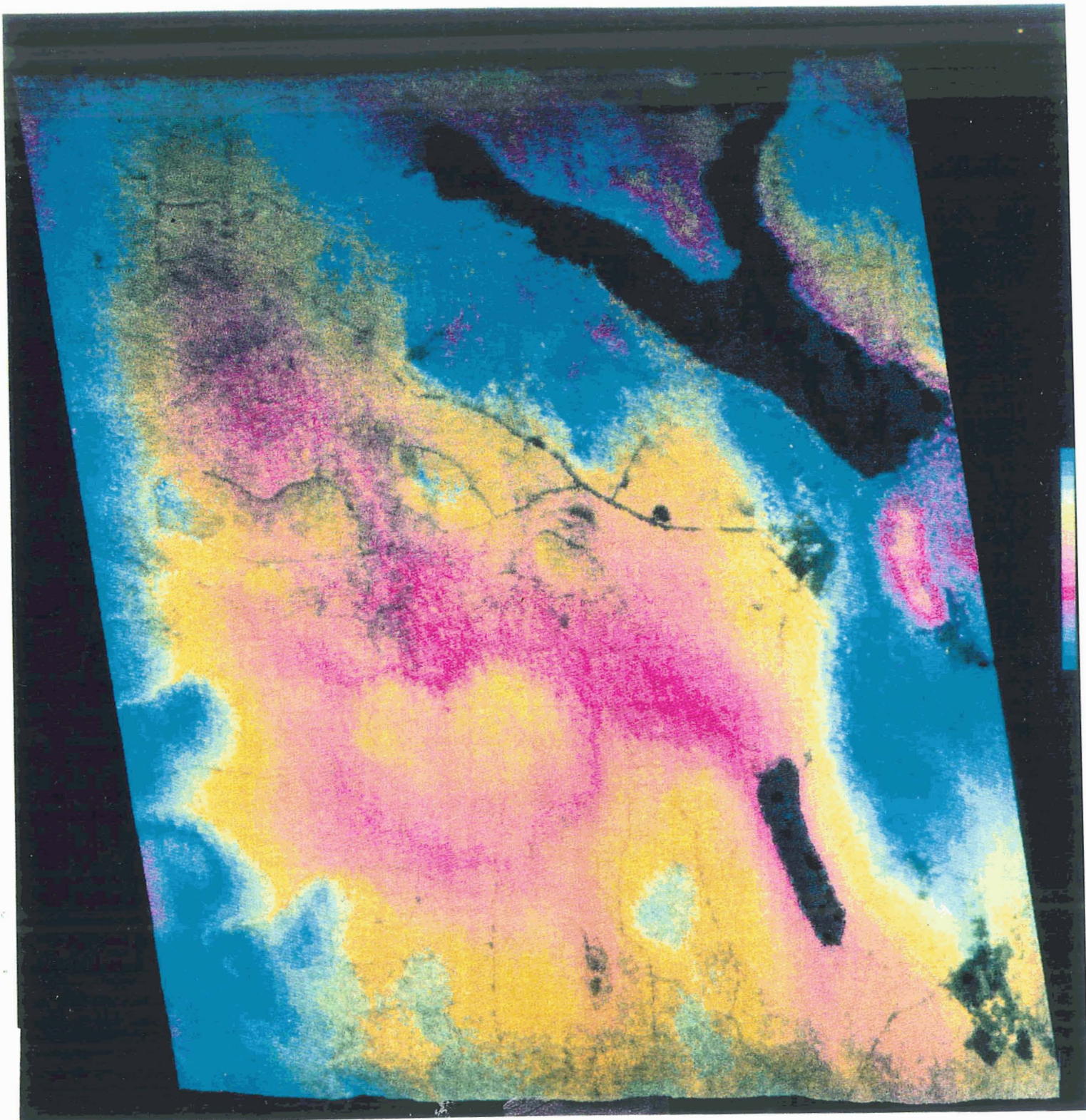


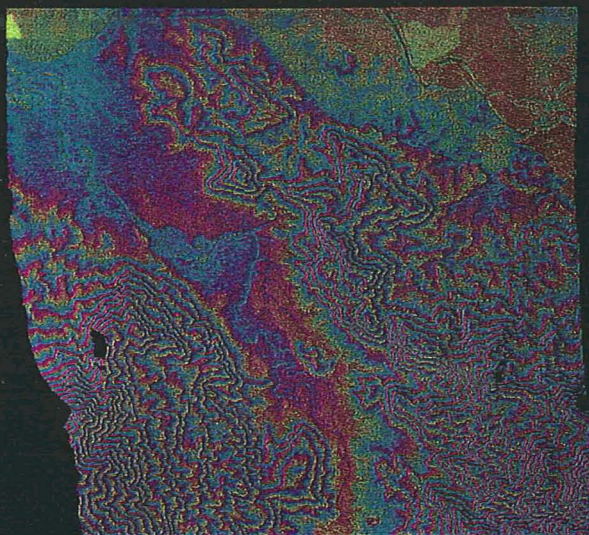
Figure 9.

**Page intentionally left blank**



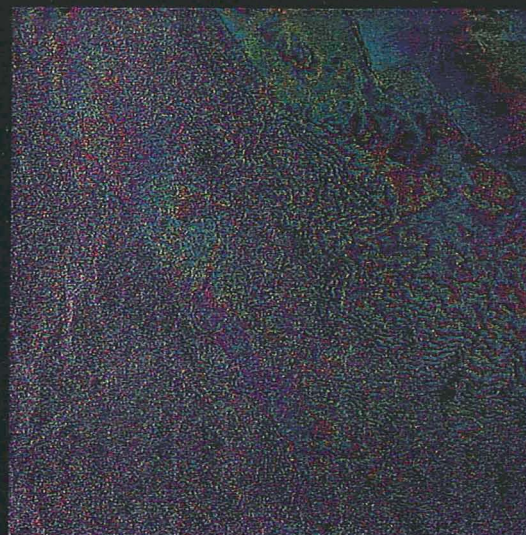
TOPSAR/AIRSAR REPEAT PASS INTERFEROMETRY  
Innisfail, Australia 1993

TOPSAR DEM (C-BAND)



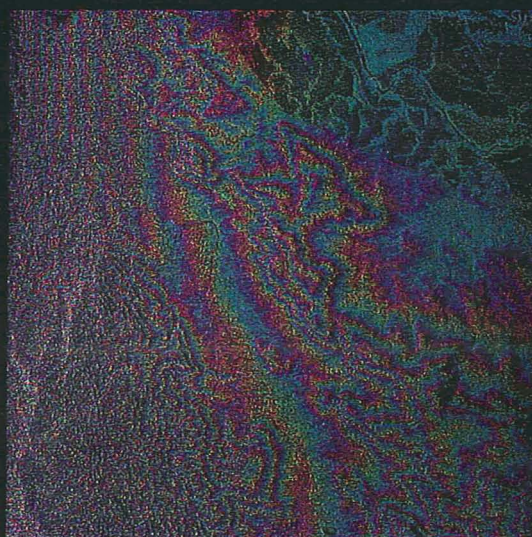
50 M  
1 Cycle / 150 M

RTI L-BAND INTERFEROGRAM



1 Cycle / 50 M

RTI P-BAND INTERFEROGRAM



$L - (\lambda_P / \lambda_L) P$  INTERFEROGRAM

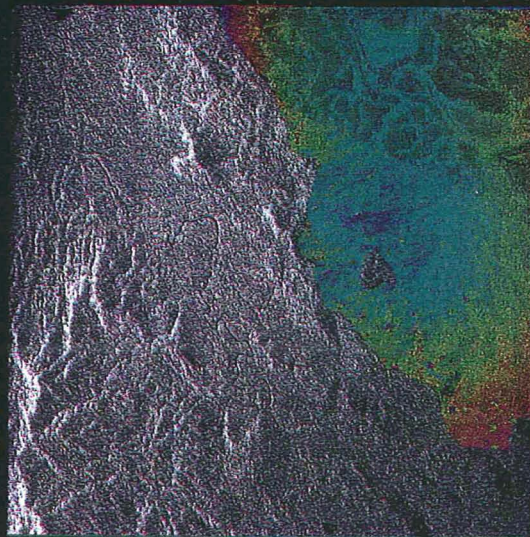


Figure 10.

**Page intentionally left blank**

Figure 11 a.

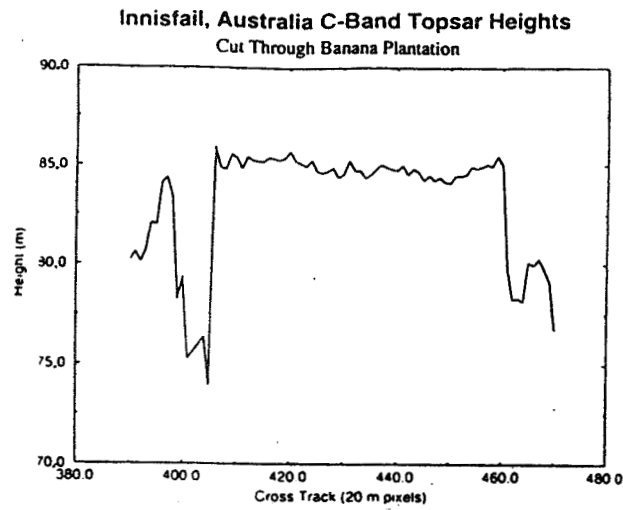


Figure 11 b.

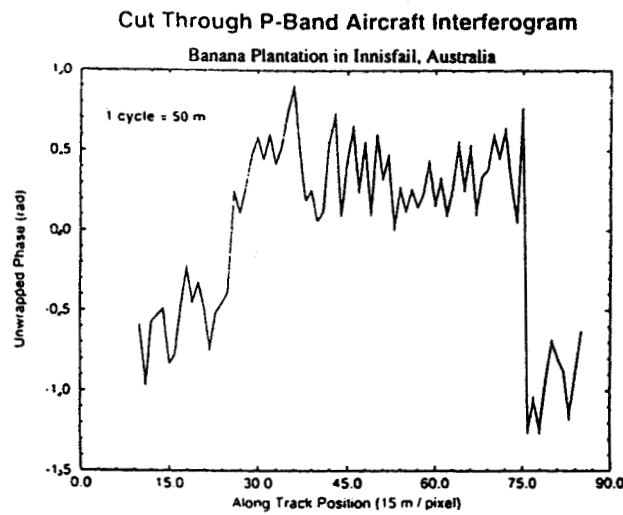
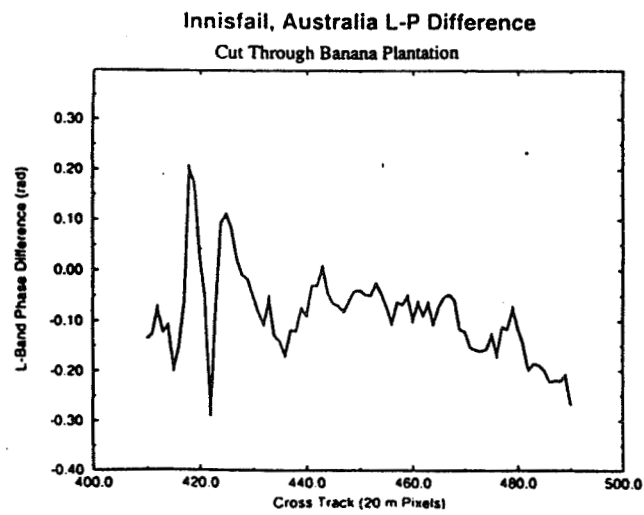


Figure 11 c.





**Page intentionally left blank**

## GEOCODING OF AIRSAR/TOPSAR SAR DATA

Francesco Holecz \*, Yunling Lou, and Jakob van Zyl

Jet Propulsion Laboratory  
California Institute of Technology  
4800 Oak Grove Drive, M/S 300-243  
Pasadena, CA 91109  
E-mail: franci@blacks.jpl.nasa.gov  
FAX: +1 818 354 0495

\* on leave from Remote Sensing Laboratories, University of Zürich, Switzerland

### 1. INTRODUCTION

It has been demonstrated and recognized that radar interferometry is a promising method for the determination of digital elevation information (Zebker et al., 1994; Madsen et al., 1995) and terrain slope (Wegmüller et al., 1993) from Synthetic Aperture Radar (SAR) data. An important application of Interferometric SAR (InSAR) data in areas with topographic variations is that the derived elevation and slope can be directly used for the absolute radiometric calibration of the amplitude SAR data (van Zyl et al., 1993; Holecz et al., 1994), as well as for scattering mechanisms analysis (van Zyl, 1993; Holecz et al., 1995). On the other hand polarimetric SAR data has long been recognized as permitting a more complete inference of natural surfaces than a single channel radar system. In fact, imaging polarimetry provides the measurement of the amplitude and relative phase of all transmit and receive polarizations.

On board the NASA DC-8 aircraft, NASA/JPL operates the multifrequency (P, L and C bands) multipolarimetric radar AIRSAR (van Zyl et al., 1992). The TOPSAR, a special mode of the AIRSAR system, is able to collect single-pass interferometric C- and/or L-band VV polarized data (van Zyl et al., 1995). A possible configuration of the AIRSAR/TOPSAR system is to acquire single-pass interferometric data at C-band VV polarization and polarimetric radar data at the two other lower frequencies. The advantage of this system configuration is to get digital topography information at the same time the radar data is collected. The digital elevation information can therefore be used to correctly calibrate the SAR data. This step is directly included in the new AIRSAR Integrated Processor. This processor uses a modification of the full motion compensation algorithm described by Madsen et al. (1993). However, the Digital Elevation Model (DEM) with the additional products such as local incidence angle map, and the SAR data are in a geometry which is not convenient, since especially DEMs must be referred to a specific cartographic reference system. Furthermore, geocoding of SAR data is important for multisensor and/or multitemporal purposes. In this paper, a procedure to geocode the new AIRSAR/TOPSAR data is presented. As an example an AIRSAR/TOPSAR image acquired in 1994 is geocoded and evaluated in terms of geometric accuracy.

## 2. THE AIRSAR INTEGRATED PROCESSOR

A complete description of the AIRSAR/TOPSAR products is given in van Zyl (1995). Here we briefly present the different output data types. The Integrated AIRSAR Processor produces two data products: the standard AIRSAR products in frame and synoptic format, and the integrated TOPSAR product. The last one consists of a number of different data types, namely:

- **Digital Elevation Model**, which represents the elevation of the terrain above a spherical approximation to the World Geodetic System 84 (WGS84). The data are stored as two bytes.
- **C-band VV polarized** calibrated amplitude data as acquired with the top antenna in the TOPSAR mode. The radiometric corrections are performed taking into account the topography when removing the antenna patterns and the scattering areas. The data are stored as two bytes.
- **Local incidence angle map** derived using the digital elevation model information. The data are stored as one byte.
- **Correlation map** contains the normalized correlation coefficient between the two C-band interferometric channels. The data are stored as one byte.
- **L-band polarimetry data** contain the calibrated AIRSAR compressed Stokes matrix data at L-band. Each pixel is represented by ten bytes.
- **P-band polarimetry data** contain the calibrated AIRSAR compressed Stokes matrix data at P-band. Each pixel is represented by ten bytes.

The selected radar mapping coordinate system  $(s, c, h_r)$  is defined relative to the sphere tangent to the WGS84 ellipsoid at longitude  $\lambda_p$  and latitude  $\varphi_p$  - referred to as the peg point and approximately corresponding to the center of the image - having a radius  $r_a$ , which is the radius of curvature in the along track direction (Hensley, 1993). In this system,  $s$  and  $c$  are distances in along and across direction, while  $h_r$  is the height above the approximating sphere.

## 3. FROM THE RADAR MAPPING TO MAP COORDINATE SYSTEM

This section describes the transformation from the radar mapping coordinates  $(s, c, h_r)$  into the map coordinates  $(x, y, h_o)$ . An accurate transformation of the derived DEM data into map coordinates is only possible by using a forward transform. In fact, by applying a backward transform, which has the advantage of fewer number of calculations, the pixel location in the map coordinate system can be inaccurate, because the pixel altitude  $h_o$  is usually unknown. Thus, the following geodetic and cartographic transformation steps must be carried out:

1. From radar mapping  $(s, c, h_r)$  into global Cartesian coordinates  $(X, Y, Z)$
2. From global Cartesian into local Cartesian coordinates  $(X', Y', Z')$
3. From local Cartesian into geographic coordinates  $(\lambda, \varphi, h_e)$
4. From geographic into map coordinates  $(x, y, h_o)$

A forward transform implies that the output product can contain holes, if inappropriately implemented. To avoid gaps in the output data, four map coordinates, corresponding to four DEM corners in the radar mapping coordinates, define the orientation and the surface of the pixel. The area is then filled using a polygon fill algorithm. This procedure is subsequently applied to each pixel of the input data. In order to be computationally efficient, the transformation of radar coordinate positions for each pixel to the map coordinate system is stored in a two dimensional look-up table. Thus, all additional input products, such as local incidence angle map, correlation map, and SAR data can be very easily and efficiently geocoded using the same look-up table.

The first step is to transform the DEM data from the radar coordinates into the global Cartesian coordinates (in this case the WGS84 system), namely:

$$\begin{pmatrix} X \\ Y \\ Z \end{pmatrix} = \mathbf{M}_1 \mathbf{M}_2 \begin{pmatrix} (r_a + h_r) \cos c_\varphi \cos s_\lambda \\ (r_a + h_r) \cos c_\varphi \sin s_\lambda \\ (r_a + h_r) \sin c_\varphi \end{pmatrix} + \mathbf{O}$$

where

$$\mathbf{M}_1 = \begin{pmatrix} -\sin \lambda_p & -\sin \varphi_p \cos \lambda_p & \cos \varphi_p \cos \lambda_p \\ \cos \lambda_p & -\sin \varphi_p \sin \lambda_p & \cos \varphi_p \sin \lambda_p \\ 0 & \cos \varphi_p & \sin \varphi_p \end{pmatrix}$$

$$\mathbf{M}_2 = \begin{pmatrix} 0 & \sin \eta & -\cos \eta \\ 0 & \cos \eta & \sin \eta \\ 1 & 0 & 0 \end{pmatrix}$$

$$\mathbf{O} = \begin{pmatrix} r_e(\varphi_p) \cos \varphi_p \cos \lambda_p \\ r_e(\varphi_p) \cos \varphi_p \sin \lambda_p \\ r_e(\varphi_p)(1 - e^2) \sin \varphi_p \end{pmatrix} - \begin{pmatrix} r_a \cos \varphi_p \cos \lambda_p \\ r_a \cos \varphi_p \sin \lambda_p \\ r_a \sin \varphi_p \end{pmatrix}$$

$$r_a = \frac{r_e(\varphi_p) r_n(\varphi_p)}{r_e(\varphi_p) \cos^2 \eta + r_n(\varphi_p) \sin^2 \eta}$$

$$r_e(\varphi_p) = \frac{a}{(1 - e^2 \sin^2 \varphi_p)^{\frac{1}{2}}}$$

$$r_n(\varphi_p) = \frac{a(1 - e^2)}{(1 - e^2 \sin^2 \varphi_p)^{\frac{3}{2}}}$$

$r_e$  and  $r_n$  are the East and North radius of curvature at the peg point,  $\eta$  is the heading (or track angle),  $c_\varphi = c/r_a$ ,  $s_\lambda = s/r_a$ ,  $\mathbf{O}$  is a translation vector,  $\mathbf{M}_1$  and  $\mathbf{M}_2$  are transformation matrices,  $a$  and  $e^2$  are the semi-major axis and the ellipticity of the WGS84 ellipsoid ( $a = 6378137$  m,  $e^2 = 0.00669437999015$ ). Basically, to specify the transformation from the radar mapping coordinates to the Earth centered Cartesian coordinate system, only three parameters are required, namely the latitude and longitude of the peg point, and the heading of the reference curve at the peg point.

Since the ellipsoid origin of a given cartographic reference system is not necessarily coincident with the Earth center and their shape and size may vary considerably, geodetic datums must be considered. The datum transformation is described by the three dimensional Helmert transformation (Frei et al., 1993), namely:

$$\begin{pmatrix} X \\ Y \\ Z \end{pmatrix} = \begin{pmatrix} \Delta x \\ \Delta y \\ \Delta z \end{pmatrix} + (1 + m)\mathbf{D} \begin{pmatrix} X' \\ Y' \\ Z' \end{pmatrix}$$

where

$$\mathbf{D} = \begin{pmatrix} \cos \beta \cos \gamma & \cos \alpha \sin \gamma + \sin \alpha \sin \beta \sin \gamma & \sin \alpha \sin \gamma - \cos \alpha \sin \beta \cos \gamma \\ -\cos \beta \sin \gamma & \cos \alpha \cos \gamma - \sin \alpha \sin \beta \sin \gamma & \sin \alpha \cos \gamma + \cos \alpha \sin \beta \sin \gamma \\ \sin \beta & -\sin \alpha \cos \beta & \cos \alpha \cos \beta \end{pmatrix}$$

and  $(\Delta x, \Delta y, \Delta z)$  are translation parameters,  $m$  a scaling parameter, and  $(\alpha, \beta, \gamma)$  three rotation parameters.

Now, the transformation from the local Cartesian coordinates into the geographic coordinates can be carried out, namely:

$$\varphi = \arctan \frac{Z' + (e')^2 b \sin^3 \theta}{d - e^2 a \cos^3 \theta}$$

$$\lambda = \frac{Y'}{X'}$$

$$h_e = \frac{d}{\cos \varphi} - \nu$$

where

$$e^2 = \frac{a^2 - b^2}{a^2}$$

$$(e')^2 = \frac{a^2 - b^2}{b^2}$$

$$\nu = \frac{a}{(1 - e^2 \sin^2 \varphi)^{\frac{1}{2}}}$$

$$d = [(X')^2 + (Y')^2]^{\frac{1}{2}}$$

$$\theta = \arctan \frac{Z' a}{d b}$$

Note that  $a$  and  $b$  are the semi-major and semi-minor axes of the ellipsoid used in a given country. Furthermore, not all countries provide the solution of the 7 parameters (i.e.  $\Delta x, \Delta y, \Delta z, m, \alpha, \beta, \gamma$ ). In those cases, usually, only the three translation parameters must be known.

The last step is to transform the geographic coordinates into a desired map coordinate system. The much used projections are the Universal Transfer Mercator, the Oblique Mercator, the Lambert Conformal Conic Projection, and the Stereographic Projection. A detailed description is given in Snyder (1987). As an example, we consider here the UTM system:

$$x = x_o + k_1\Delta\lambda + k_3\Delta\lambda^3 + k_5\Delta\lambda^5$$

$$y = y_o + k_0 + k_2\Delta\lambda^2 + k_4\Delta\lambda^4 + k_6\Delta\lambda^6$$

where  $x_o$  and  $y_o$  are the false origin coordinates,  $\Delta\lambda = (\lambda - \lambda_o)$  with  $\lambda_o$  the geographic longitude of the central meridian, and  $k_0...k_6$  are coefficients (see Snyder, 1987). Note,  $x$  refers to the Easting coordinates, while  $y$  to the Northing coordinates. It should be noted that to obtain orthometric heights  $h_o$ , ellipsoidal heights  $h_e$  need to be corrected for the geoidal heights  $h_g$  according to  $h_o \cong h_e - h_g$ .

#### 4. RESULTS

The SAR data used in this study were collected by the NASA/JPL AIRSAR/TOPSAR system in 40 MHz mode on April 12, 1994 over the area of Atlanta airport (33.76°N, 83.59°W), Georgia. The data have a postprocessing pixel spacing of 10 meters and cover an area of around 100 km<sup>2</sup>. The DEM was geocoded to the UTM coordinate system zone 16 (central meridian 87°) taking into account the North American Datum 1927 (Clarke ellipsoid 1866,  $\Delta x = -9$  m with  $\sigma_{\Delta x} = 5$  m,  $\Delta y = 161$  m with  $\sigma_{\Delta y} = 5$  m,  $\Delta z = 179$  m with  $\sigma_{\Delta z} = 8$  m).

Figure 1 represents the location accuracy for 8 selected ground control points without using (left) and by using some independent ground control points (right). Figure 2 shows the geocoded DEM (a) with the corresponding correlation map (b), the derived local incidence angle map (c), the C-band VV-polarized amplitude data (d), the L-band HH-polarized amplitude data (e), and the L-band HV-polarized amplitude data (f).

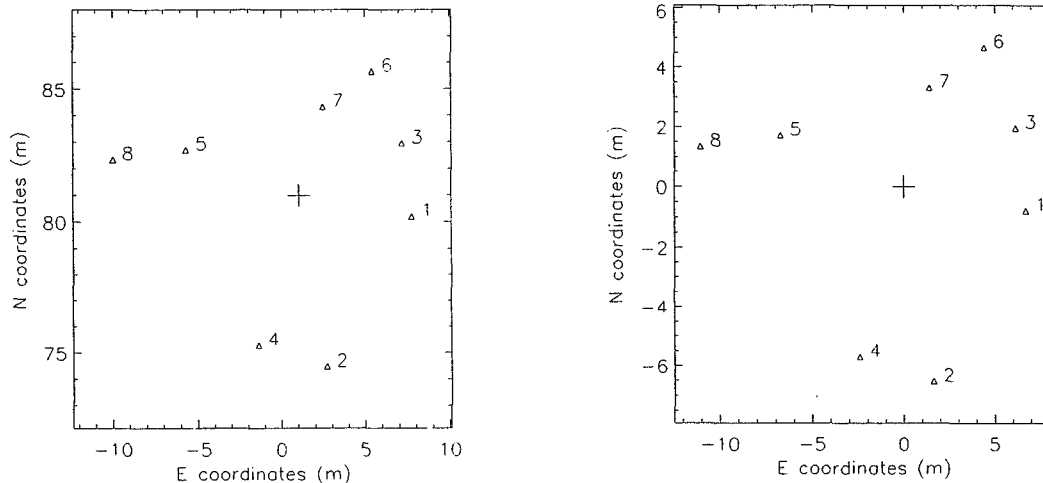
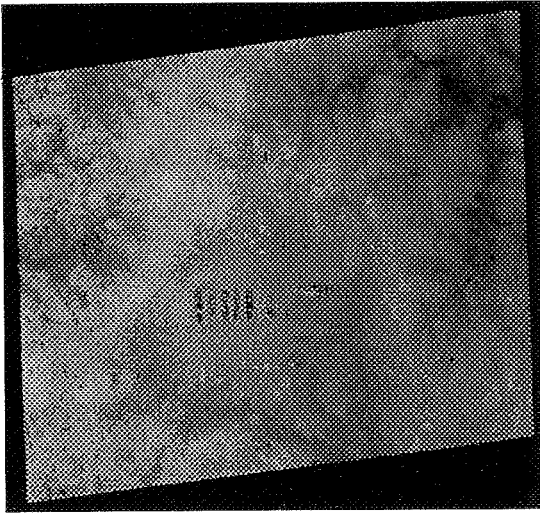
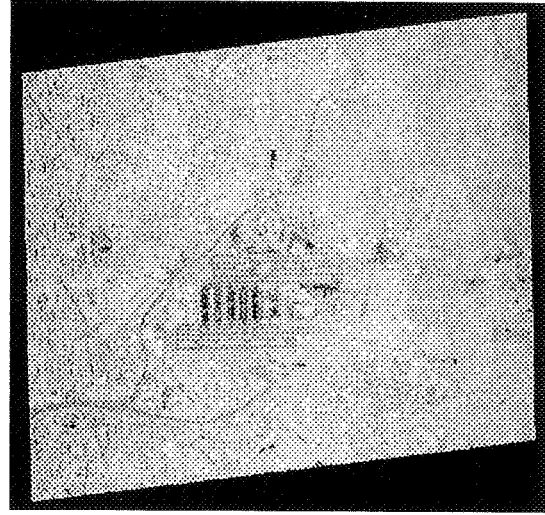


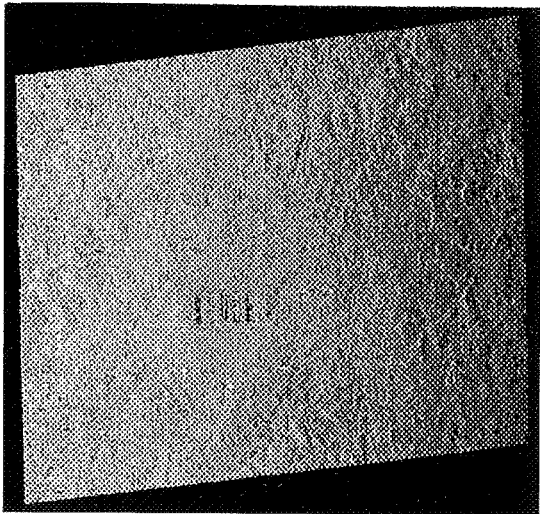
Figure 1: Positioning accuracy without (left) and with ground control points (right).



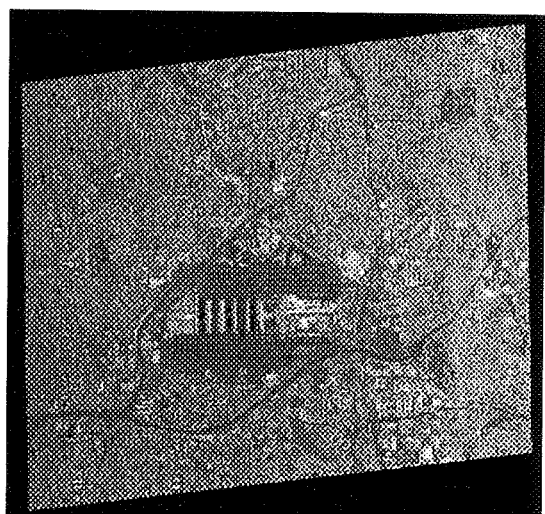
a)



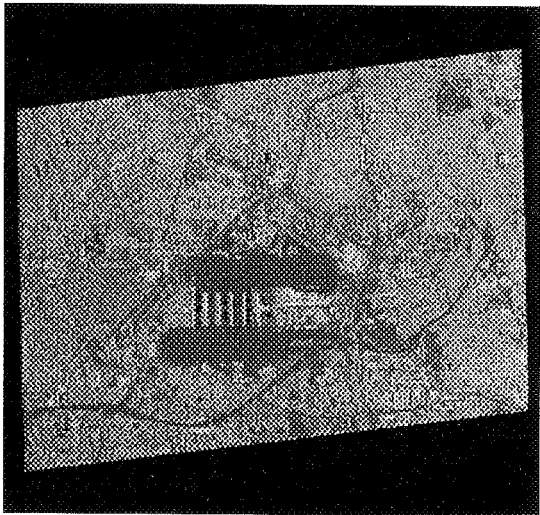
b)



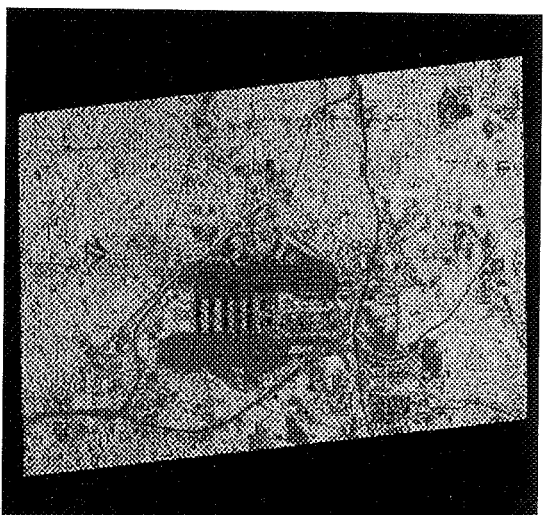
c)



d)



e)



f)

Figure 2: Geocoded AIRSAR/TOPSAR products in UTM zone 16 a) DEM, b) Correlation map, c) Local incidence angle map, d) C-VV data, e) L-HH data, f) L-HV data.

An important prerequisite for accurate geocoding is precise flight path data. Currently, the NASA DC-8 aircraft is equipped with the Honeywell H-764G Inertial Navigation System (INS) with an embedded Global Positioning System (GPS) receiver. This system, which has an acquisition rate of 50 Hz, meets a position accuracy of  $\leq 16$  meters, a pitch and roll accuracy of  $\leq 0.01$  degrees, and a heading accuracy of  $\leq 0.02$  degrees (Honeywell, 1993). Note that this GPS performance is obtained during a period of normal GPS coverage with a Position Dilution of Precision of 3.2 or less, and P(Y)-Code receiver mode. In other words, using this flight path data accuracy, and also considering the uncertainties of the datums' shift parameters, a geocoding precision of  $\pm 1$  pixel is expected, assuming a postprocessing pixel spacing of 10 meters.

Figure 1 (left) clearly shows in the  $y$ -direction, i.e. N-S direction, an average location error of around 80 meters (corresponding to 8 pixels in the DEM data), while in the  $x$ -direction it is about 1 pixel. However, by using 1 ground control point, these inaccuracies are reduced, resulting in a final positioning precision on the order of  $\pm 1$  pixel (Figure 1 right). A possible explanation of the observed error in  $y$ -direction could be figured in a time synchronization problem between the GPS measurements and the SAR data. In fact, the flight track angle  $\eta$  in this case was of  $0^\circ$ , i.e. S-N direction, and therefore positioning inaccuracies in the  $y$ -direction were mainly affected. It should be noted that the position of the 8 ground control points was determined by using a 1:24,000 scale map of the U.S. Geological Survey. Therefore, some minor inaccuracies due to the map scale must also be considered.

## 5. CONCLUSIONS

In this paper we presented a procedure to geocode the new AIRSAR/TOPSAR data. Furthermore, it was shown that geocoding of these data is well defined, without using, as is often done, transformations based on polynomials, which can strongly affect the geometric accuracy. Using geodetic and cartographic transforms, the geocoding can basically be carried out without the need of ground control points, which sometimes can be difficult, especially for those areas where the availability of topographic maps is almost impossible. At this time, we are testing this procedure for data sets acquired during the 1994 and 1995 campaigns in order to figure out the above mentioned error. In addition, we are planning to optimize the geocoding procedure without using the intermediary  $(s, c, h_r)$  radar mapping system. This will allow a straight geocoding from slant range to a given reference map coordinate system, in order to deliver to the users geocoded AIRSAR/TOPSAR data.

## ACKNOWLEDGMENTS

This study was supported by the Swiss Academy of Science and the Holderbank Foundation. A portion of the research described in this paper was performed by the Jet Propulsion Laboratory, California Institute of Technology, under a contract with the National Aeronautics and Space Administration.



## REFERENCES

- Frei U., C. Graf, and E. Meier, 'Cartographic reference systems', Chapter 10 in SAR-Geocoding - Data and Systems, Wichmann-Verlag, Karlsruhe, Germany, edited by G. Schreier, 1993.
- Hensley S., 'Interoffice Memorandum 3346-93-163' (internal document), Jet Propulsion Laboratory, Pasadena, Calif., 1993.
- Holecz F., E. Meier, J. Piesbergen, D. Nüesch, and J. Moreira, 'Rigorous derivation of the backscattering coefficient', IEEE Geoscience and Remote Sensing Newsletter, No. 92, September, 1994.
- Holecz F., U. Wegmüller, E. Rignot, and Y. Wang, 'Observed radar backscatter from forested areas with terrain variations', Proceedings IGARSS'95, Firenze, 1995.
- Honeywell, 'Detailed specification for the H-764G Inertial Navigation System (INS) with an embedded Global Positioning System (GPS) receiver', Avionics Division, St. Petersburg, Florida, 1993.
- Madsen S., H. Zebker, and J. Martin, 'Topographic mapping using radar interferometry: Processing techniques', IEEE Transactions on Geoscience and Remote Sensing, Vol. 31, No. 1, 1993.
- Madsen S., J. Martin, and H. Zebker, 'Analysis and evaluation of the NASA/JPL TOPSAR across-track interferometric SAR system', IEEE Transactions on Geoscience and Remote Sensing, Vol. 33, No. 2, 1995.
- Snyder J., 'Map projections used by the U.S. Geological Survey', Geological Survey Bulletin 1532, United States Government Printing Office, Washington DC, 1987.
- van Zyl J., R. Carande, Y. Lou, T. Miller, and K. Wheeler, 'The NASA/JPL three frequency polarimetric AIRSAR System', Proceedings IGARSS'92, Houston, 1992.
- van Zyl J., 'The effect of topography on radar scattering from vegetated areas', IEEE Transactions on Geoscience and Remote Sensing, Vol. 31, No. 1, 1993.
- van Zyl J., B. Chapman, P. Dubois, and J. Shi, 'The effect of topography on SAR calibration', IEEE Transactions on Geoscience and Remote Sensing, Vol. 31, No. 5, 1993.
- van Zyl J., 'AIRSAR Integrated Processor Documentation' Version 0.01 (internal document), Jet Propulsion Laboratory, Pasadena, Calif., 1995.
- van Zyl J., H. Zebker, S. Hensley, D. Haub, and W. Wiesbeck, 'The new dual frequency (C- and L-band) TOPSAR airborne interferometric SAR', Proceedings IGARSS'95, Firenze, 1995.
- Wegmüller U., C. Werner, and P. Rosen, 'Derivation of terrain slope from SAR interferometric phase gradient', Second ERS-1 User Symposium, Hamburg, 1993.
- Zebker H., C. Werner, P. Rosen, and S. Hensley, 'Accuracy of topographic maps derived from ERS-1 interferometric radar', IEEE Transactions on Geoscience and Remote Sensing, Vol. 32, No. 4, 1994.

# MEASUREMENT OF OCEAN SURFACE SLOPE BY AIRSAR

J.S. Lee and D. L. Schuler  
Remote Sensing Division, Code 7263  
Naval Research Laboratory  
Washington DC 20375-5351, USA  
Tel: 202 767-2004, Fax: 202 767-5599  
E-mail:lee@imsy1.nrl.navy.mil

## 1. INTRODUCTION

A new technique has been developed to measure ocean surface slopes by polarimetric SAR. This technique has the potential of estimating surface slope in the along-track direction at an accuracy of a fraction of a degree. Experimental results using NASA/JPL AIRSAR P-, L-, C-band data from the Gulf Stream'90 Experiment showed a sudden slope change at a converging current front.

The capability of SAR for the imaging of ocean waves, currents, surfactants, slicks, etc. has been studied in great detail (*Hasselman et al*, 1985, *Alpers et al*, 1981). However, few studies have been devoted to the understanding of the polarimetric aspect of the SAR response to waves, currents and other ocean surface features. The polarimetric SAR simultaneously collects the backscattered responses from HH, HV, VH and VV polarizations, from which a Mueller matrix can be formed. From the Mueller matrix, the inherent scattering mechanism can be revealed by the polarization signature (*van Zyl*, 1987). *Schuler et al* (1993) have shown that, based on the stochastic surface tilts suggested by *Cox and Munk* (1954), the polarimetric SAR response of an ambient ocean surface agrees with the tilted Bragg model (*Valenzuela*, 1968). They also showed that the co-polarization signature of a current front displayed a higher degree of depolarization induced by the composite nature of scattering mechanisms, such as tilted-Bragg and specular, and the scatter caused by breaking waves.

For idealized Bragg scattering, the peak value of the co-polarization signature plot occurs at a polarization orientation angle of  $90^\circ$ , and an ellipticity angle of  $0^\circ$  (i.e., at VV polarization). However, a tilted surface in the azimuth direction introduces the HV and VH components, and causes the shift of the location of the maximum response away from the orientation angle of  $90^\circ$ . The amount of shift correlates with the slope of the tilted surface. This phenomenon has been utilized to develop slope measurements of mountainous desert terrain and forested areas (*Schuler, Lee and De Grandi*, 1995). For topographic measurements, the inhomogeneities of forest and deserted areas often introduce various dominant scattering mechanisms. Algorithms for the slope measurement have to be carefully devised to account for this variation. For ocean surfaces, however, the dominant scattering mechanism for incident angles between  $25^\circ$  to  $65^\circ$  has been adequately represented by composite surface, or tilted-Bragg models for the backscatterer (*Valenzuela*, 1968). Consequently, the estimation of ocean surface slope is expected to produce more consistent results.

This new slope measurement technique is applied to the P-, L-, C-band polarimetric SAR images of a current front with converging flows. The orientation angle displacement in the co-polarization signature is computed for each pixel. The results show a sudden  $1.3^\circ$  slope change at the front. All three bands show a similar trend. The effect of velocity bunching on this measurement technique will be investigated. The measurement error and the limitations of this technique will also be discussed.

## 2. IN-SITU MEASUREMENTS

During the 1990 Gulf Stream Experiment, the AIRSAR imaged the north edge of the Gulf stream supersite near the coast of Virginia (36.5°N, 72.0°W) (Valenzuela, 1991). Simultaneous shipboard measurements of currents, temperature, salinity, etc. were also made. Two relatively bright lines in the SAR imagery delineated a filament of cool, fresh water that was entrained by the Gulf Stream as it passed near the continental shelf. In-situ measurements made from the R/V Cape Henlopen are summarized in Fig.1. A southerly bright line corresponds to a surface front having relatively weak current shear, but a convergence velocity (measured at 7-m depth) of about 20 cm/s. Nearly coincident interferometric SAR measurements confirm the weak shear and show a surface convergence of 20-25 cm/s. Surface convergence was also suggested by the narrow width of the frontal temperature change, surface accumulation of *Sargassum*, and an adjacent band of breaking waves. A more northerly bright line, which was not well-sampled, appeared to coincide with a zone of stronger current shear between the filament and the slope water to the north. Some convergence may have existed at this shear front as well. A second filament lying farther inside the Gulf Stream also showed a strong linear feature and also had strong surface convergence. Ocean waves were driven by southwesterly 8 m/s winds. Wave-current interactions at these fronts produced narrow bands of steep and breaking waves manifesting higher radar returns in polarimetric SAR images. Detailed discussion of the environmental setting and in-situ measurements is given by Marmorino *et al* (1994).

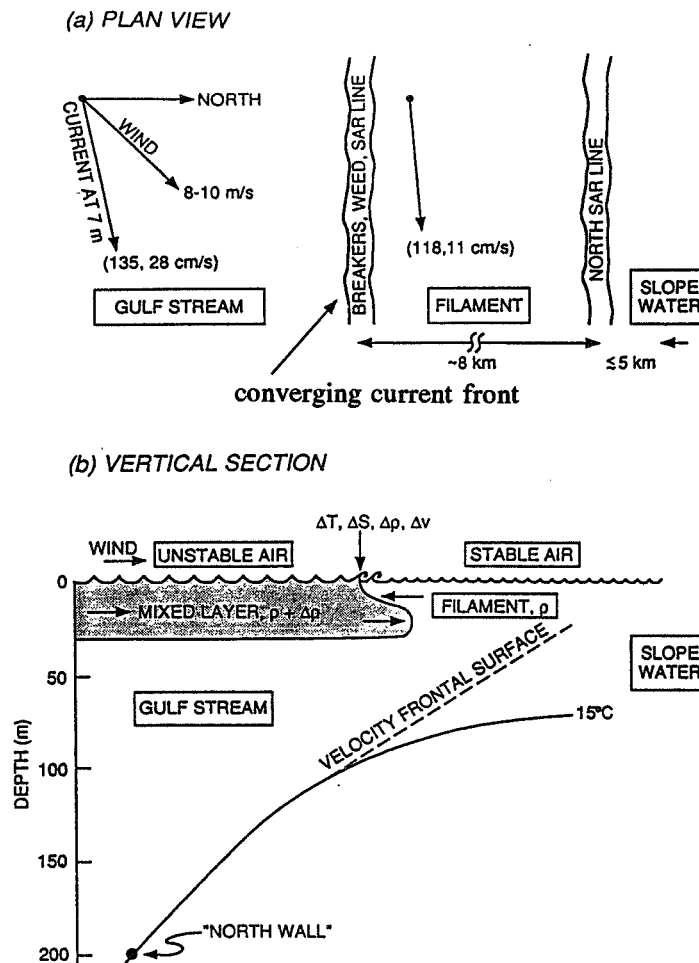


Fig. 1. Schematic summary of the observations. Plan view (a) shows the east-west surface front between Gulf Stream and low-salinity filament. Slope-Water lies farther to the north. Vertical section (b) indicates relative cross-front current motion and surface convergence. Water-current interaction produces narrow band of steep and breaking waves appearing in the SAR imagery.

### 3. POLARIMETRIC SAR MEASUREMENTS

The AIRSAR imaged the north edge of the Gulf Stream with quad-polarizations (HH, HV, VH, and VV) of P-Band (68 cm), L-Band (24 cm) and C-Band (5.7 cm) simultaneously. For each band, the four polarization channels are processed to form SAR images, and then converted to the Mueller matrix. For speckle reduction and data compression, four Mueller matrices of pixels in the azimuthal direction are averaged to form 4-look processing. The pixel spacing is 12.0 meters in azimuth and 6.7 meters in slant range. The typical image covers an area of 12.4 km in azimuth and 9 km in slant range. The incidence angle varies across an image from 10 to 65 degrees. We also obtained two scenes using a newer JPL 16-look processor. The 16-look data provides higher image quality with better focusing and less speckle noise. The resolution remains the same as in the 4-look cases. Our analysis has concentrated on the 16-look data.

Several flight paths of the AIRSAR crossed the convergent front several times, providing valuable data for analysis. A north-south pass was investigated (AIRSAR data: CM3597), and it was found that the cross-pol (HV) signature of the front are much higher than co-pol responses (VV and HH), and that P-Band HV has the highest signal-to-background ratio. To quantify the radar cross sections, a cut was made across the convergent front at an incidence angle of 47°. Fifty samples are averaged to reduce speckle. Fig. 2 shows the radar cross section,  $\sigma$ , for all three frequencies and for all three polarizations. Cross sections at VV are the highest, 3-8 dB lower at HH, and 9-18 dB lower at HV. For all three bands, the HV signal-to-background ratio,  $\delta\sigma$ , for the convergent front is much higher ( $\approx 2$  dB) than those of HH and VV ( $\approx 0.5$  dB), and P-Band HV has the highest  $\delta\sigma$ , followed by L-Band and C-band. The spatial width of the  $\delta\sigma$  peak is wider for P-band than for L- and C-band, but the peak value for P-band is less than for L-Band. These effects are caused by the longer SAR integration time for P-band. When the integration time is longer than the ocean wave coherence time, it causes smear in the azimuthal direction. It is interesting to note that P-band VV has a very weak signature. The presence of strong signatures in HV polarization indicates that strong wave-current interaction is producing large surface tilts in the along-track direction.

### 4. OCEAN SURFACE SLOPE MEASUREMENT

The polarization signature was introduced by *van Zyl et al* (1987) to graphically represent the variation of scattering cross-section as a function of the ellipticity and orientation angles of the transmitted waves. It is a useful technique for describing the scattering mechanism of point and distributed targets. For idealized Bragg scattering, the scattering matrix can be represented by

$$S_{Bragg} = \begin{bmatrix} a & 0 \\ 0 & b \end{bmatrix} \quad (1)$$

where  $a$  and  $b$  are real, and  $b > a$  (i.e.,  $\sigma_{vv} > \sigma_{hh}$ ). The HV and VH polarization responses are zero. Using the polarimetric SAR data (CM3597), for incidence angles between 20° and 65°, co-polarization signatures of all three bands display the same characteristics as Bragg scattering. For incidence angles below 20°, specular scattering becomes dominant.

For Bragg scattering, maximum co-polarization signatures occur at an orientation angle  $\psi = 90^\circ$ , and ellipticity angle  $\chi = 0^\circ$  (i.e., at VV-polarization). However, a tilted ocean surface in the azimuth direction introduces HV and VH components, and causes a shift of the location of the maximum response in the co-polarization signature away from  $\psi = 90^\circ$ . The amount of shift from  $\psi = 90^\circ$  correlates with the slope of the tilted surface. Intuitively, the maximum co-pol response occurs when the vertical antenna is perpendicular to the ocean surface in the azimuth direction. The surface tilt causes the shift of the maximum response away from the vertical position. The amount of shift can be visualized as the rotation

of the vertical-horizontal basis vectors to an angle where the vertical component is again perpendicular to the tilted surface. This phenomenon has been utilized by *Schuler et al.* [13] for slope measurements of mountainous desert terrain, where the Bragg scattering mechanism is also dominant.

This new slope measurement technique is applied to the same data of Fig. 2. to measure the slope change across the converging currents. The ideal Polarimetric SAR imaging alignment for this slope

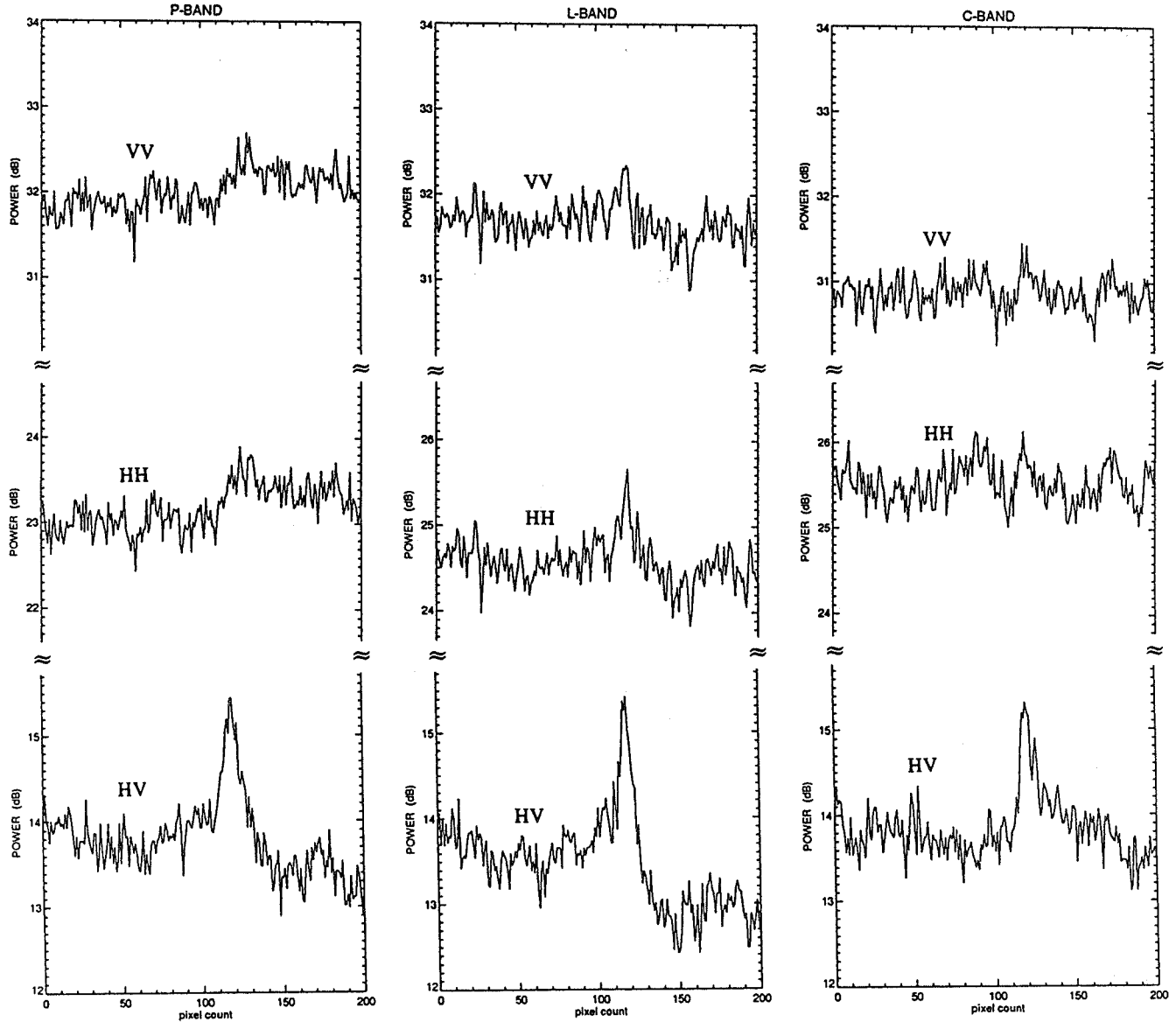


Fig. 2 To quantify the radar cross sections of the convergent front, a cut was made across the convergent front at an incidence angle of  $47^\circ$ . Fifty samples are averaged to reduce speckle. The radar cross section,  $\sigma$ , for all three frequencies and for all three polarizations are shown. The azimuth pixel size is 12m, and the distance covered is 2.4 km (200 pixels). Cross sections at VV are highest, 3-8 dB lower at HH, and 9-18 dB lower at HV. For all three bands, the HV signal-to-background ratio,  $\delta\sigma$ , for the convergent front is much higher ( $\approx 2$  dB) than those of HH and VV ( $\approx 0.5$  dB), and P-Band HV has the highest  $\delta\sigma$ , followed by L-Band and C-band.

measurement is to have the front aligned in the range direction. The AIRSAR CM3597 image is one of the data that possesses this alignment. The P-Band polarimetric data is used to compute the orientation angle of the maximum co-pol response for each pixel. The result for the lower right quarter of data is shown as an image in Fig. 3. This figure displays a sudden slope change encoded as a gray-scale change at the convergent front. The *R/V Henlopen* is crossing the front with its wake in a contrasting dark slope. To quantify the slope change at the front, a 50-line average below the ship (at incidence angle= $47^\circ$ ) is plotted in Fig. 4A. It clearly shows that the surface slope is positive north of the front, negative or near zero south of the front, and a maximum at the front. The estimated slope at the front has an abrupt change from an average of  $+0.8^\circ$  to  $-0.5^\circ$  as shown in Fig. 7. In our experiments, we have found that the shift in orientation angle induced by the surface tilt depends on incidence angle and the  $\sigma_{hh}$  to  $\sigma_{vv}$  ratio.

Similar results were also obtained for L-band (Fig. 4B), except that it is noisier. C-Band with its shorter wavelength is more subject to local wave variations, the noise level is much too high. For this application, P-band polarimetric SAR is preferred.

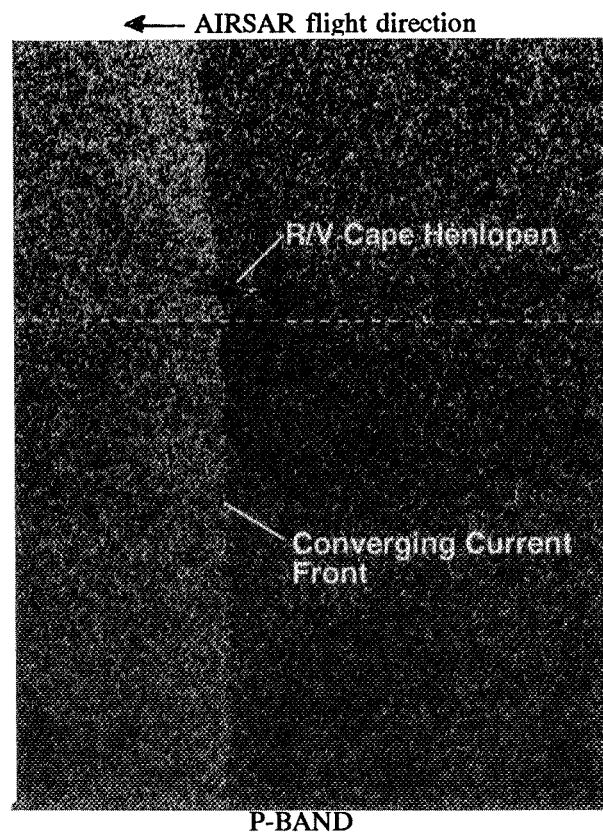
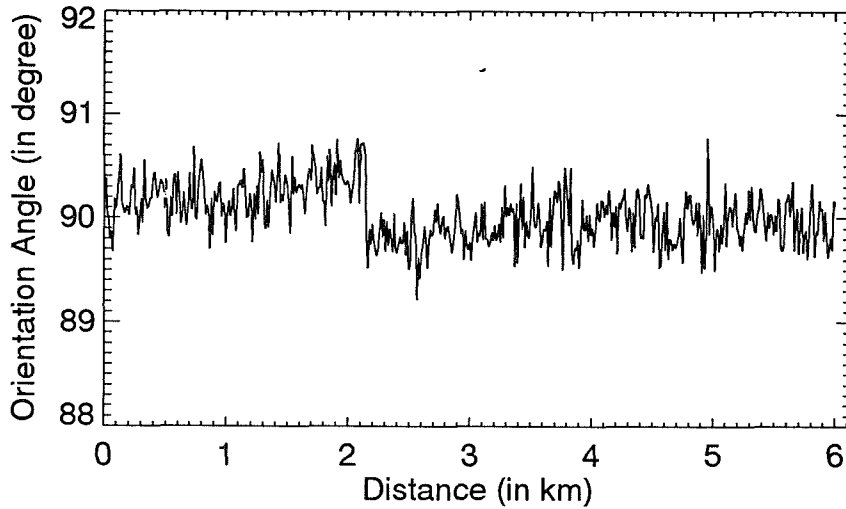
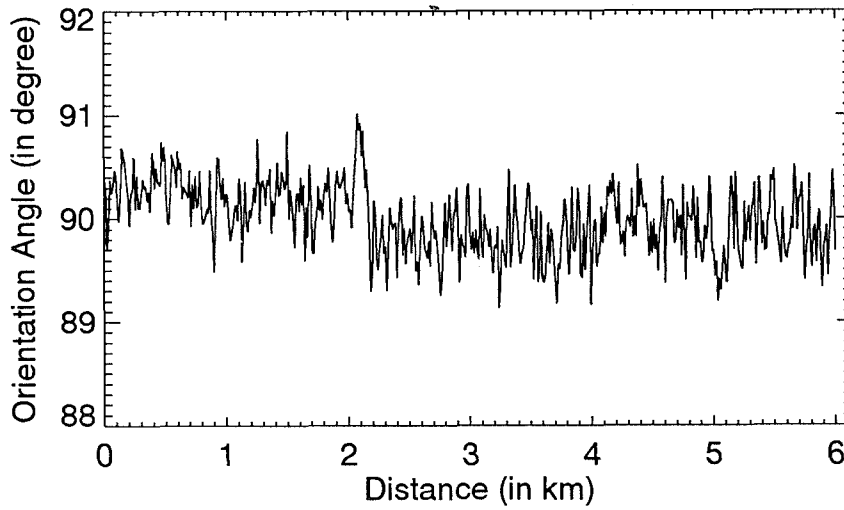


Fig. 3 The polarimetric SAR measured surface slopes around the convergent front is shown as a gray-level image. The slope is computed for each pixel by the shift from  $90^\circ$  of the polarization orientation angle associated with the maximum co-polarization signature. The sudden change in slope at the front demonstrated the effectiveness of this algorithm.



(A) P-BAND



(B) L-BAND

Fig. 4 A 50-line average of the orientation angles at the dotted line of Fig.3 (incidence angle= $47^\circ$ ) is plotted. The orientation angle of  $90^\circ$  corresponds to  $0^\circ$  surface tilt. It clearly shows that the surface slope is positive north of the front, negative or near zero south of the front, and a maximum at the front.

## 6. REMARKS:

The procedure of finding the maximum polarization signature follows a specially devised scheme that accelerates the computation and improves the accuracy. This procedure (*Schuler, Lee and De Grandi, 1995*) is based on the method of steepest ascent, and uses iterative methods to locate the maximum. It was found that this method can achieve the orientation angle accuracy of  $0.01^\circ$ .

The polarization orientation angle shift for a given surface tilt is incident angle and HH to VV ratio dependent. For a given incident angle and HH to VV ratio, a theoretically derived function relates

the shift of orientation angle to the surface tilts. This function is then applied to map the polarimetric SAR orientation angle shifts into surface tilts.

## 7. Conclusions

The polarization and wavelength diversity of radar signatures associated with narrow Gulf Stream current fronts have been investigated using the P-, L-, C-Band airborne polarimetric SAR data. Using the polarization signatures, a new procedure has been formulated to estimate the change in mean slope across the front. NASA/JPL AIRSAR data is used for demonstration.

## Acknowledgement:

We would like to thank Dr. J. van Zyl of JPL for his helpful comment on the slope measurement by polarimetric SAR. We also thank the NASA/JPL AIRSAR team for providing polarimetric SAR data, and Dr. G. Valenzuela and Dr. G.O. Marimorino for their contributions in organizing the Gulf Stream Experiment. Preparations of this paper was supported by the NRL Polarization and Wavelength Diversities of SAR Imaging and the Polarimetric SAR for Coastal Remote Sensing Programs.

## References:

- Alpers, W.R. D.B. Ross, and C.L. Rufenach, "On the detectability of ocean surface waves by real and synthetic aperture radar," JGR, 86, 6481-6498, 1981.
- Cox, C. and W. Munk, "Statistics of sea surface derived from sun glitter," J. Mar. Res. vol.13, pp. 198-227, 1954.
- Hasselmann, K., R.K. Raney, W.J. Plant, W. Alpers, R.A. Shuchman, et al., "Theory of synthetic aperture radar imaging of ocean waves," JGR, vol. 90, pp.4659-4685, 1985.
- Marmorino, G.O., et al., "Gulf Stream Surface Convergence Imaged by Synthetic Aperture Radar," JGR, 99(C9), 18315-18328, September 15, 1994.
- Schuler, D. L., J.S. Lee and K.W. Hoppel, "Polarimetric SAR Image Signatures of the Ocean and Gulf Stream Features," IEEE Trans. Geo. Sci. Rem. Sen., vol.31, no.6, pp.1210-1221, Nov. 1993
- Schuler, D. L., J.S. Lee and G. De Grandi, "The Measurement of Topography Using Polarimetric SAR Images" Submitted to the IEEE Trans. Geoscience and Remote Sensing.
- Valenzuela, G.R., "Scattering of electromagnetic waves from a tilted slightly rough surface," Radio Sci., vol.11, no. 3, pp. 1057-1066, 1968.
- Valenzuela, G.R., et al., "The July 1990 Gulf Stream Experiment," Proceedings of IGARSS'91, pp.119-122, June 1991.
- van Zyl, J.J., H.A. Zebker and C. Elachi, "Imaging radar polarization signatures: Theory and observations," Radio Science., vol. 22, no. 4, pp.529-543, 1987.



**Page intentionally left blank**

# **THE NASA/JPL AIRBORNE SYNTHETIC APERTURE RADAR SYSTEM**

Yunling Lou, Yunjin Kim, and Jakob van Zyl

Jet Propulsion Laboratory  
California Institute of Technology  
4800 Oak Grove Drive, MS 300-243  
Pasadena, CA 91109  
Tel: (818) 354-2647  
Fax: (818) 354-0495  
E-mail: lou@blacks.jpl.nasa.gov

## **INTRODUCTION**

The NASA/JPL airborne SAR (AIRSAR) system operates in the fully polarimetric mode at P-, L- and C-band simultaneously or in the interferometric mode in both L- and C-band simultaneously. The system became operational in late 1987 and flew its first mission aboard a DC-8 aircraft operated by NASA's Ames Research Center in Mountain View, California. Since then, the AIRSAR has flown missions every year and acquired images in North, Central and South America, Europe and Australia.

In this paper, we will briefly describe the instrument characteristics, the evolution of the various radar modes, the instrument performance and improvement in the knowledge of the positioning and attitude information of the radar. In addition, we will summarize the progress of the data processing effort especially in the interferometry processing. Finally, we will address the issue of processing and calibrating the cross-track interferometry (XTI) data.

## **INSTRUMENT CHARACTERISTICS**

In AIRSAR, transmit polarization diversity is achieved by alternately transmitting the signals using horizontal or vertical polarizations. Receive polarization diversity is accomplished by measuring six channels of raw data simultaneously, both H and V polarizations at all three frequencies. The video data are digitized using 8-bit ADCs, providing a dynamic range in excess of 40 dB and, together with navigation data, stored on tape using high density digital recorders. The AIRSAR system also includes a real-time processor capable of processing any one of the 12 radar channels into a scrolling image. In addition to checking the health of the radar, the scrolling display is also used to ensure that the correct area has been imaged. Table 1 provides a summary of the AIRSAR system characteristics. AIRSAR can be operated in many different modes due to the complexity and flexibility of the instrument. The evolution of these radar modes is summarized in the following section.

Table 1. Summary of AIRSAR system characteristics. The parameters in ( ) apply to 40 MHz chirp bandwidth configuration.

	P-band	L-band	C-band
Chirp Bandwidth (MHz)	20 (or 40)		
Chirp Center Freq. (MHz)	438.75 (427.5)	1248.75 (1237.5)	5298.75 (5287.5)
Peak Transmit Power (dBm)	62	67	60
Antenna Polarization	H/V dual microstrip		
Antenna Gain (dBi)	14	18	24
Azimuth Beamwidth (deg)	19.0	8.0	2.5
Elevation Beamwidth (deg)	38.0	44.0	50.0
Antenna Size (m)	0.9 x 1.8	0.5 x 1.6	0.2 x 1.4
ADC Sampling Rate (MHz)	45 (90)		
Data Rate (MB/s)	10		
NE Sigma0 (dB)	-45	-45	-35
Nominal Altitude (m)	8000		
Nominal Velocity (Knots)	450		
PRF/Polarization Channel	1 (programmable) x ground speed in Knots		
Slant Range Resolution (m)	10 (5)		
Azimuth Resolution (m)	1		
Ground Range Swath (km)	10 - 15		

## RADAR MODES

When AIRSAR flew its first scientific mission in 1988, it was capable of imaging sites in P-, L-, and C-band simultaneously in polarimetric mode or L- and C-band along-track interferometric (ATI) mode. ATI mode was successfully used to image ocean currents and waves moving in the radar line-of-sight direction. Since then, more antennas and antenna switching networks have been installed to accommodate cross-track interferometric (XTI) and bistatic modes. XTI mode was successfully used to generate topographic maps of areas of interest whereas the bistatic mode was successfully used to collect data in conjunction with ERS-1 (CVV) and SIR-C (LVV and CVV). Figure 1 shows the relative location of all the antennas currently available on the DC-8 and their polarization. Table 2 summarizes the evolution of these radar modes.

As shown in Table 2 and Figure 1, the baseline of the C-band ATI mode was shortened significantly in 1991 by pairing up the newly added C-bt antenna with the C-SAR antenna in an effort to increase the sensitivity to shorter decorrelation time of ocean currents. Prior to 1995, the single frequency XTI mode (XTI1) was operated with one transmit antenna that provides the best possible SNR. The reason is that the transmit path via the C-tp antenna is 3 m shorter than that of the C-bt antenna, hence giving us better SNR. Since 1995, we have been experimenting with alternating the transmit antenna between the top and the bottom antennas. This effectively doubled the baseline and initial data analysis showed that the longer baseline produced DEMs (digital elevation models) with reduced RMS height error as expected. In addition, the newly added L-band XTI mode produced DEMs of slightly higher RMS height error due to shorter baseline length (scaled by wavelength) compared to those of C-band XTI mode, although much work remains to be done to calibrate the L-band XTI mode.

To produce accurate DEMs, we need to know the baseline precisely. To do this, we have also upgraded the Inertial Navigation System (INS) and the Global Positioning System (GPS) receiver in order to have more accurate knowledge of the location and attitude of the antennas. The upgrades are described in the next section.

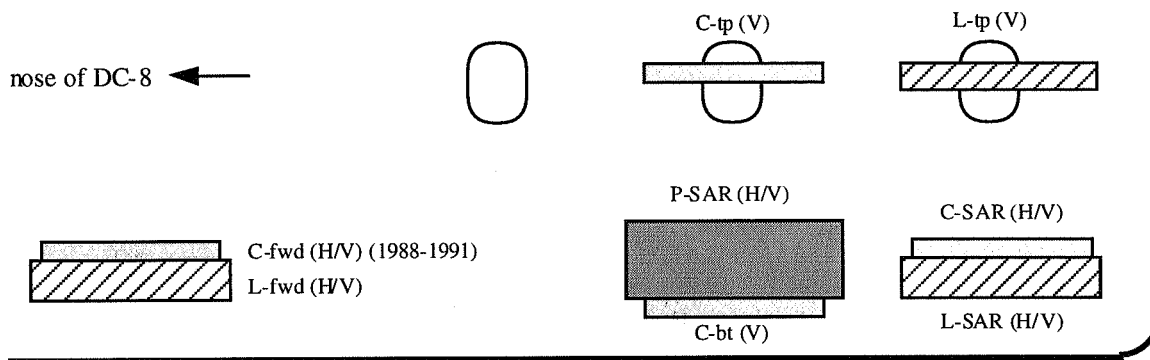


Figure 1. View of relative location of the antennas (not to scale).

Table 2. Summary of the available radar modes for AIRSAR. \* Since 1994, P-band is allowed to transmit in the U.S only when the radar is in 20 MHz chirp bandwidth mode. If special clearance is obtained prior to the flight, P-band is then allowed to transmit in 40 MHz chirp bandwidth mode also.

Mode	Date	P-band*		L-band		C-band	
		TX	RX	TX	RX	TX	RX
POLSAR (quad-pol)	1988 - present	P-SAR (H/V)		L-SAR (H/V)		C-SAR (H/V)	
ATI	1988 - 1990	P-SAR (H/V)		L-fwd and L-SAR		C-fwd and C-SAR	
ATI	1991 - present	P-SAR (H/V)		L-fwd and L-SAR		C-bt (V) and C-SAR	
XTI1	1991	P-SAR (H/V)		L-SAR (H/V)		C-bt	C-bt / C-tp
XTI1	1992 - 1995	P-SAR (H/V)		L-SAR (H/V)		C-tp	C-bt / C-tp
XTI1 - ping pong	1995	P-SAR (H/V)		L-SAR (H/V)		C-bt and C-tp	
XTI2	1995	P-SAR (H/V)		L-tp	L-tp / L-bt	C-tp	C-bt / C-tp
XTI2 - ping pong	1995	P-SAR (H/V)		L-tp and L-bt		C-bt and C-tp	

## NAVIGATION SYSTEM

The original navigation system of AIRSAR consisted of a Honeywell INS with a ring laser gyro that determined the attitude of the aircraft and a Motorola Eagle 4-channel GPS receiver that provided the positioning information (latitude and longitude) of the aircraft. As technology advanced and our need for more accurate positioning and attitude information became more stringent, we purchased a new Motorola Six-Gun GPS receiver and a new Honeywell Integrated GPS and INS (IGI) in 1994. The Six-Gun GPS receiver has six channels and a much more stable clock compared to the old unit and provides positioning accuracy of 100 m using CA code. This receiver was integrated in the radar in 1994. The Honeywell IGI has a smaller and more sensitive ring laser gyro integrated with a GPS receiver capable of receiving the more accurate but restricted Precise Positioning Service (PPS) data. The specifications on this unit are:  $0.02^\circ$  heading accuracy,  $0.01^\circ$  roll and pitch accuracy, 0.03 m/s velocity accuracy per axis, and 16 m positioning accuracy with PPS. The IGI was installed on the DC-8 in 1994 but the data were recorded off-line and were not available in the radar header until the 1995 flight season.

In addition, we have also experimented with differential GPS by using a Turbo Rogue GPS receiver on the aircraft in conjunction with another Turbo Rogue receiver on the ground. This experiment is usually supported by the GPS experts from another section at JPL and requires special post-processing to obtain positioning accuracy of better than 1 m.

## DATA PROCESSING

A variety of processors and processing techniques are utilized to process AIRSAR data to imagery. A real-time correlator is part of the AIRSAR radar flight equipment (the Aircraft Flight Correlator) and is used to produce low resolution (approx. 25 meter) two look survey imagery. The same on-board equipment is used to generate a slightly higher resolution (15 meter), 16 look image of a smaller area (12 km x 7 km) within 10 minutes of acquisition using the quick-look processor. These on-board processors are useful for assessing the general health of the radar and the success of data taking in real time.

Final processing of selected portions of the data to high quality, fully calibrated image products happens in the weeks and months following a flight campaign. Currently, users may request images from two different operational processors, the synoptic processor and the frame processor. In the synoptic processor, the user specifies three data channels to be processed. About five minutes of raw data from each of the three selected channels are processed to 16 looks and amplitude-only image strips, covering about 40 km along track. In 40 MHz mode, the image strips would be 8 looks and 20 km long. These image strips cover about 9 km in the slant range direction for the 20 MHz mode and 4.5 km for the 40 MHz mode.

In terms of frame processing, we currently support two processor versions: the AIRSAR processor (version 3.5x) and the new integrated processor (version 5.x), which is still under development (especially in XTI calibration). 1995 has been a transition year for the AIRSAR ground processing facility. The new integrated processor was developed mainly to process XTI data routinely since XTI mode has become increasingly popular. In order to do so, we needed a new processor that tracks and compensates for the motion of the aircraft since uncorrected motion translates into baseline error between the two antennas, which results in height error in the DEM. In addition to motion compensation, the new integrated processor is also capable of generating images with full range swath as

opposed to half range swath with the version 3.5 processor. The XTI processor still needs an accurate algorithm to determine absolute phase. In addition, better calibration is required to remove systematic height errors in DEM.

As with the previous version, the integrated processor processes one minute of raw data of all available data channels into absolutely calibrated images in compressed Stokes matrix format that contains all the polarization information. If C-band cross-track interferometer data are available for the data take, the integrated processor will generate a digital elevation model and a local incidence angle map. By using the local incidence angle map, all output images will be geometrically and radiometrically corrected taking the topography into account and resampled to ground range with a 10 m by 10 m pixel spacing. The output images cover about 10-12 km in the range direction by about 10 km in the along-track direction for the 40 MHz mode, and about 20 km in the range direction by about 10 km in the along-track direction for the 20 MHz mode. Although the radar data rate allows us to image about 20 km in range swath for the 20 MHz mode, the increasing phase noise due to decreasing SNR as a function of incidence angle reduces the correlation between the two antenna channels. As a result, the RMS height error can be quite large in far swath due to poor SNR.

## **DATA CALIBRATION**

The calibration of polarimetric data is well understood. Briefly, with the calibration tone in the receive chain and corner reflector verification, we are able to consistently produce polarimetric images with better than 3 dB absolute accuracy, better than 1.5 dB relative accuracy amongst the 3 radar frequencies, and better than 0.5 dB between the polarization channels. The relative phase calibration between the HH and VV channels is better than  $10^\circ$ .

The calibration of XTI data is much more challenging because various parameters, such as baseline vector, are involved in the XTI data processing. The absolute phase must be known in order to derive height information from the interferometric data without  $2\pi$  ambiguity. The differential phase (between two channels) of the radar can be a function of system temperature. Therefore, we need to determine both absolute and differential phase for each data take. In addition, accurate knowledge of the baseline between the two antennas to a few millimeters is necessary to generate accurate DEMs. We have successfully used the corner reflector array at Rosamond Dry Lake to determine the baseline for C-band antennas and are currently working on the L-band antennas that we started operating in 1995.

## **SUMMARY**

In this paper, we described the AIRSAR instrument characteristics, the evolution of the various radar modes, and improvement in the navigation system. In addition, we summarized the progress of the data processing effort and briefly addressed some of the challenges in calibrating the XTI data. We hope to resolve the phase calibration issues with the 1995 dual frequency XTI data in the near future so that we can provide users with DEMs at L- and C-band routinely.

## **ACKNOWLEDGMENT**

The research described in this paper was carried out by the Jet Propulsion Laboratory, California Institute of Technology, under a contract with the National Aeronautics and Space Administration.

# **ON THE CAPABILITIES OF USING AIRSAR DATA IN SURFACE ENERGY/WATER BALANCE STUDIES**

Jose F. Moreno<sup>(\*)</sup> and Sasan S. Saatchi  
Jet Propulsion Laboratory, California Institute of Technology, MS 300-243  
4800 Oak Grove Drive, Pasadena, CA 91109-8099  
Tel. 818-3543865, Fax: 818-3936943, E-mail: moreno@blacks.jpl.nasa.gov

(\*) on leave from: Remote Sensing Unit - Faculty of Physics, University of Valencia,  
46100 Burjassot, Valencia, Spain

## **1. INTRODUCTION**

The capabilities of using remote sensing data, and in particular multifrequency/multipolarization SAR data, like AIRSAR, for the retrieval of surface parameters, depend considerably on the specificity of each application. The potentials, and limitations, of SAR data in ecological investigations are well known. Because the chemistry is a major component in such studies and because of the almost lacking chemical information at the wavelengths of SAR data, the capabilities of using SAR-derived information in such studies are considerably limited. However, in the case of surface energy/water balance studies, the determination of the amount of water content, both in the soil and in the plants, is a major component in all modeling approaches. As the information about water content is present in the SAR signal, then the role of SAR data in studies where water content is to be determined becomes clearly predominant.

Another situation where the role of SAR data becomes dominant over other remote sensing systems is the case of dense canopies. Because of the penetration capabilities of microwave data, which is especially superior as compared to optical data, information about the canopy as a whole and even the underlying soil is contained in the SAR data, while only the top canopy provides the information content in the case of optical data. In the case of relatively dense canopies, as has been demonstrated in this study, such different penetration capabilities provide very different results in terms of the derived total canopy water content, for instance.

However, although all such capabilities are well known, unfortunately there are also well known limitations. Apart from calibration-related aspects (that we will not consider in this study), and apart from other intrinsic problems (like image noise, topographic corrections, etc.) which also significantly affect the derived results, we will concentrate on the problem of extracting information from the data. Even at this level, methods are still not fully well established, especially over vegetation-covered areas.

In this paper, an algorithm is described which allows derivation of three fundamental parameters from SAR data: soil moisture, soil roughness and canopy water content, accounting for the effects of vegetation cover by using optical (Landsat) data as auxiliary. Capabilities and limitations of the data and algorithms are discussed, as well as possibilities to use these data in energy/water balance modeling studies.

All the data used in this study were acquired as part of the Intensive Observation Period in June-July 1991 (European Multisensor Aircraft Campaign-91), as part of the European Field Experiment in a Desertification-threatened Area (EFEDA), a European contribution to the global-change research sponsored by the IGBP program (Bolle et al., 1993).

## **2. PARAMETERS WHICH ARE REQUIRED IN SURFACE ENERGY/WATER BALANCE STUDIES**

Although the actual parameters which are required in surface energy/water balance studies depend very much on the kind of modeling approach adopted in each case, it is a general agreement that accounting for the amount of water available, and changes in water content, both in the soil and in the plants, is always a major component, not only for water balance but also for the partitioning of available energy into latent and sensible heat flux components. However, the way in which each parameter enters into the model and the assumptions made by each model are always conditioning the so called 'sensitivity' to such model parameters. For this reason, accuracy requirements on the retrievals of each parameter can not be easily stated.

The model used in previous studies (Moreno et al., 1994), which was actually a derivation from the Biosphere-Atmosphere Transfer Scheme (BATS) (Dickinson et al., 1993) with significant modifications and additions, used a total of about 70 parameters (many of them fixed to default values), from which about 15 are potentially derivable from remote sensing data, and about half of them directly from SAR data or by combination of SAR data with optical data. Such parameters are: (top-)soil moisture, soil roughness, canopy water content, Leaf Area Index, vegetation height (displacement height), Stem Area Index-Canopy 'roughness' (or canopy geometry parameters), soil



albedo as a function of soil moisture (see Fig. 4), as well as other parameters indirectly derived from image-classification results. Other parameters (like surface temperature, cloudiness, etc.), are also used, but will not be discussed here.

Because of the complexity of intervening effects, no definite limits can be put *a priori* for the accuracy requirements over each parameter, and then no fixed limits are put over the capability to provide soil moisture or other parameters from remote sensing data, partly because the use of this kind of data (spatial data) would also require re-parameterization in the models (the problem of handling spatially distributed data is another reason for the difficulties in deriving clear conclusions from 1D-model sensitivity studies). As the final desired goals (errors of about  $10 \text{ Wm}^{-2}$  for the derived fluxes) are still far from the actual capabilities (including ground-based meteorological networks), all we can do is to try to achieve the maximum accuracy possible. Also, the present situation is that the models (including 3D models) use very poor surface parameterization because of the lack of any additional data, so that any information which can be provided from remote sensing systems (with all the involved limitations) would still be in any case very welcome.

### 3. CAPABILITIES OF SAR DATA TO PROVIDE THE REQUIRED PARAMETERS

The capabilities of SAR data to provide at least some of the parameters required by surface energy/water balance models, especially those related to water content, are well known, and actual use of these data has been made in previous field experiments (FIFE, EFEDA, HAPEX). The way in which this has been done is mainly through model-inversion techniques. However, the kind of model used (and we actually do not have an appropriate model for the behaviour of natural surfaces at the frequencies at which SAR data are acquired), and the kind of inversion technique used, become critical when retrieved numerical values are to be compared to ground measurements. As the SAR signal sensitivity to water content in the canopy, and also in the soil, has been in any case demonstrated (Engman, 1991), it is expected that this information will come out in the retrievals derived from SAR data, at least in terms of relative values.

The use of full-polarimetry information for the retrieval of soil/vegetation parameters has been demonstrated to be an essential aspect as compared to the capabilities of single channel/single polarization systems (like ERS-1/2). Because of the ability of polarimetric information to separate different contributions, roughness/geometry effects and water content information can be decoupled, and then the corresponding values retrieved from the measured data.

Apart from the classical parameters derived from polarimetric information, information about canopy roughness (mainly related to canopy height) can be also derived from interferometric information. However, because the physical meaning of canopy roughness (which is also a recurrent function of wind speed) cannot be easily related to such interferometric information, work in this field is still in its beginning. Phase information in standard polarimetric data can also be related to canopy geometry, but the link between such estimates and the required parameters (canopy height and displacement height, canopy 'roughness') is still at the level of empirical relationships. The penetration capabilities of SAR data become here a difficulty, because it is the canopy height which is expected to be given as input to the models. However, the actual canopy roughness is not simply related to vegetation height, and most probably the roughness information derived from the scattering mechanism in SAR data is more relevant for modeling purposes than the use of a fraction of the total canopy height as a roughness estimator, as is currently being done in the models.

It is true that AIRSAR data alone still have limitations in this type of study because of the ambiguity in scattering mechanisms in (dry) bare soil surfaces and in surfaces with small vegetation amount. The combination of information derived from optical data (where the separability between soil and vegetation behaviour is more strict, see Fig. 3), with AIRSAR data, significantly improves the capabilities of the retrievals of the required information.

Two main aspects are in any case to be taken carefully into account: data preprocessing aspects (becoming critical for any posterior analysis of the data), and the kind of information-extraction technique used to derive the required parameters from the data. Both will be discussed in the following sections.

### 4. DATA PRE-PROCESSING

In any study in which theoretical physically-based scattering models are to be inverted against measured data, the calibration of such measured data becomes critical. The reason is that the models are based on physical coefficients which are supposed to be of universal applicability. The way in which such parameters come into the model (usually through highly non-linear relationship) makes impossible the introduction of some kind of (linear) compensation for calibration deviations, so that irremediably any calibration error (including deviations in antenna gain pattern correction for varying altitude/topography and any other related radiometric correction) produces absolute errors in the retrievals by using the theoretical model. For the data used in this study, calibration was done

according to standard techniques at JPL. A total of four corner reflectors were deployed in the study area during the AIRSAR overflight, and their response was used to check calibration in the data and to perform the proper corrections when needed.

The synthesized images were geometrically rectified to ground-range projection by using available ephemeris data for the DC-8 aircraft navigation, while at the same time azimuth/range pixel sizes were compensated for to make square the resulting pixels through cubic convolution. Finally, the images were resampled by using about 50 ground control points in the common 10 m UTM grid, covering the 10×10 km<sup>2</sup> area, to which all remote sensing data were co-registered into the image database to make possible the use of multisensor/multitemporal studies. As in the resulting geometrically corrected image, pixel numbering loses the information of the incidence angle, a new image with the corresponding incidence angle for each new UTM pixel was also produced to facilitate additional processing. Although accurate Digital Elevation Models are available for the area, specially developed as part of the EFEDA experiment, because the study area considered here is completely flat (maximum height differences of less than 20 m and almost constant slope over the full area), no topographic corrections have been applied.

## 5. MODEL INVERSION TECHNIQUES APPLIED TO MULTI-PARAMETER RETRIEVAL FROM SAR DATA

The first approach that we considered in the derivation of surface parameters from SAR data was merely empirical, based on correlation approaches between some "indices" (band and/or polarization combinations) and measured surface parameters (LAI, biomass, canopy water content, etc). Different band ratios (mainly L/C and P/L) and polarization ratios (HH/VV, HH/HV, VV/HV) have been considered. Although not intended to be used for the actual retrieval of surface parameters from the data, the establishment of empirical relationships allows a preliminary estimation of the capabilities of the data to account for the observed variability (and the determination of error bounds which can be expected and used in the fitting of the 'merit function' in the numerical inversion procedure) as well as the derivation of simple relationships to be used in the initialization of the model parameters in the iterative inversion procedure used later for parameters' retrieval. Although the advantages of empirical relationships are well known in terms of speed in calculations and avoidance of convergence and other numerical problems, the use of empirical relationships is absolutely limited by how well one can extrapolate from the results and the generality of the algorithms. Then, even if the use of empirical relationships could provide an optimum fit in our case where we have ground measurements of all surface parameters, the use of such empirical methods has been avoided and they have been restricted to be used as auxiliary elements in the numerical model-inversion procedure.

The central part of this study is the development of a model-inversion technique to extract the required information from SAR data. The details of the method are given elsewhere (Saatchi et al., 1993; Moreno et al., 1994; Moreno, 1995; Moreno and Saatchi, 1996), and only the main aspects will be described here.

For the contribution of bare soil, several models have been considered in this study. A model developed by Dubois et al. (1994) was initially used (Saatchi et al., 1993). Another semi-empirical model developed by Oh et al. (1992) has been also used. The present implementation is an updated version of the Oh et al. algorithm after more recent improvements introduced by the same authors. The results obtained for bare soil moisture are indeed in agreement with the results obtained by other authors (Oevelen et al., 1995) by using the Integral Equation Model over the same dataset. As a major effort is put on the derivation of canopy parameters, because the model is intended to be used over agricultural areas with significant vegetation cover for some fields, the parameterization of the soil has to be kept to a minimum in order to make the model actually invertible.

For the derivation of canopy parameters, the model has been implemented with a layer of randomly distributed scattering elements over the underlying bare soil. Such a layer represents the vegetation contribution. Three types of scattering mechanism are then considered: volume scattering, surface-volume scattering and soil surface scattering. The direct scattering from the soil is also attenuated (twice) because of the presence of the canopy, and such attenuation must be also included in the model. The surface-volume scattering terms must be introduced because of the type of vegetation to be considered in this case, giving significant contributions only for the co-polarized terms. The backscattering coefficients for the canopy are obtained by using the distorted Born approximation (Lang and Sidhu, 1983). Finally, the model needs to account for the amount of effects which are due to the soil and those which are due to vegetation in the case where no dense vegetation is considered but sparse vegetation is (and is still assumed randomly distributed at the scale of a pixel in order to avoid problems in the modeling of very clumpy structures).

An important aspect to be pointed out is the necessity of working with the original channels separately in order to minimize the problems originated by the presence of noise and in order to take full information from the data, without reductions in the dimensions of the original information. Most of the empirical approaches work with channel ratios. These channel ratios are supposed to somehow compensate for deviations in calibration and

secondary effects in the signal, but this is not absolutely true, and also these channel ratios actually enhance the noise as compared to the noise present in each channel separately. The potential advantages of using channel ratios do not compensate for the problems that the use of channel ratios introduces in the inversion procedure.

The method used for numerical inversion of the scattering model is the downhill simplex method, with two limiting conditions: maximum error and maximum number of iterations allowed. Although less robust (and especially more time consuming) than other techniques, this method has proven to be more resistant to noises and inadequacies in the model to fit the data, providing always a set of solution parameters for each pixel after avoidance of divergences.

## 6. RESULTS

Although the data used in this study correspond to only one specific situation (which prevents us from deriving general conclusions), and also the data is old as compared to the new capabilities added to the AIRSAR system in the last few years (especially in terms of data calibration), the conclusions derived from this study are similar to those previously derived in other field experiments: techniques are promising but still not fully ready for operational application, at least for the purpose of energy/water balance monitoring.

In the case of soil moisture, because of the very high sensitivity of energy/water balance models to the initialization of the soil moisture profile prior to temporal evolution calculations, the values retrieved from SAR data are not very useful for this purpose. However, those values are in good agreement with ground observations. This is especially significant over the study area used in this case, because it is a very dry area (especially in summer, when the experiment was carried out) and it still seems that the SAR signal is sensitive enough to the top-soil moisture content, provided that the effects of surface roughness variations are properly accounted for.

In the retrieval methods based on single-channel multiple-polarization techniques we have observed that in many cases the retrieved values of soil moisture at C band are considerably higher than those at L band, and this is independent of the kind of model inversion used. Because this is in contradiction with the expected behaviour (taking also into account the measured profiles given in Table 1), we have developed a double-channel multiple-polarization inversion technique (which is also actually necessary in order to account for vegetation effects in the retrievals). In the multiple-channel approach, the results are more consistent. Also, the resulting surface roughness terms are more consistent when dual channel methods are applied, especially for the correlation length. However, the use of dual-channel approaches requires that the model be applicable to both frequencies, and this is not true for some roughness conditions. In any case, the uncertainty in the retrievals of soil moisture (at least over our study area) is about 20-50% for the top-soil moisture content.

As part of the data collection for the field experiment, the soil group generated a detailed soil map of each pilot area, including soil type, soil texture, soil depth and other information. Soil density and hydrological properties were measured both in the field and in laboratory conditions, and special experiments were carried out to test the importance of spatial variability in such soil properties, even at different spatial scales, from the field level up to a network of  $10 \times 10 \text{ km}^2$  (Bolle et al., 1993; Droogers et al., 1993; Ogink-Hendriks et al., 1995). However, if all this information is used to calculate the dielectric constant of the soil for comparison with the retrievals derived by model inversion from SAR data, we are facing the problem of empirical relationships between soil moisture and dielectric constant (Hallikainen et al., 1985). Because of the large uncertainty in such relationships over varying natural conditions in the field (also coupled to high variability in surface roughness as modeled by statistical estimators based on rms heights and correlation lengths), absolute values of soil moisture must be regarded with some high probability of 'systematic' errors. However, relative values are in any case comparable, but for that purpose an independent account of the variability in intrinsic soil properties (texture, density, etc.) is needed, and this is something which is rarely available. Even when such information is available for pilot areas (as in the case of the EFEDA experiment), the way in which such information can be used in conjunction with SAR data remains unclear because of the problems of spatial scaling and scale compatibility.

In the case of canopy water content (see Fig. 2), the results are very sensitive to the geometric characterization of the canopy and the soil. The retrieved values (see for instance Fig. 2) are quite reasonable, especially taking into account that no ground data are used for training the model but only theoretical scattering considerations. However, the model was developed for the case of corn canopies in particular, and, in the present version of the algorithms, extrapolation to a full image requires some pre-classification of the scene in order to account for scattering mechanisms in a different way over different vegetation types. Work in progress is trying to eliminate this dependence by introducing additional parameters accounting for canopy geometry effects, but it seems that such geometrical effects can only be accounted for by means of multiple data taken with different incidence angles. Otherwise, separation of geometric effects from actual canopy water content will never be possible for absolute-value retrievals.

The modeling of soil roughness underlying the canopy has been demonstrated in this study to have also a major importance. An underestimation of soil roughness results in an overestimation of canopy water content.

The first trials to get information from SAR data alone resulted in difficulties in the interpretation of the retrieved values in the case of partially covered pixels. Because the soil/vegetation algorithms used in combination worked only over bare soil areas or over dense (homogeneous) vegetated areas, the cases where separation between both extreme cases was not quite obvious give wrong contributions for soil moisture and/or canopy water content. The introduction of Landsat TM data (see Fig. 1) as auxiliary information, and the use of just the fractional vegetation cover from optical data (instead of other parameters which could be also derived from Landsat data) give as a result a significant increase in the capabilities of the application of the algorithm (in terms of reduction of the number of iterations needed and avoidance of cases with no convergence as always forcing a linear solution). However, because of the difficulties in modelling partially vegetation-covered soils, the results are still questionable in such cases.

## 7. CONCLUSIONS

A key point in the results is the necessity of some spatial homogenization of the original data prior to any information-extraction technique being applied, especially in the cases where model-inversion techniques are used. Multilooking techniques (spatial average) have been demonstrated to be not enough for the purpose of deriving consistent moisture fields from the data. It is necessary to reduce the spatial resolution to about 100 m to get consistent fields over homogeneous areas, but, as the spatial resolution decreases, more difficulties are added in the inversion technique to get convergence over heterogeneous areas. Actually, as spatial resolution is decreased, the noise level is reduced, but some information is lost. However, the main impact of reducing spatial resolution is increasing the within-pixel heterogeneity and decreasing between-pixel variance. The result is that over heterogeneous pixels the model cannot be inverted because no convergence is possible or because the retrieved values are out of range for many of the resulting heterogeneous mixtures (lack of physical meaning for the model).

In order to get reliable results it is necessary to work with the highest possible spatial resolution but allow a two-way accounting for inter-pixel variability which is just due to noise: spatial filtering and multiresolution inversion techniques. The combination of both techniques is the only realistic way to handle the problem of spatial variability, especially when one of the objectives is just to analyze the problem of spatial variability in the derived surface values.

The capabilities to derive soil moisture values which can be realistically used in surface energy/water balance studies seem to be very limited, especially over dry areas, where no sensitivity to deep moisture content is present in the SAR signal but where vegetation can take water from very deep levels and still produce a considerable contribution of latent heat flux in surface energy partitioning. According to our results (see Tables 2 and 3), an uncertainty in soil moisture values between 20-50% is all we can get in the case of relatively dry areas. Note however that *in situ* measurements in controlled conditions also give uncertainties between 16% and 40% (Table 1), in the same range as the variability in the different values derived from SAR data. Even when top-soil moisture can be detected by SAR data, the use of these data in energy/water balance monitoring is still very limited in vegetated areas, because of the predominant role of root-zone moisture, as well as in the case of bare soil, where other mechanisms are determining more strongly the dynamics of water in the soil. Whatever these limitations, the SAR-derived top-soil moisture field can still be very useful to properly account for the variability of soil albedo as a function of soil moisture. In the case of soils with low albedo, variations in soil albedo due to changes in soil moisture can be up to 50% (Fig. 4). As the soil albedo has a major effect on energy balance (actually controlling the amount of energy which is available at the surface), any improvement in surface albedo retrievals (including temporal variability due to soil moisture changes) would have a dramatic impact in energy balance monitoring through modeling techniques, provided that an observation system, stable enough, could provide routine updates of systematic top-soil moisture changes.

Concerning canopy water content, the results obtained from AIRSAR data seem to overestimate the measured values of the ground according to the model used in this case. Although there are several uncertainties in the model that could explain such differences (especially those related to canopy geometry factors), it seems that the critical aspect in the model is the way in which soil scattering is treated. The overestimation in canopy water content is then mainly due to an underestimation of the roughness of underlying soil. It is interesting, on the other hand, to compare the results obtained from AIRSAR data to those obtained from optical data (Landsat TM) (see Fig. 2). In the case of Landsat TM, a full model inversion technique is also used. The model takes the reflectance values measured in the six (thermal channel 6 is excluded) Landsat channels (after radiometric calibration and atmospheric correction of the data). Then, an inversion technique is applied to fit the 6 measurements to give 6 surface parameters. One of the surface parameters used, and then retrieved by the algorithm, is the canopy water content. The values of canopy water content retrieved from Landsat data represent a strong underestimation of the values measured on the ground.

The reason for that is the sensitivity of optical data only to the top of the canopy (top leaves), so that a high underestimation is always expected from such optical data. However, fractional vegetation cover values derived from optical data are essential to guarantee proper interpretation of SAR data over partially covered areas or where confusion between soil and vegetated areas can be present in SAR data, as has been demonstrated in this study. Then, optical-microwave synergy seems to be the only way to overcome the limitations of both optical and microwave data in energy/water balance studies.

## ACKNOWLEDGMENTS

This work has been supported by the Commission of the European Union (Project EV5V-CT93-0284, DG12 DTEE) and the Spanish Inter-Departmental Commission for Science and Technology (CICYT Project AMB 94-0019-C05-CE). A portion of the research described in this paper was performed at the Jet Propulsion Laboratory, California Institute of Technology, under a contract with the National Aeronautics and Space Administration. J.F.M.'s work at JPL is supported by a grant from the Spanish Ministry of Education and Science.

## REFERENCES

- Bolle H.J., and B. Streckenbach (eds.), "The ECHIVAL Field Experiment in Desertification-threatened Areas (EFEDA)", Final Report to the Commission of the European Union, Contract EPOC-CT 90-0030, Free University of Berlin, Berlin, 1993, 461 pp.
- Dickinson R.E., P.J. Kennedy and A. Henderson-Sellers, 1993, Biosphere-Atmosphere Transfer Scheme (BATS), version 1E as coupled to the NCAR Community Climate Model, NCAR Technical Note, NCAR/TN-387, National Center for Atmospheric Research, Boulder, CO, 1993.
- Droogers P., G.D. v.d. Abee, J. Cobbaert, C.P. Kim, R. Rösslerova, M. Soet and J.N.M. Stricker, 1993, "Basic data sets description and preliminary results", Report no. 37, Department of Water Resources, Wageningen Agricultural University, Wageningen, The Netherlands, July 1993, 94 pp.
- Dubois P., and J. van Zyl, 1994, "An empirical soil moisture estimation algorithm using imaging radar", Proceedings IGARSS'94, Pasadena, CA, August 1994, pp. 1573-1575.
- Engman E.T., 1991, "Applications of microwave remote sensing of soil moisture for water resources and agriculture", Remote Sensing of Environment, vol. 35, pp. 213-226, 1991.
- Fung A.K., Zongqian Li and K.S. Chen, 1992, "Backscattering from a randomly rough dielectric surface", IEEE Trans. Geosci. Remote Sensing, vol. 30, pp. 356-369, 1992.
- Hallikainen M.T., F.T. Ulaby, M.C. Dobson, M.A. El-Rayes and L. Wu, 1985, "Microwave dielectric behaviour of wet soil - Part I: empirical models and experimental observations", IEEE Trans. Geosci. Remote Sensing, vol. 23, pp. 25-34, 1985.
- Lang R.H., and J.S. Sidhu, 1983, "Electromagnetic backscattering from a layer of vegetation: a discrete approach", IEEE Trans. Geosci. Remote Sensing, vol. 21, pp. 62-71, 1983.
- Moreno J.F., S.S. Saatchi, R.O. Green, and A.M. Jochum, 1994, "Optical-microwave data synergism to provide parameters required as inputs by surface energy balance models", Proceedings IGARSS'94, Pasadena, CA, pp. 584-586, 1994.
- Moreno J.F., 1995, "Spectral/spatial integration effects on information extraction from multispectral data: multiresolution approaches", European Symposium on Satellite Remote Sensing, Rome, Italy, September 1994, SPIE Proc., vol. 3214, pp. 324-338, 1995.
- Moreno J.F., S.S. Saatchi, 1996, "Surface information retrieval from optical/microwave data: potentials and limits of synergistic approaches", Proceedings IGARSS'96, Lincoln, Nebraska, 1996 (in press).
- Oevelen P.J. van, and D.H. Hoekman, "Radar backscattering inversion techniques for estimation of surface soil moisture content: EFEDA-Spain and HAPEX-Sahel case studies", submitted to IEEE Trans. Geosci. Remote Sensing, 1995.
- Ogink-Hendriks M.J., P. Kabat, J.A. Elbers, W.G.M. Bastiaanssen, H.G.M. van der Elsen, "Contribution to the EFEDA field campaigns in 1991 and 1994: measurements and first data analysis", Winand Staring Centre for Integrated Land, Soil and Water Research, Agricultural Research Department, Wageningen, The Netherlands, Report SC-DLO 112, 1995.
- Oh Y., K. Sarabandi, F.T. Ulaby, "An empirical model and an inversion technique for radar scattering from bare soil surfaces", IEEE Trans. Geosci. Remote Sensing, vol. 30, pp. 370-381, 1992.
- Saatchi S.S., D. Evans, P. Dubois, J. Van Zyl, "SAR experiment in desertification-threatened areas: EFEDA-Spain", JPL- D-10283, Jet Propulsion Laboratory, Pasadena, CA, March 1993.

**Table 1.** Measurements of soil moisture over a reference bare soil field used for multisensor calibrations/intercomparisons (located just at the center in Fig. 1c), during the two AIRSAR overflights over the study area. Numbers correspond, respectively, to the mean (of the N values available), standard deviation and relative error (%). The N measurements correspond to a spatial grid over the field.

Date	Soil moisture		Soil roughness	
	<i>TDR (N=29)</i>	<i>Volumetric:</i>	$\sigma$ (cm)	$\lambda$ (cm)
19 June 91 (a)		crust : $2.9 \pm 1.2$ (40%)		
"	5 cm : $3.5 \pm 0.8$ (24%)	0-5 cm : $4.9 \pm 0.9$ (19%)	1.41	4.00
"	10 cm : $7.2 \pm 1.2$ (17%)	5-10 cm : $10.9 \pm 1.8$ (16%)		
"	30 cm : $16.0 \pm 3.5$ (22%)			
14 July 91 (b)	<i>Gravimetric: (N=24)</i>			
	0-5 cm : $4.0 \pm 0.7$ (17%)			

(a) Droogers et al., 1993; (b) Saatchi et al., 1993.

**Table 2.** Derived soil moisture values and roughness parameters from AIRSAR data for the same reference bare soil where simultaneous ground measurements are shown in Table 1.

Date	Soil moisture	Soil roughness	
	<i>L band</i>	$\sigma$ (cm)	$\lambda$ (cm)
19 June 91	3.9	0.19	3.6
14 July 91	7.1	0.27	3.1

**Table 3.** Comparisons of retrieval of soil moisture by using the same AIRSAR data but applying three different models for the same reference bare soil area where simultaneous ground measurements are shown in Table 1. Data shown correspond to model inversion for L band (HH-VV and HH-VV-HV, depending on the model used in each case).

Date	Soil moisture		
	<i>Oh et al., 1992</i>	<i>Fung et al., 1992</i>	<i>Dubois et al., 1994</i>
19 June 91	11.2	5.6	6.8



(a)



(b)



(c)

**Fig. 1** Multitemporal AIRSAR data: (a) 19 June 1991 (L-HH), (b) 14 July 1991 (L-HH), and (c) Landsat TM data (derived vegetation fractional cover) for 14 July 1991, after geometric registration of the full dataset. The area corresponds to the Barrax test site, one of the pilot areas of the EFEDA experiment in Spain.

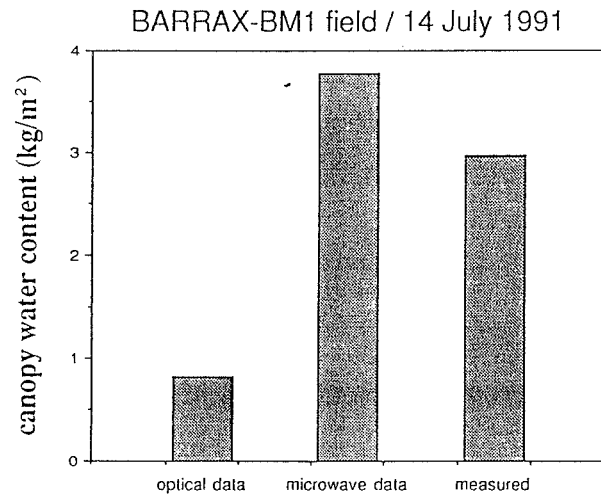


**Fig. 2** Comparison of the retrievals of canopy water content from almost simultaneous microwave (AIRSAR) and optical (Landsat TM) data. SAR data slightly overestimate the total canopy water content in this case, but Landsat data give a very low value as compared to ground measurements.

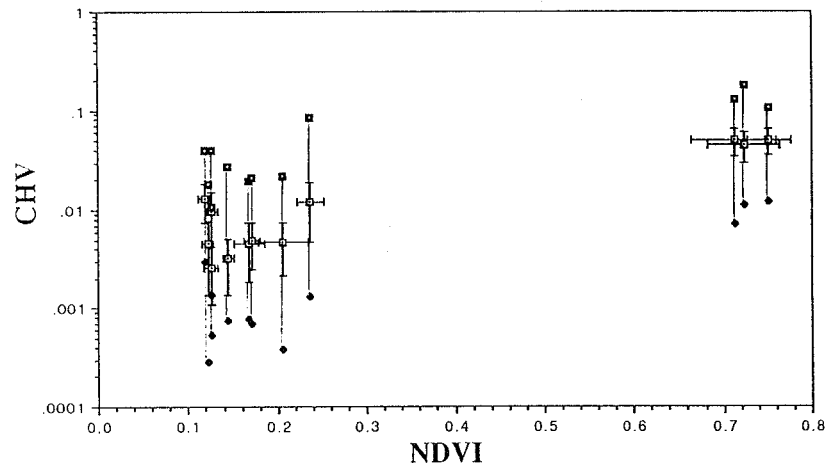


**Fig. 3** Backscattering coefficients (C-HV) as measured by AIRSAR plotted against NDVI values derived from simultaneous Landsat TM data, for all the pilot fields used in the EFEDA'91 experiment (MAC-Europe campaign). Optical data allows a better separation of bare soil and vegetated surfaces for interpretation of SAR data.

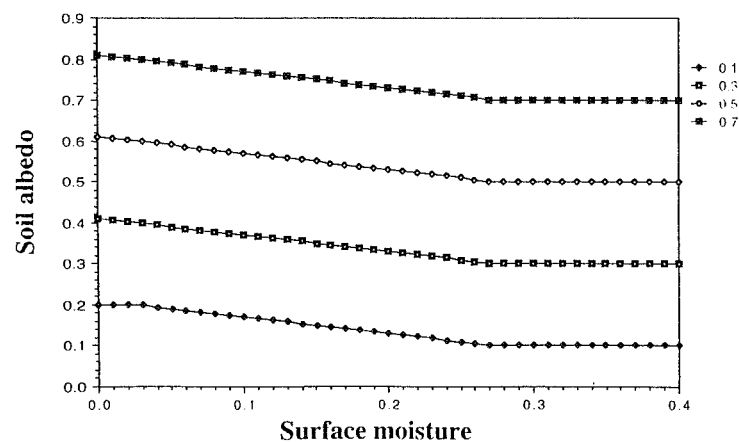


**Fig. 4** Bare soil albedo (spectral and angular integration) as a function of top-soil moisture, according to the parameterization used in the Biosphere-Atmosphere Transfer Scheme (BATS) surface energy/water balance model (numbers on labels indicate the soil albedo corresponding to saturated conditions for each curve).



**Page intentionally left blank**

# AN AUTOMATED MAPPING PROCESSOR USING C-BAND INTERFEROMETRIC SAR DATA

E. Rodriguez, T.R. Michel, J.M. Martin, B. Houshmand  
Jet Propulsion Laboratory  
California Institute of Technology

**Abstract:** We present the description of a processor which has been implemented to generate map products starting from C-band interferometric data. The first stage of the processor consists of the conventional interferometric SAR processing producing a Digital Elevation Model (DEMs) and a SAR brightness image in sensor coordinates. In the second stage of processing, a land use classification map is obtained by using the DEM, brightness, and interferometric correlation layers. Auxiliary layers which include a drainage layer, a height gradient layer, a height error layer, an estimated penetration layer, and a shaded relief layer are also computed. In the final step, all UTM collocated layers are combined in a GIS system which allows for both hard copy map products and for digital applications.

## 1. INTRODUCTION

Conventional generation of map products using stereo imaging techniques requires human intervention, making the elaboration of wide maps covering very extensive areas a daunting proposition. Recently, Interferometric SAR (IFSAR) techniques have shown the capability of producing digital elevation models (DEM) in near real time, and without operator intervention. Given the promise shown by these techniques, it is a natural extension to try to implement a processing system capable of generating digital map products automatically in near real time. The purpose of this paper is to report on such a prototype system which has been implemented at JPL for the processing of AIRSAR TOPSAR C-band interferometric data.

The goals in developing the automated mapping station described here were the following:

- 1) Automated product generation without operator intervention or editing.
- 2) Near real time processing capabilities.
- 3) Land classification from interferometric data alone.
- 4) Digital products in a GIS usable format.
- 5) Ability to produce hard copy output of standard map products.

The following section describes the JPL AUTOMAP processor which has been implemented to achieve these goals.

## 2. PROCESSOR IMPLEMENTATION

The AUTOMAP processor takes raw interferometric data (e.g., the data generated by the JPL TOPSAR radar), and produces two types of products: 1) Geolocated topographic maps; and, 2) A multi-layer GIS database which can be examined on a work station. The AUTOMAP processor can be divided functionally into four (see Figure 1):

- The IFPROC Processor: Converts raw interferometric data into heights, radar brightness, and correlation files.
- GIS Data Layer Generation: Takes the outputs from IFPROC and computes the layers which will be incorporated into the GIS database.
- Geolocated GIS Quad: Given the desired map location and size, creates a geolocated database incorporating the desired data layers.
- Map Product Generation: Makes map products suitable for printing.

The IFPROC processor has been documented elsewhere, and this manual will restrict itself to a brief overview of how it is integrated to the rest of the AUTOMAP processor.

The IFPROC module of the processor always outputs four data files which correspond to the height, brightness, correlation, and header data. Since user requirements for the output map products are variable, the rest of the AUTOMAP processor is designed for flexibility in both the output products and in the contents of the GIS database. The user can specify the desired products by using a menu, which can be filled interactively or preset prior to run time.

The processor is currently implemented in a 16-processor Silicon Graphics Power Challenge computer and a DEC Alpha work station which is used as a front-end for displaying the GIS data and printing output products. The computer intensive code is run in the Silicon Graphics computer and is written in C++, C, and FORTRAN. The commercially available package PCI is used to geolocate the data layers, do some processing steps, and display the data. PCI processing steps are run automatically using the PCI "easi" script language.

## **Terrain Classification**

The terrain classification module takes in the height, brightness, and correlation data produced by IFPROC, computes a series of data feature layers, and performs terrain classification using a mixture of Bayes classification and knowledge based algorithms. A flow diagram is presented in Figure 2.

The following is a brief description of each of the programs in the terrain classification module:

- featureVector: This program takes the three files generated by IFPROC and generates a set of user defined features to be used by the Bayes classifier. The features currently implemented are:
  - The radar brightness corrected for incidence angle, antenna pattern, and range effects.
  - The measured correlation between the two IFSAR channels.
  - The calculated "penetration" (correlation corrected for thermal noise and tilt effects). To obtain this feature, define the volumetric decorrelation,  $\gamma_Z$ , as

$$\gamma_Z = \frac{\gamma}{\gamma_G \gamma_N}$$

where  $\gamma$  is the measured correlation;  $\gamma_N$  is the decorrelation due to noise, defined as

$$\gamma_N = \frac{1}{1 + \text{SNR}^{-1}}$$

where SNR is the signal-to-noise ratio; and,  $\gamma_G$  is the decorrelation due to the size of the resolution cell and the local surface slope. The "penetration",  $\sigma_Z$ , which is a measure of the standard deviation of scatterers in the vertical direction, is defined as

$$\sigma_Z = \frac{2}{K_Z} \sqrt{1 - \gamma_Z}$$

- The height rms inside a window whose size is determined by the user.
- The slope rms inside a window whose size is determined by the user.
- The brightness rms inside a window whose size is determined by the user.
- The rms of the detrended slope.
- The rms of the detrended height.

In addition, **featureVector** calculates the surface slopes in the north and east directions.

• **bayesClass:** This module implements a standard Bayes classifier assuming Gaussian probability density functions and equal *a priori* probabilities. The inputs consist of the features calculated by **featureVector** and a file which contains the training information required by the Bayes Classifier. The philosophy behind this approach has been to decompose the true feature pdfs using Gaussian basis functions, and each basis function is treated as a separate class in the classification. For this version of the processor, a total of four land use classes have been chosen: water, trees, urban, non-treed/non-urban terrain. To go from the many (typically on the order of 20) classes used in the Bayes classification to these four classes, a projection method is used, as described below. Training was accomplished by using sites for which ground truth had been manually collected. The training set spanned a variety of sites including areas around the San Francisco Bay area, Crater Lake, Washington, and the Los Angeles County area.

• **collapseClass:** As discussed above, the number of classes generated by **bayesClass** is greater than the four classes ultimately used in the terrain classification layer. **collapseClass** uses a simple mapping to collapse the classification layer into four classes.

• **cleanClass:** This program uses contextual information to clean up the water layer in the classification. The information used includes surface slope and area covered by connected components.

• **sieve:** In general, the classification will have a greater resolution than is desired in the output map product. The **sieve** module decomposes the classification map into connected components and iteratively merges smaller ones into neighboring larger ones, until every component in the classification map has a minimum area. This procedure avoids the blockiness associated with simple averaging algorithms and preserves edges.

## Feature Calculation

The AUTOMAP processor currently implements only two automatically derived feature layers: the mountain/peak and drainage layers.

• **Mountain/Peak Layer:** This layer is generated by two programs, **mountain** and **peak**. **mountain** computes a mountain mask based on slope and covered area criteria. This mask, together with the elevation, is used by **peak** to find all the major mountain peaks contained inside the mountain mask.

- **Drainage Layer:** Due to its large memory requirements, the drainage layer is calculated at the map quad level, rather than for the strip map data. The drainage network is calculated by a module of the TOPAZ topography analysis package, version 1.10, produced by Martz and Garbrecht for the US Department of Agriculture. The complete TOPAZ package can measure topographic properties, define surface drainage, delimit watershed boundaries, quantify the drainage network, and parametrize subcatchments and overland flow paths, but we use only a small subset of its capabilities.

To obtain a drainage network, the DEDNM module first preprocesses the DEM to remove localized depressions by filling them in up to the lowest outflow point, and lowering the DEM levels of localized impoundments (dams) across drainage paths to allow the flow to continue. Flat regions either in the DEM or produced by depression fill-in are then modified by adding small height variations consistent with the surrounding terrain and just large enough to define a flow path across the regions. The D8 (deterministic eight-neighbor) method is used to calculate the steepest descent direction for each pixel. Then, starting at each DEM cell in turn, the flow vectors are followed from cell to cell until the edge of the DEM is encountered, and the upstream area value for each cell along the path is incremented. After all DEM cells have been used as starting points, the upstream area value for each cell is the number of DEM cells that drain into that cell. Finally, to define the drainage network, only cells that have an upstream area greater than a threshold value (the Critical Source Area, CSA) are marked, and paths shorter than a minimum length (Minimum Source Channel Length, MSCL) are pruned. The CSA and MSCL can be spatially varying to account for varying hydrologic controls, such as soil type or vegetation, but we use only a single value for these quantities for the drainage network calculation.

The DEDNM module has been slightly modified for the AUTOMAP purpose. The original program did not have an exit path after the drainage network was calculated, so one was added as an option. The DEM input routine was also modified to read a binary DEM file, and to accomodate data values less than 1m. Finally, the output is reported as a vector layer, rather than a byte image.

### Auxiliary Layers

In addition to the previous layers, AUTOMAP computes a series of useful auxiliary layers which may be incorporated in the GIS data bas and output map products:

- **Height Error Layer:** A layer containing the random DTE height error, as derived from the measured correlation function, is also calculated. The height error is calculated by first calculating the estimated phase noise,  $\sigma_\Phi$ , using the Cramer-Rao bound

$$\sigma_\Phi = \frac{1}{\sqrt{2N}} \frac{\sqrt{1 - \gamma^2}}{\gamma}$$

where N is the number of looks. The height error is then estimated using the formula

$$\sigma_h = \frac{\lambda \ r \ (\sin \theta + \cos \theta \tan \tau)}{2\pi B} \sigma_\Phi$$

where B is the component of the baseline perpendicular to the look direction,  $\theta$  is the local incidence angle, r is the range to the scatterer location,  $\tau$  is the surface slope in the azimuth direction, and  $\lambda$  is the wavelength.

- **Shaded Relief:** A shaded relief image is calculated from the slope layers. The brightness value is set by forming the dot product,  $\hat{\mathbf{n}} \cdot \hat{\mathbf{r}}$ , where  $\hat{\mathbf{n}}$  is the local surface normal, and  $\hat{\mathbf{r}}$  is the unit vector in the look direction.
- **Brightness Modulated Classification RGB Layers:** Red, green, and blue image planes are generated using the brightness to set the image value and the classification to set the image hue.
- **Sigma0 Layer:** The radiometrically corrected brightness feature is used as an auxiliary layer.
- **Penetration Layer:** The penetration feature is used as an auxiliary layer.

### Geolocation and GIS Database Generation

The geolocation is performed using nearest neighbor interpolation going from sensor coordinates to UTM. The GIS database generation is performed by using PCI, a commercially available GIS program. Given the user selected map size and location and a set of options, this module will resample the strip map layers generated in the previous module to a UTM map using the WGS 84 ellipsoid. It will, in addition, calculate a contour level vector layer. The output GIS data base will be stored in PCI format.

### Map Product Generation

The map product generation module is performed by using PCI hardcopy map making utilities to generate the map data product selected by the user. The output is in a standard graphic format which can be output by a color printer or viewed electronically.

## 3. SAMPLE RESULTS

Figure 3 presents a sample output of the AUTOMAP processor for data over the San Francisco Area. The training set for this classification was obtained by selecting small representative samples for each of the four classes from the data itself. In the image, Golden Gate Park and the Presidio region, which are known to be treed, are clearly recognizable. The urban areas agree with USGS 7.5' quads. The Bay and Pacific Ocean are also clearly identified. A detailed comparison against ground truth confirms many of the detailed features observed in the classification map, although there are areas, such as in the hills above Golden Gate Park where the extent of tree coverage is over-estimated. The contour lines shown in the map are obtained from the TOPSAR IFSAR derived DEM.

## 4. CONCLUSIONS

We have presented a description of the JPL AUTOMAP processor for generation of map products and auxiliary layers using C-band IFSAR data alone. Preliminary results indicate that the techniques presented here represent an automated alternative to traditional stereo photography for generating finished map products. Furthermore, the current processing speed of the AUTOMAP processor is 3 squared kilometers/per minute using a 16 processor Silicon Graphics Power Challenge. This efficiency is much greater than that which can be achieved using conventional optical techniques.

## **5. ACKNOWLEDGEMENTS**

The research described in this paper was carried out by the Jet Propulsion Laboratory, California Institute of Technology, under contract with the National Aeronautics and Space Administration.

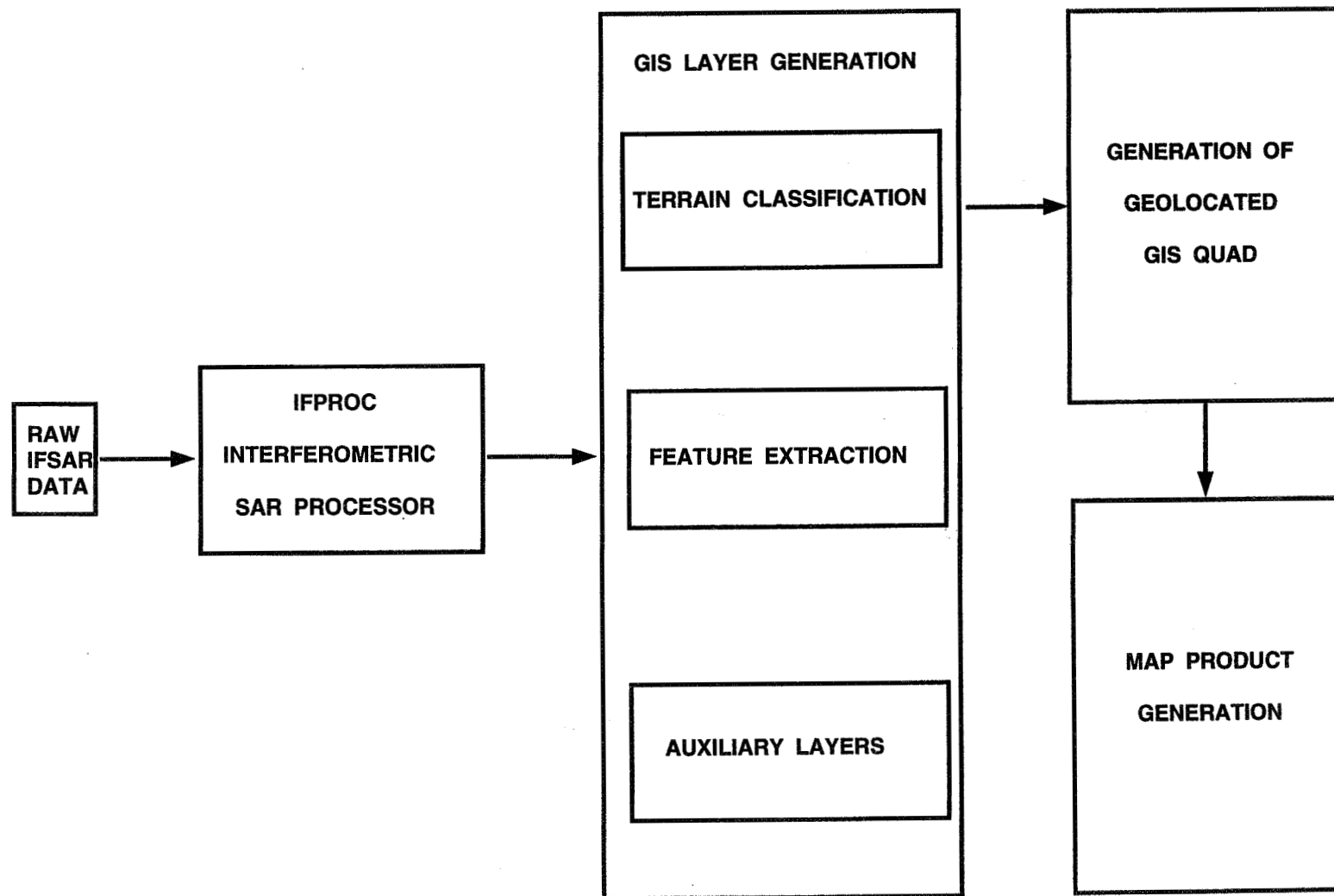


**Figure 1:** Flow diagram for the JPL AUTOMAP Processor



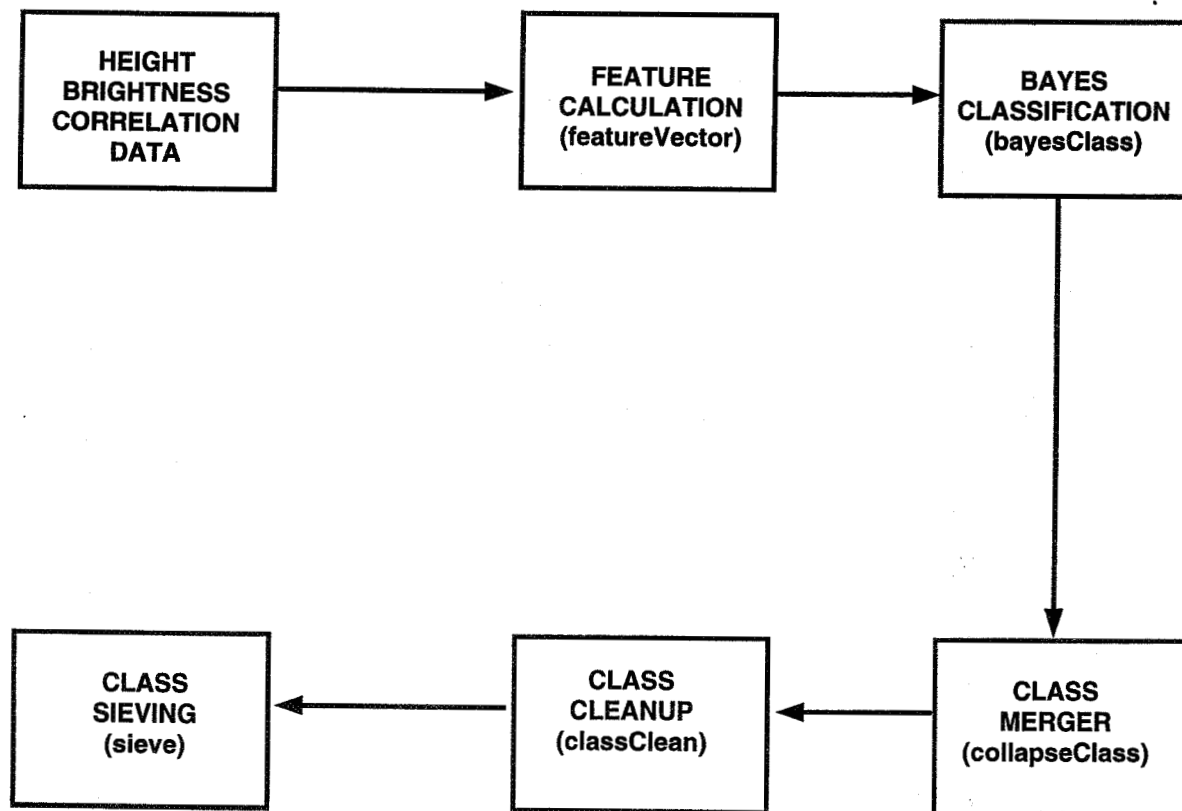
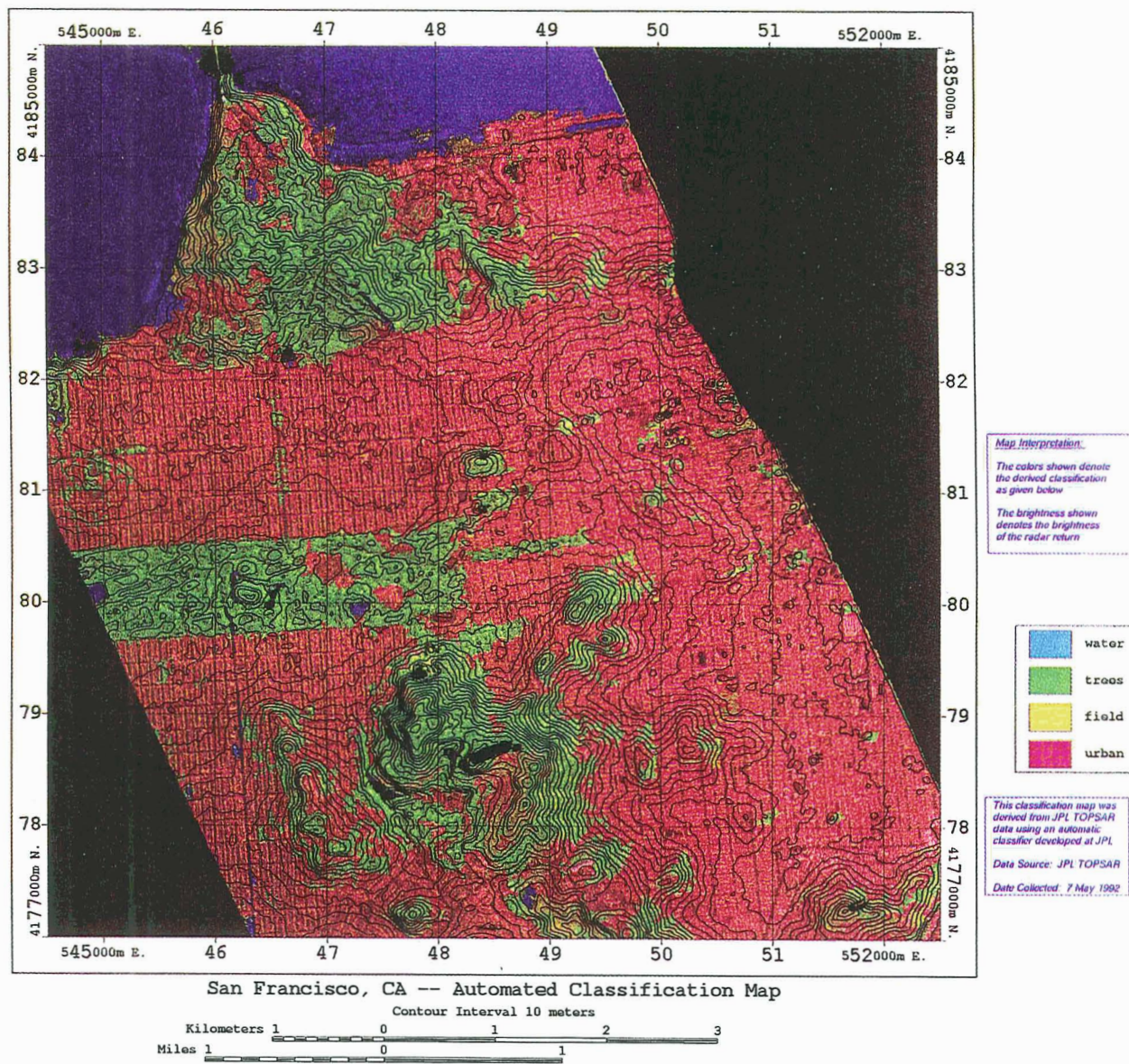


Figure 2: Flow diagram for the terrain classification module of the JPL AUTOMAP processor.

**Figure 3:** Sample product of the JPL automap processor showing IFSAR generated height contour levels, terrain classification (image hue), and radar brightness (image value) simultaneously.



**Page intentionally left blank**

# First Results of the TOPSAR C-Band / L-Band Interferometer: Calibration and Differential Penetration

Paul A. Rosen and Scott Hensley

Jet Propulsion Laboratory  
California Institute of Technology  
4800 Oak Grove Drive  
Pasadena, CA 91109

## SUMMARY

The NASA/JPL TOPSAR instrument recently was extended from a single-wavelength C-band (5.6 cm- $\lambda$ ) dual aperture synthetic aperture radar interferometer to include a second wavelength at L-band (24 cm). Adding the second wavelength invites comparison of wavelength-diverse effects in topographic mapping of surfaces, with the principal goal of understanding the penetration of the radar signals in vegetation canopies, and determining the inferred topographic height. A first analysis of these data was conducted at two sites. Elkhorn Slough near Monterey, California presented flat, vegetation free terrain required for calibrating the radar interferometric parameters. A second site stretching from San Jose to Santa Cruz, CA, which is heavily vegetated, provided the first test case for wavelength diverse penetration studies. Preliminary results show that: a) the interferometer calibration determined at Elkhorn Slough is extendable to Laurel Quad and gives confidence in the C- and L-band height measurements; b) Clear differences are observed between the C- and L-band heights associated with vegetation, with C-band-derived topographic heights generally higher than those from L-band. The noise level in the L-band interferometer is presently the limiting factor in penetration studies.

## Introduction

The NASA/JPL TOPSAR instrument, maintained and operated by the Jet Propulsion Laboratory AIRSAR group (Yunjin Kim, supervisor) was extended from a C-band-only topographic mapping SAR interferometer to L-band wavelengths (Howard Zebker, principal investigator) with the addition of a second L-band antenna complementing the AIRSAR polarimetry aperture. The radar instrumentation was modified to allow operation in the usual TOPSAR mode, in which a single antenna transmits the radar pulses and both antennas receive, or in ping-pong mode, where alternate antennas transmit on alternate pulses but both antennas receive on all pulses. In ping-pong mode, the effective separation between the antennas, called the baseline is increased by a factor of two relative to TOPSAR mode, giving increased sensitivity to topographic height. This is particularly important at L-band, where the short baseline relative to the wavelength causes considerable height noise despite good signal-to-noise conditions. Typical imaging geometries and height sensitivities for TOPSAR are summarized in Table 1.

The dual-wavelength, dual-baseline capability of the new TOPSAR system allows detailed study of the effects of vegetation canopies on the interferometrically derived heights. Coherent backscatter of microwave radiation is dominated by scatterers sized of the order of the radar wavelength.

It is well known from comparison of heights at field/forest stand boundaries in flat terrain that the C-band signal scattering in the forest is dominated by the canopy such that the interferometrically derived height is well above the forest base. The dual wavelength capability of the interferometer measures the differential penetration depth (if any) to provide insight into the scattering mechanism, which can be complicated in real canopies. The vegetation canopy increases the effective scattering area of each resolution cell, leading to increasingly decorrelated radar echoes as the interferometer baseline is increased. The dual baseline capability of the TOPSAR interferometer tests this prediction and establishes the usefulness of decorrelation measurements for estimating canopy depths.

This work takes the first steps toward addressing these fundamental questions by first calibrating the system at C- and L-band, then comparing C- and L-band height maps. Before the measurements can be interpreted, calibration is essential. The locations of the phase centers of the interferometer antennas are very difficult to measure at the millimeter scale required for accurate topographic mapping (Madsen et al 1993). Centimeter scale errors in baseline components can lead to planimetric and vertical map distortions in the tens of meters. In addition to the baseline, systematic phase errors exist in the radar data that are attributable to scattering of energy into an antenna from multiple paths, ostensibly the antenna farings. These systematic phase errors corrupt the derived height maps in the cross track direction with vertical and horizontal oscillations of several meters' amplitude at C-band and over 10 meters at L- band, severely limiting the utility of the measurements for sensitive differential penetration studies.

## Calibration

The C-band TOPSAR baseline is measured yearly to an accuracy of a few centimeters. Until recently inaccuracies in the aircraft attitude and position measurement system precluded meter scale accuracy mapping. With the operational use of a refined inertial navigation system in late 1994 and in 1995, a finer accuracy baseline for C-band is needed. Calibration using an array of corner reflectors in Rosamond dry lake bed is under way, however the flight conditions were turbulent and windy, so verifying the derived baseline parameters will require additional work. For the purposes of this study an alternate path of calibration was taken. It has the advantage of removing height distortions due to baseline errors and multipath phase errors simultaneously. This phase screen approach was first employed when JPL calibrated the Environmental Research Institute of Michigan's IFSARE X-band topographic mapper (Kim and Imel 1995).

The phase screen approach requires a reference digital elevation model. The TOPSAR digital terrain map is computed as an array of height values on a locally spherical grid. At the same time, the imaging geometry of each array element is recorded. The difference between the TOPSAR map and the reference DEM is taken - this constitutes an array of height errors. The residual interferometric phase error needed for calibration  $\Delta\Phi$  is related to these height errors  $\Delta h$  through the ambiguity height equation, given in a simplified two dimensional geometry by

$$\Delta\Phi(r) = \frac{2\pi n}{\lambda} \frac{B \cos(\theta - \alpha)}{r \sin(\theta)} \Delta h \quad (0.1)$$

where  $B$  is the baseline length,  $\alpha$  is the angle the baseline makes with the horizontal measured counterclockwise,  $\theta$  is the look angle,  $\lambda$  is the wavelength, and  $n$  is 1 for TOPSAR mode or 2 for ping-pong mode. The height-induced errors from both multipath and baseline error are primarily

functions of the look angle, so the phase screen correction inferred from the difference DEM and the geometry is tabulated as a function of look angle. By using the entire two dimensional DEM, the one dimensional phase screen benefits from averaging and is quite smooth despite errors in the DEM data. Using this phase screen to correct the interferogram, a new TOPSAR digital terrain map is produced and compared to the reference DEM. An adjusted phase screen is then computed and compared to the first estimate. This procedure is iterated until the phase screen becomes stable, usually after no more than two iterations.

Figure 1 illustrates the phase distortions in the radar heights in the left-most panel. The area is located at Elkhorn Slough, CA and is quite flat, containing a large part of Monterey Bay in the left of the image. Despite the flat terrain, there is a tilt of the heights from left to right (near range to far range) in the image as well as oscillatory banding aligned with the flight direction, the effects of baseline error and multipath. The center panel shows the difference between the radar heights and the USGS 90m DEM resampled to the radar coordinates at 30 m spacing. The USGS DEM is the best readily available digital data set for this site. Nearly all the terrain features remaining in the difference map are due to inaccuracies or resolution limits in the USGS data. Nevertheless, the net phase screen derived from the difference map is quite smooth.

On the second iteration, the region of the difference map used was restricted to the ocean and featureless areas in the bottom half of the image. This improved the estimate considerably. The right most panel of Fig. 1 shows the calibrated height data. The ripples in the Bay and flat regions clearly evident in the left panel have been removed in the right panel. If we assume that the average height of the USGS map over wide areas is correct, we can conclude that the phase screen calibration performed well. Figure 2 shows the phase screen profile as a function of look angle.

The L-band system is new, so the baseline is commensurately less well known than the C-band baseline. To calibrate L-band, we decided to estimate its baseline by comparing the interferometric phase at C-band to the phase at L-band. If both baselines are perfectly well known then the following relationship holds:

$$\Phi_L(r) - \frac{\lambda_C}{\lambda_L} \frac{B_L \cos(\theta(r) - \alpha_L)}{B_C \cos(\theta(r) - \alpha_C)} \Phi_C(r) = 0 \quad (0.2)$$

Any residual phase  $d\Phi(r)$  remaining as a function of range  $r$  we attribute at this stage to baseline error through the relation

$$\frac{\lambda}{2\pi n} d\Phi(r) = dB \sin(\theta - \alpha) - d\alpha B \cos(\theta - \alpha) \quad (0.3)$$

It is straightforward to derive the corrections  $dB$  and  $d\alpha$  from the residuals  $d\Phi$ . The L-band baseline given in Table 2 was determined in this way. As a cross check of the baseline estimate, we measured planimetric distortion of the data before and after baseline correction by correlating the L-band interferogram with the C-band data. Before baseline correction, the images were misregistered by many pixels particularly in the near range. After baseline correction, the images aligned to within a pixel everywhere.

The phase screen correction for L-band is still necessary because of multipath. Instead of using the USGS DEM, we used the newly calibrated C-band DEM. Few large scale artifacts exist in the difference map, however the large amount of height noise in the L-band data due to large ambiguity height limited the effectiveness of the phase screen. Residual multipath ripples remain in the L-band DEM at the 1-2 meter amplitude level. Though this is considerably lower than the statistical height noise at L-band, the artifacts are visible to the eye.



## Preliminary penetration results

Two differential penetration maps have been produced. The first is located at Elkhorn Slough, an obvious choice for calibration because the surface is essentially unvegetated. Figure 3 shows the calibrated C-band (left panel), L- band (center) and the C-L height difference (right panel). We expect the right panel to have no topographic variation even in areas of high relief, and this is observed: The L-band calibration succeeded, and the statistical height error of 2 – 5 m is sufficiently low to allow detection of penetration differences.

Figure 4 shows the same three panels for a different site, Laurel Quad, CA located between San Jose and Santa Cruz. Laurel Quad is heavily vegetated with tall conifers and deciduous trees, as well as populated with grasslands and clear-cuts. Penetration differences should be apparent in the C-L difference map as positive numbers because penetration is expected to be larger at L- band. Indeed, close examination of the right panel shows virtually no height differences in the urban areas to the north and south but statistically significant differences in the forested areas between. Note that the imaging geometry and acquisition time for the C- and L-band systems are identical so there can be no terrain bias effect or angular calibration error causing this difference. Furthermore, careful study of the figure, or inspection of the full resolution data (these data are averaged for display), shows a clear correlation between backscatter variations associated with canopy and the height differences. In particular, above the image center southeast of San Jose, the northern slopes show clear vegetation, while the southern slopes are bare and show no vegetation.

Transects through the urban areas and forest consisting of profiles averaged across many image lines show clear distinctions, with an average difference of zero in the city and 4-6 meters in the forest. It is not clear how representative the average transect height is of the actual penetration locally. The image shows patchiness that is often attributable to variations in canopy. Because of the large height error in the L band data however, considerable averaging is required. Therefore, to better characterize the penetration, uniform tree stands must be identified from ortho images and other ground truth and a statistical average computed, probably as a single number per stand. This detailed analysis is under way. Comparison of these data with other acquisition modes will also provide insights into penetration phenomenology. However, calibration of the remaining modes is just beginning.

## References

1. Kim, Y. and D. Imel (1995) IFSARE Phase Calibration Report. JPL Interoffice Memorandum 3349-95-017 (Internal document), Jet Propulsion Laboratory, Pasadena, Calif.
2. Madsen S.N., H. A. Zebker, and J. M. Martin (1993). Topographic mapping using radar interferometry: processing techniques. *IEEE Trans. Geosci. Rem. Sens.*, **31**, 246-256.

## Acknowledgment

The research described in this paper was carried out by the Jet Propulsion Laboratory, California Institute of Technology, under a contract with the National Aeronautics and Space Administration.

TABLE 1  
RELEVANT INTERFEROMETRIC MAPPING MODES AND PARAMETERS<sup>†</sup>

Map Product posting (m)	5	
Map Product Resolution (m)	15	
Range Bandwidth (MHz)	40	
Range Resolution (m)	3.331	
Pulse Repetition Ground Spacing (m)	0.34	
Number of Looks	30	
Aircraft Altitude (km)	8	
Range (km)	9	17.5
Look Angle (deg)	25	63
C/L-Band Ambiguity Height (m)	56/243	174/755
C/L-Band Nominal Interferometric Correlation	0.90/0.94	0.90/0.94
C/L-Band Nominal Statistical Height Error (m)	0.56/1.81	1.73/5.63

<sup>†</sup> For 40 MHz ping-pong mode

TABLE 2  
PRELIMINARY TOPSAR INTERFEROMETRIC CALIBRATION PARAMETERS

Wavelength	L-Band (24 cm)			C-band (5.6 cm)		
Antenna Location	Top	Bottom	T-B <sup>a</sup>	Top	Bottom	T-B
X <sup>†</sup> (m)	0.54	0.54	0	2.46	2.46	0
Y (m)	1.231	0.52	0.711	1.154	0.157	0.997
Z (m)	1.601	-0.23	1.831	1.577	-0.717	2.294
$\Delta\phi_d$ (rad) <sup>††</sup>	0.85	0	0.85	0	-1.35	1.35
$\Delta t_d$ (ns)	428.02	444.72	-16.7	406.08	437.04	-30.96

<sup>a</sup> T-B implies baseline components

<sup>†</sup> X coordinate measured forward along aircraft fuselage

Y coordinate measured outward to port side

Z coordinate measured vertically upward

<sup>††</sup> Channel phase  $\Delta\phi_d$  and time delay  $\Delta t_c$  are mode dependent.

These values are valid for 40 Mhz ping pong mode only.



**Page intentionally left blank**

# TOPSAR "PHASE SCREEN" CALIBRATION

Elkhorn Slough, CA Run 180-1 1995

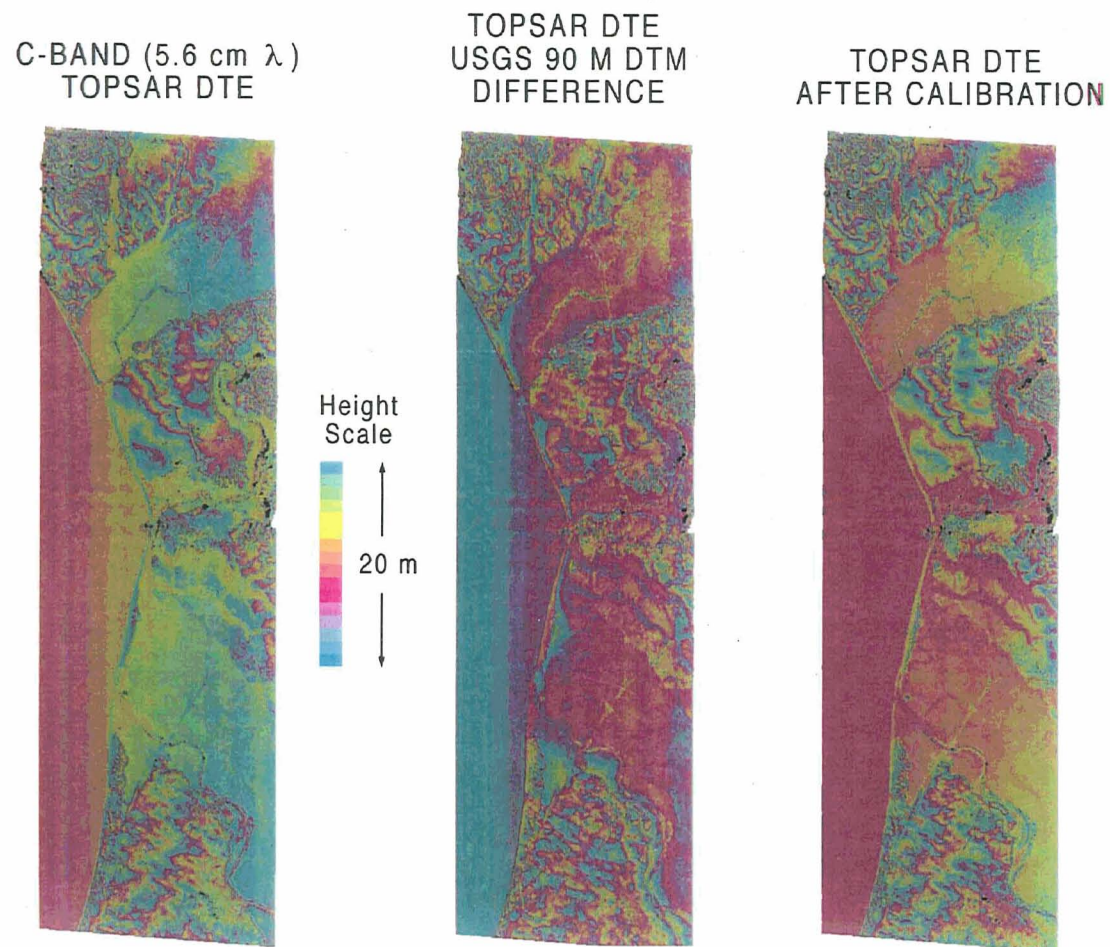


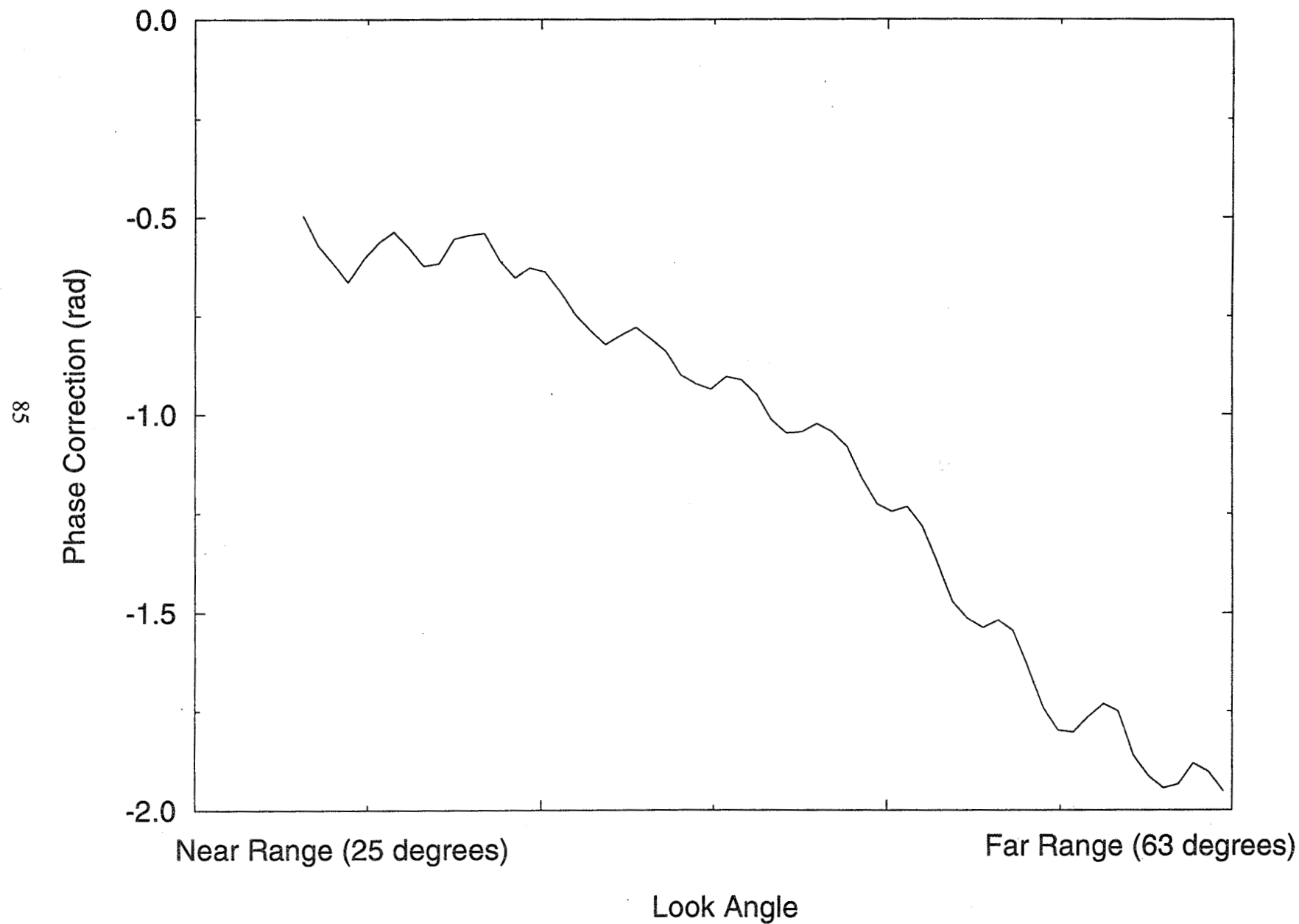
Figure 1

**Page intentionally left blank**

# Phase Screen Calibration

C-Band Phase Correction Vector

FIGURE 2



**Page intentionally left blank**

# TOPSAR DUAL FREQUENCY TOPOGRAPHIC MAPPING Elkhorn Slough, CA Run 180-1 1995

C-BAND (5.6 cm  $\lambda$ )

L-BAND (24 cm  $\lambda$ )

C-L TOPOGRAPHY

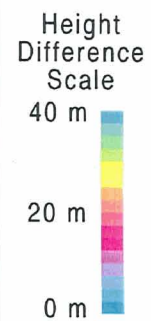
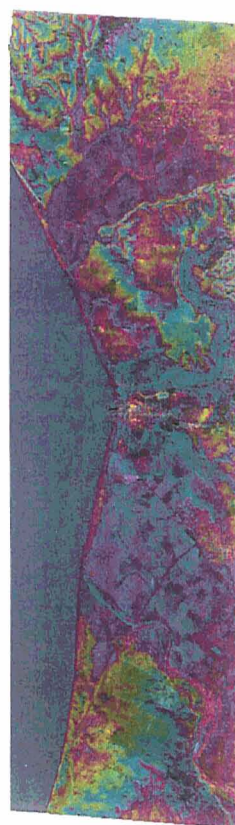
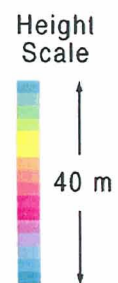
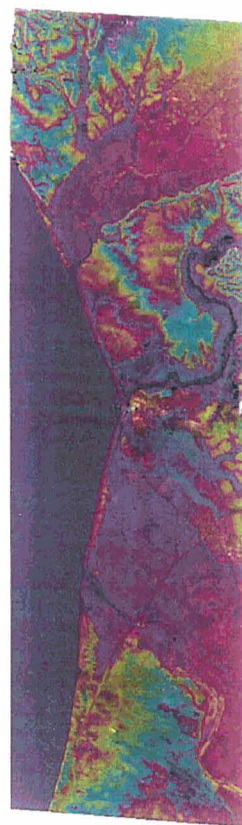


Figure 3

**Page intentionally left blank**



# TOPSAR DUAL FREQUENCY TOPOGRAPHIC MAPPING

Laurel Quad, CA, Run 180-3 1995

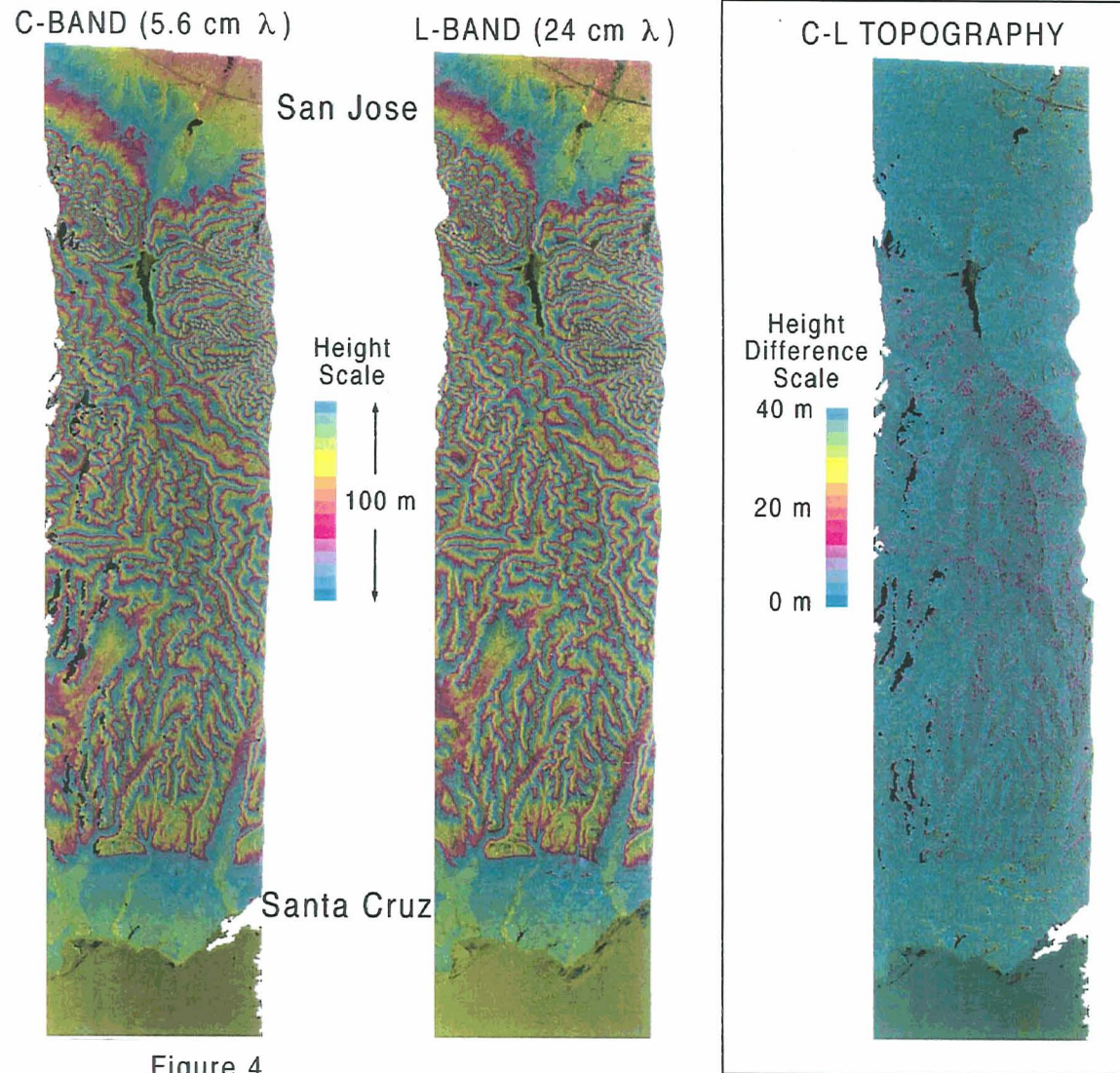


Figure 4



**Page intentionally left blank**

## **MEASUREMENTS OF OCEAN FEATURES WITH AIRSAR**

**\*David Sheres and \*\*Walt Osterman**

**\*Center for Marine Science \*\*Scientific Computing Dept.**

**University of S. Mississippi**

**Stennis Space Center, MS 39529**

**\*email dsheres@radar.ucsd.edu**

### **ABSTRACT**

Oceanographers have tried to obtain ocean data from SAR since mid 1978 when SEASAT was launched and exposed an impressive array of features on the ocean surface. The difficulty in obtaining quantitative ocean data from SAR imagery is due to the fact that different ocean/atmosphere processes modulate the grey shades in the imagery. It is difficult to tell whether a front observed in the imagery is due to changes in the air/sea temperature difference, wind variability, horizontal current shear, rain front or spawning of near surface organisms. Determination of quantitative values, for the shear for example, are not realistic. With this gloomy introduction in mind, how do we proceed?

Here we will discuss an indirect approach for measuring ocean features from SAR imagery. The approach is based on the refraction of swell that can be seen in the SAR imagery. Locally, swell refraction is due only to changes in bathymetry and surface current shear and it is easy to separate these two effects. Utilizing the indirect approach requires the following steps:

1. Image segmentation to a size smaller than the velocity scale.
2. Dominant waves enhancement in each segment.
3. Determination of the wave number of the dominant waves in each segment.
4. An inverse model utilizing the refraction of the dominant waves.

It has been shown already that linear energetic shears can be detected and measured from high resolution images of the ocean (see for example Sheres et al *JGR*, May 1985). A simple approach to measuring surface velocity and shear is to divide the imagery to smaller segments where the shear in each segment is approximately linear (not curved); the known linear algorithm would then be applied to each segment; the velocity /shear distribution can then be determined by assembling the segments with linear shear into an estimate of the actual shear/velocity distribution.

Swell is many times buried in the noise of SAR imagery. To use the swell in the SAR imagery as a diagnostic tool to measure shear/currents, we frequently need to enhance the dominant waves in the SAR imagery. An example of dominant wave enhancement using AIRSAR imagery will be presented. The imagery was obtained in May 26, 1993 over a coastal area in the Gulf of Mexico exhibiting a rich array of features.

# Estimation of Local Incident Angles for Bare surface Using only SAR Measurements and Its Applications

Jiancheng Shi and J. Dozier\*

Institute for Computational Earth System Science (ICESS)

\*School of Environmental Science and Management

University of California, Santa Barbara, CA 93106

Telephone: (805) 893-2309

FAX: (805) 893-2578

## ABSTRACT

The effects of terrain geometry result a great problem in SAR data calibration and interpretation of the relationships between geophysical parameters and radar backscattering measurements. The terrain correction could be done if we can determine the sensor position accurately and if high resolution and accurate Digital Elevation Model (DEM) is available at study site. It is clear that the radar backscattering highly depends on the local incidence angle. In this study, we have developed a model for the bare surface based on the simulations of Integral Equation Model (IEM) for a wide range of surface dielectric and roughness conditions. This model characterizes the relationship between the backscattering coefficients of VV and HH polarizations at L-band and the incidence angle. The model does not require the surface dielectric and roughness information so that it is possible to determine local incidence angle for each pixel with only SAR measurements. We tested this model with NASA/JPL AIRSAR over Washita. The results showed an accuracy within a few degree can be achieved over the bare surface. However, the vegetated surface has significant effect on this relationship.

An example of applications of this model is to estimate snow density. The imaginary part of dielectric constant of ice is very small so that the microwave is transparent over snow cover. The penetration depth could reach several ten meters. Since snow is a dense media, with density ranges from 0.1 to 0.55 in general, the real part of dielectric constant of snow is dependent only on the snow density. Our evaluation has shown the backscattering measurements at L-band over dry snow covered terrain are mainly affected by:

1. Incidence angle change: from incidence angle at air/snow interface to refractive angle at snow/ground interface.
2. The wavenumber (or wave propagation constant) will be shifted from  $k_0$  to  $k_0\sqrt{\epsilon_s}$ .
3. The dielectric contrast will be changed from  $\frac{\epsilon_g}{\epsilon_0}$  to  $\frac{\epsilon_g}{\epsilon_s}$ .
4. The transmission loss at the air/snow interface.

Where subscript g, s, and 0 represent ground, snow, and air, respectively. With consideration of above factors, we can determine the refractive angle at snow/ground interface by using the model that we have developed. Furthermore, the snow density estimation can be obtained for each pixel by comparing the local incidence angle (at air/snow interface) calculated using DEM and the estimated refractive angle from L-band SAR measurements. We will demonstrate this technique and validations in detail.

**Page intentionally left blank**

## MODELING WETLAND VEGETATION USING POLARIMETRIC SAR

K. Clint Slatton(\*), Melba M. Crawford(\*), James C. Gibeaut(\*\*), Roberto O. Gutierrez(\*\*)

(\*): Center for Space Research, University of Texas at Austin  
2901 N. IH-35, suite 300, Austin, TX 78722

(\*\*): Bureau of Economic Geology, University of Texas at Austin  
E-mail: slatton@poseidon.csr.utexas.edu  
Ph: (512) 471-5506 Fax: (512) 471-3570

### 1.0 Introduction

Sandy barrier islands dominate the Atlantic and Gulf of Mexico shorelines of the United States. These islands naturally erode and accrete in response to waves, wind, tides, and long-term sea-level change. Since the late 1800s, barrier island shorelines on the whole have eroded at an average rate of 0.8 m/yr, although in many areas the rate can be several meters per year (Gibeaut and Crawford, 1994). The barrier island and peninsula complex off the coast of Texas is composed of several interactive depositional subenvironments. Tidal inlets (semipermanent breaches in the island) commonly open, close, and migrate along the coast with significant changes occurring over time scales of several months to decades. Storms can lower the beach and dunes by as much as 3 m while simultaneously depositing as much as a meter of washover sand in the backbarrier areas. They can also move shorelines tens of meters landward and create channels, scarps, and dune blowouts with a topographic relief of several meters. Post-storm recovery of the dune system, however, can take several years. During fair-weather conditions, the elevation and horizontal position of the beach changes daily from 1 cm to 1 m, depending on wave and wind conditions. Currently it is impossible to rapidly and accurately measure these changes across entire barrier islands or in various subenvironments.

Galveston Island and Bolivar Peninsula reach a maximum elevation of 3 - 5 m above sea level (White et al., 1985). Because of their extremely low relief, even slight changes in the surface topography can result in significant variations in the soil and vegetation. Detailed knowledge of the topography can improve predictions for sediment erosion/accretion processes, storm impact and recovery, and the capability to map coastal wetland environments. Coastal geological studies have primarily focused either on long-term studies of large-scale phenomena at coarse spatial resolutions or on high-resolution, short-term studies of small-scale phenomena. Long-term studies are useful in describing general coastal change caused by cumulative effects of coastal processes. Short-term studies measure fine-scale changes in beaches and dunes occurring over periods ranging from one wave cycle to one monthly tidal cycle or during a single storm. They do not accurately show the integrated response of coastal depositional systems across a large area. To understand the dynamics of barrier islands, the interactions between various subenvironments and adjacent islands must be considered. A means to rapidly collect accurate high-resolution topographic data across tens of kilometers of shoreline has not existed, however. NASA/JPL's fully-polarimetric multi-frequency AIRSAR system has the potential to collect these data (using TOPSAR mode or repeat-pass interferometry techniques). When these topographic data are combined with wave, current, wind, and sediment data, a better understanding of the overall response of the coast to various environmental conditions will be possible. This understanding will in turn allow formulation of better predictive models of shoreline erosion.

A three-year project to study small-scale topographic changes and relict geomorphic features on barrier islands using synthetic aperture radar (SAR) is underway at the University of Texas at Austin as part of a NASA program to study global topographic change. A study area on

the Texas coast consisting of Galveston Island and Bolivar Peninsula was overflowed by the NASA/JPL DC-8 AIRSAR in April, 1995. Data was acquired in the fully polarimetric mode using C-, L-, and P-bands and in the TOPSAR configuration with C- and L-bands in interferometric mode. The study area will be overflowed again in late spring of 1996. The data will be registered to GPS-surveyed points to form high-resolution digital elevation models (DEMs), and then analyzed to investigate possible topographic changes.

Initially, the fully polarimetric data from a test site on Bolivar Peninsula is being used to model the SAR backscatter coefficient ( $\sigma^0$ ) response to wetland vegetation. Marshes that commonly form the landward shorelines of barrier islands generally accrete and erode more slowly, but are often subject to rapid natural or man-induced changes. In the Galveston Bay area, about 20% of coastal marshes were lost from the 1950s to 1989. Draining, filling, and man-induced submergence caused by fluid withdrawal (water and oil) were responsible for most of the loss (Gibeaut and Crawford, 1994). By modeling the backscatter from the vegetation in the various sub environments, the study will investigate the use of SAR for studying wetland environments (Durden et al., 1995), (Ott et al., 1990). The vegetation species in this low-relief area are very sensitive to slight changes in the surface elevation. Using both GPS measurements and the TOPSAR data, the relationship between the vegetation and the topography will be investigated.

## 2.0 Background

Mathematical models have been developed that relate SAR backscatter measurements to surface parameters such as soil moisture (Oh et al., 1992), (Shi et al., 1992), (Dubois et al., 1995) and to vegetation parameters like woody biomass and branching structure (Dobson et al., 1992), (Durden et al., 1989). However, most of the previous research in these two areas has been devoted to the study of soil properties for bare to sparsely-vegetated terrain and vegetation properties for agricultural crops and forested areas. Studies have also demonstrated the capability to distinguish between wetland sub environments using SAR, (Hess et al., 1995) and (Pope et al., 1994), and more recently, the ability of vegetation models to explain the observed backscatter from herbaceous vegetation in the presence of surface water (Durden et al., 1995). Many of the models developed to represent the  $\sigma^0$  response to natural terrain either describe scattering from a surface or scattering from vegetation above the surface. Each class of model relates the observed  $\sigma^0$  to parameters that characterize the geometric and electrical properties of the study area. Once a mathematical relationship has been developed, parameters of interest are computed via model inversion.

Surface models such as (Shi et al., 1992) and (Dubois et al., 1995) attempt to represent the different polarization combinations of  $\sigma^0$ , and their linear combinations, as functions of the angle of incidence, geometric properties ( e.g. rms surface height), and electrical properties ( e.g. relative dielectric constant ). Because of the large difference in electrical conductivity between water and dry soil, the relative dielectric constant can be used to estimate the soil moisture using dielectric mixing models (Dobson et al., 1985). The mathematical expressions relating  $\sigma^0$  to these parameters are either based upon electromagnetic theory or empirically derived (Chen and Fung, 1995). Theoretical models such as the small perturbation method and the phase perturbation method are useful for investigating the dependence of  $\sigma^0$  on various parameters, but are only valid for surfaces that are very smooth relative to the incident wavelength (Oh et al., 1992). Most natural surfaces exceed this limit on surface roughness. Although the integral equation method, which may apply to a greater variety of surfaces, has been recently developed (Fung et al., 1992), researchers have historically utilized empirical surface models to explain  $\sigma^0$  behavior over natural terrain.

Empirically-based models can better deal with the levels of surface roughness encountered in natural terrain, but they suffer from two major shortcomings: (1) a strong dependence upon the data used to develop them, and (2) difficulty in separating the effects of surface roughness from those of soil moisture. Once a backscatter model has been developed by empirically fitting a function to a particular data set, it usually does a poor job of predicting  $\sigma^\circ$  for other data sets (Dubois et al., 1995). Although this problem can be alleviated by using several data sets to develop the model, it will still perform poorly if the terrain being analyzed differs significantly from that used to develop the model. The second shortcoming of the empirical surface models is their difficulty in separating the contributions of surface roughness and dielectric constant relative to the total  $\sigma^\circ$  in the presence of significant vegetation. The primary effect of the vegetation layer covering the surface is to introduce a volume-scattering component into  $\sigma^\circ$ . This produces the same response that an increase in either surface roughness or the relative dielectric constant (decrease in soil moisture) would cause, so the change in  $\sigma^\circ$  cannot be uniquely attributed to either effect. As a result, these models tend to overestimate surface roughness and underestimate soil moisture when vegetation is present.

The impact of vegetation cover on the predictive capability of a model varies substantially. Researchers have investigated various approaches to reduce the sensitivity of the models to vegetation cover. Ratios of the co-polarized  $\sigma^\circ$  responses and their linear combinations have been considered (Dubois et al., 1995) as well as accounting for the volume scattering and surface scattering components of  $\sigma^\circ$  separately (Shi et al., 1992). These approaches often achieve improved representation of the measurements, but the problem has not been completely solved, so models should only be applied to appropriate data. The Dubois et al. (1995) model includes a criterion for determining whether the vegetation cover is too thick for the model to provide adequate results. Areas where this criterion is exceeded are excluded from consideration. The  $\sigma^\circ_{\text{hv}}/\sigma^\circ_{\text{vv}}$  ratio is used as an indicator of significant vegetation since the amount of diffuse (multiple) scattering usually increases in the presence of vegetation. A threshold of -11 dB at L-band was determined empirically for this particular model. Applying this criterion to the Bolivar Peninsula test site excluded approximately 85% of the terrain. Because this class of models is not directly applicable to the data acquired of the Bolivar test site, and appropriate generalizations are not apparent, models of the scattering due to vegetation are being investigated instead. These models will be used for discriminating vegetation in the test site and representing the behavior of  $\sigma^\circ$  in the presence of marsh vegetation.

Vegetation models have been used to represent the plant material both as a layer of continuous and discrete random media (Lang, 1981). Several techniques for analyzing the scattering from continuous random media were developed in the 1960s and 1970s. These models assume that the permittivity of the medium is a random variable whose statistical moments are known, and then determine the average backscatter cross section from the layer. More recently, the plant material has been treated as a layer of randomly-oriented discrete scattering elements. This approach allows a more direct representation of various plant elements (e.g. trunks and size, shape, and orientation of leaves and branches). These plant elements are often described by dielectric cylinders and disks with random orientations prescribed by probability distribution functions (Yueh et al., 1992). Much of the research with discrete vegetation models has focused on agricultural crops and forested areas (Brakke et al., 1981) and (Durden et al., 1989). Recently, these types of models have also been applied to grasslands and wetlands (Saatchi et al., 1994) and (Durden et al., 1995). In particular, Durden et al. (1995) focused on flooded herbaceous vegetation similar to some areas of the Bolivar Peninsula test site.

These vegetation models can also be considered to be empirically-based in that model coefficients and characteristics of the scattering elements can be varied to achieve a better fit to the observed  $\sigma^\circ$ . Insight can also be gained into the scattering behavior of the vegetation by varying



the orientation, size, and shape of the scattering elements. Some of these models can also be used to determine what fractions of the total  $\sigma^0$  are due to various scattering mechanisms, including direct scattering from the vegetation and direct-reflected scattering from ground/vegetation interaction (Lang and Sidhu, 1983). The model from (Durden et al., 1995) expressed the attenuation coefficient and scattering cross-section per unit volume in terms of the leaf area index (LAI). It was then possible to estimate LAI, which can be a useful parameter for assessing plant growth stage and density.

### 3.0 Site Description and Data Collection

The initial test site selected for developing the wetland-vegetation model is a saltwater marsh on the landward side of Bolivar Peninsula, TX (Fig. 1). A single fully polarimetric, three frequency frame from the AIRSAR coverage over the Bolivar Island test site is being analyzed initially (Fig. 2). The site contains a variety of terrain types and associated vegetation. The upland flats of the peninsula consist mostly of herbaceous range grasses. Towards the mainland, the terrain gradually decreases in elevation and supports a saltmarsh. Between the uplands and saltmarsh lies a highly saline intertidal zone where salt flats and salt barrens form. The saltmarsh can be further segmented into lower and upper marshes which correspond to frequently flooded and non-flooded areas. The elevation ranges from sea level at the edge of the saltmarsh to about 2 m on the upland flats, with the highest point occurring along the foredunes at approximately 4 m.

The vegetation in this test site is strongly dependent upon the elevation. The saltmarsh becomes less frequently flooded further from the landward side of the peninsula and the tidal inlets. The intertidal zone develops at the maximum elevation where flooding and soil moisture are still due to seawater. Here, the salt compounds are precipitated out of the water through evaporation, creating a highly saline environment. Finally, on the upland flats, the elevation is sufficient to prevent the frequent flooding. Each of the regions can be distinguished by the most commonly occurring vegetation and, to a lesser extent, the soil type. For developing the vegetation models, the test site is considered to be comprised of upland flats, an intertidal zone, non-flooded saltmarsh, and flooded saltmarsh. The upland flats, near the center of the peninsula, are characterized by loose, sandy soil. The water table is often close to the surface, but the topsoil is still typically well-drained and dry. This region is covered with range grasses such as *Evagrostis* (Webb), which tend to be short (8-10 cm) and have blades oriented between 45° and 90°. The salt barrens and flats of the intertidal zone also have sandy soil, but are more saline. This region supports only sparse vegetation such as the short grasses *monathochloe littoralis*, and succulents such as *Salicornia* (Webb) and (White and Paine, 1992). The *monathochloe littoralis* has very short leaves (5-10 mm) which occur along the ground runners. The *Salicornia* grows erect to heights of 6 cm. The high, less-frequently flooded saltmarsh occurs just below the intertidal zone. Marsh soils have a higher concentration of silt and organic material than the upland terrain. The high marsh is dominated by tall grasses called *spartina patens*, which grow to 90 cm and are vertically oriented. The lower saltmarshes are very often submerged under several centimeters of standing water. The dominant species is a very tall grass (150 cm) known as *spartina altiniflora*.

As expected, preliminary visual interpretation of the image showed that C-band is the best frequency for differentiating vegetation differences. The longer wavelength L- and P-bands penetrated the vegetation and revealed large scale surface variation which is in rough agreement with the soil variation on the peninsula. The sandy soils of current and past beach ridges produced stronger  $\sigma^0$  responses than the silty soils that comprise the existing marsh over which the beach ridges have accreted. Field measurements will be used to determine whether the radar is actually penetrating the vegetation and sensing soil differences or merely indicative of variation in the vegetation that itself is responding to soil differences.

Combinations of various polarizations were employed as simple indicators of the relative abundance of vegetation. The difference between the P-band co-polarized data ( $\sigma_{hh}^{\circ} - \sigma_{vv}^{\circ}$ ) was examined because it was expected that the vegetation would attenuate  $\sigma_{vv}^{\circ}$  more than  $\sigma_{hh}^{\circ}$ , especially at longer wavelengths. The response was relatively weak throughout the intertidal zone, which agreed with the sparse vegetation in that region. Ratios of cross-polarized values of  $\sigma^{\circ}$  were also investigated. The L-band ratio  $\sigma_{hv}^{\circ}/\sigma_{vv}^{\circ}$  was expected to indicate the presence of depolarization caused by multiple scattering from very rough surfaces and vegetation, with a reduced dependence upon local slope and incidence angle. The response was weak in the intertidal zone and very strong in the uplands, with an intermediate level of response over the marsh. The intertidal zone produced the weakest response because of the sparse vegetation. The relatively weak response over the marsh is believed to be due to the specular nature of the standing water and extremely smooth surface in that region.

#### 4.0 Analysis & Future Work

Ground measurements will be acquired from these four regions to support the development of the vegetation models. Surface parameters such as rms surface roughness, volumetric soil moisture, and saline concentration will be measured. Dielectric mixing models will be used to then estimate soil dielectric constant. (Dobson et al., 1985). Plant geometry and moisture content will also be measured. Average plant height, size, shape of the leaves, and leaf and stalk orientation will represent the size and orientation of the scattering elements in the models (Lang, 1981). Plant moisture content will be used to estimate vegetation dielectric constants (El-Rayes and Ulaby, 1987). Adjustment will be made for differences in plant geometry due to annual growth which has occurred since the SAR data was acquired. Model results will be compared to the  $\sigma^{\circ}$  data from an AIRSAR frame centered over the test site. Adequate geometric correction of the AIRSAR frame will be achieved using extensive GPS data and GPS-surveyed corner reflectors visible in the image.

The structural form of the model developed by (Lang and Sidhu, 1983) is being used initially. Vegetation is treated as a layer containing scattering elements over a flat lossy ground, or a specular reflector if flooded (Durden et al., 1995). The herbaceous vegetation, which mostly consists of grass stalks and blades of varying height and orientation, is modeled as a layer of dielectric disks with specified orientation distributions. The dielectric constant of the ground is being adjusted to account for the moisture and salinity variations observed in the field measurements. The model uses the Foldy technique to determine an approximate equation for the mean field. Using this mean field, an equivalent dielectric constant for the scattering layer is determined. The correlation of the field is then determined by assuming that the scatterers are imbedded in the equivalent medium (i.e. the distorted Born approximation). The model results are being compared to the SAR data to investigate differences in the predictions of the  $\sigma^{\circ}$  values for the various subenvironments.

The configuration of the scattering elements will be investigated to best approximate the true plant geometry. Other wetland sites in the study area will also be analyzed to test the range of applicability of the model. Finally, the correspondence between vegetation type and topography will be examined.

## 5.0 References

- Brakke, T. W., E. T. Kanemasu, J. L. Steiner, F. T. Ulaby, and E. Wilson, 1981, "Microwave Radar Response to Canopy Moisture, Leaf Area Index, and Dry Weight of Wheat, Corn, and Sorghum," *Remote Sensing of Environment*, vol. 11, pp. 207-220.
- Chen, K. S., A. K. Fung, January 1995, "A Comparison of Backscattering Models for Rough Surfaces," *IEEE Trans. Geosci. Remote Sensing*, vol. 33, no. 1, pp. 195-200.
- Dobson, M. C., F. T. Ulaby, M. T. Hallikainen, and M. A. El-Rayes, January 1985, "Microwave Dielectric Behavior of Wet Soil - Part II: Dielectric Mixing Models," *IEEE Trans. Geosci. Remote Sensing*, vol. GE-23, no. 1, pp. 35-46.
- Dobson, M. C., F. T. Ulaby, T. Le Toan, A. Beaudoin, and E. S. Kasischke, 1992, "Dependence of Radar Backscatter on Coniferous Forest Biomass," *IEEE Trans. Geosci. Remote Sensing*, vol. 30, no. 1, pp. 412-415.
- Dubois, P. C., J. J. van Zyl, and T. Engman, July 1995, "Measuring Soil Moisture with Imaging Radars," *IEEE Trans. Geosci. Remote Sensing*, vol. 33, no. 4, pp. 915-926.
- Durden, S. L., J. J. van Zyl, and Howard Zebker, May 1989, "Modeling and Observation of the Radar Polarization Signature of Forested Areas," *IEEE Trans. Geosci. Remote Sensing*, vol. 27, no. 3, pp. 290-301.
- Durden, S. L., L. A. Morrissey, and G. P. Livingston, May 1995, "Microwave Backscatter and Attenuation Dependence on Leaf Area Index for Flooded Rice Fields," *IEEE Trans. Geosci. Remote Sensing*, vol. 33, no. 3, pp. 807-810.
- El-Rayes, M. A. and F. T. Ulaby, September 1987, "Microwave Dielectric Spectrum of Vegetation - Part I: Experimental Observations," *IEEE Trans. Geosci. Remote Sensing*, vol. GE-25, no. 5, pp. 541-549.
- Fung, A. K., Z. Li, and K. S. Chen, 1992, "Backscattering From a Randomly Rough Dielectric Surface," *IEEE Trans. Geosci. Remote Sensing*, vol. 30, pp. 356-369.
- Gibeaut, J. C. and M. M. Crawford, July 1994, "Detecting Small-Scale Topographic Changes and Relict Geomorphic Features on Barrier Islands Using SAR," University of Texas proposal, pp. 1-18.
- Hess, L. L., J. M. Melack, S. Filoso, and Y. Wong, July 1995, "Delineation of Inundated Area and Vegetation Along the Amazon Floodplain with the SIR-C Synthetic Aperture Radar," *IEEE Trans. Geosci. Remote Sensing*, vol. 33, no. 4, pp. 896-904.
- Lang, R. H., January 1981, "Electromagnetic Backscattering From a Sparse Distribution of Lossy Dielectric Scatterers," *Radio Science*, vol. 16, no. 1, pp. 15-30.
- Lang, R. H. and J. S. Sidhu, January 1983, "Electromagnetic Backscattering From a Layer of Vegetation: A Discrete Approach," *IEEE Trans. Geosci. Remote Sensing*, vol. GE-21, no. 1, pp. 62-71.

- Oh, Y., K. Sarabandi, and F. T. Ulaby, March 1992, "An Empirical Model and an Inversion Technique for Radar Scattering from Bare Soil Surfaces," *IEEE Trans. Geosci. Remote Sensing*, vol. 30, no. 2, pp. 370-381.
- Ott, J. S., E. S. Kasischke, N. H. French, M. F. Gross, and V. Klemis, 1990, "Evaluation of Multichannel SAR Data for Analysis of a Mid-Atlantic Coastal Wetland Ecosystem," Proc. IGARSS'90, pp. 453-456.
- Pope, K. O., J. M. Reybenayas, and J. F. Paris, 1994, "Radar Remote Sensing of Forest and Wetland Ecosystems in the Central American Tropics," *Remote Sensing Environ.*, vol. 48, pp. 205-219.
- Saatchi, S. S., D. M. Le Vine, and R. H. Lang, January 1994, "Microwave Backscattering and Emission Model for Grass Canopies," *IEEE Trans. Geosci. Remote Sensing*, vol. 32, no. 1, pp. 177-186.
- Shi, J., J. J. van Zyl, J. V. Soares, and E. T. Engman, 1992, "Development of Soil Moisture Retrieval Algorithm for L-band SAR Measurements," Proc. IGARSS'92, pp. 495-497.
- Webb, J. W., *Saltmarsh Plants of the Gulf Coast*, non-published Texas A&M at Galveston document, pp. 8, 10.
- Webb, J. W., *Typical Dune Vegetation of the Upper Texas Coast*, non-published Texas A&M at Galveston document, pp. iii, 3.
- White, W. A., J. G. Paine, 1992, *Wetland Plant Communities, Galveston Bay System*, Bureau of Economic Geology: University of Texas at Austin, pp. 10.
- White, W. A., T. R. Calnan, R. A. Morton, R. S. Kimble, T. G. Littleton, J. H. McGowen, H. S. Nance, and K. E. Schmedes, 1985, "*Submerged Lands of Texas, Galveston-Houston Area: Sediments, Geochemistry, Benthic Macroinvertebrates, and Associated Wetlands*," Bureau of Economic Geology: University of Texas at Austin, Plate I.
- Yueh, S. H., J. A. Kong, J. K. Jao, R. T. Shin, and T. L. Toan, March 1992, "Branching Model for Vegetation," *IEEE Trans. Geosci. Remote Sensing*, vol. 30, no. 2, pp. 390-402.

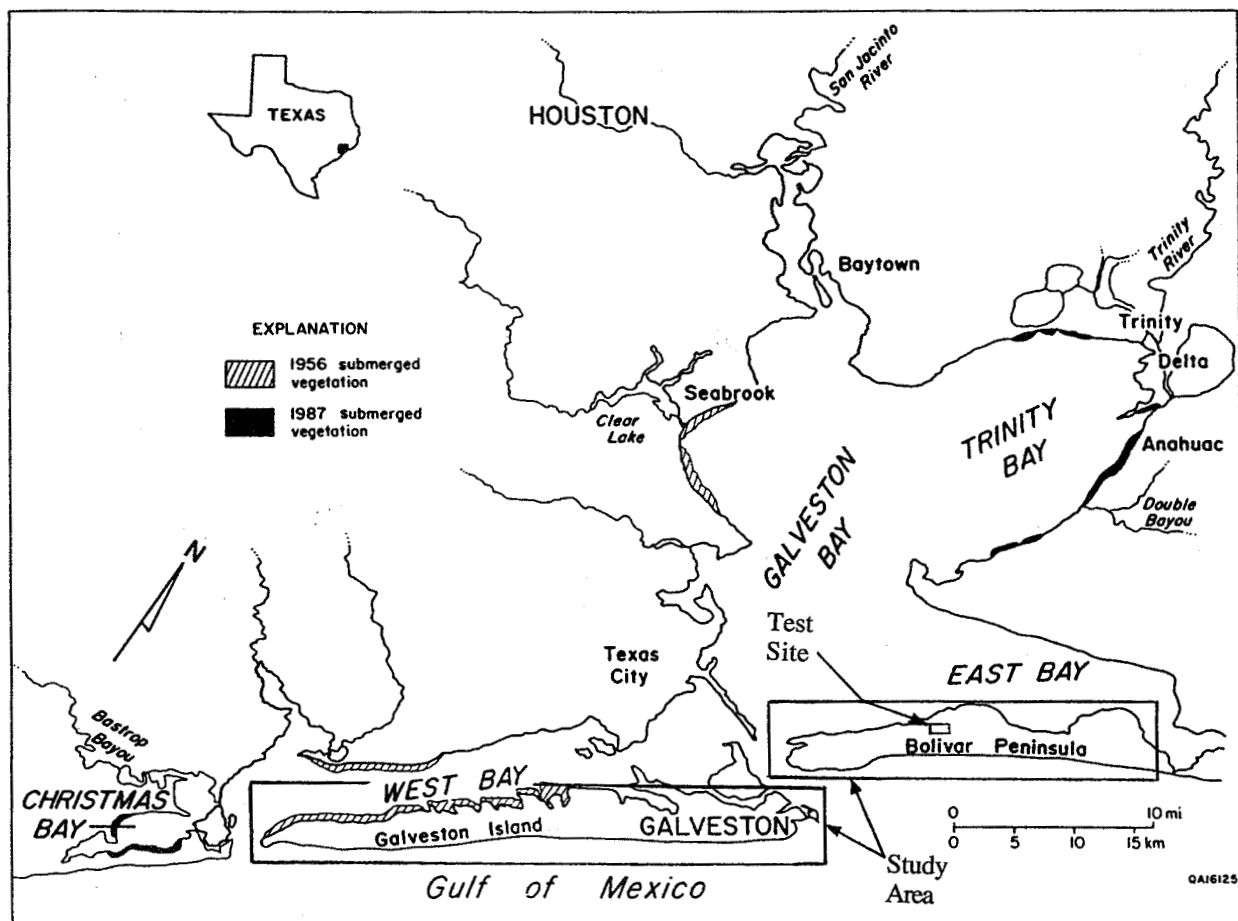


Figure 1 Study area (adapted from White et al., 1992 Fig. 28)

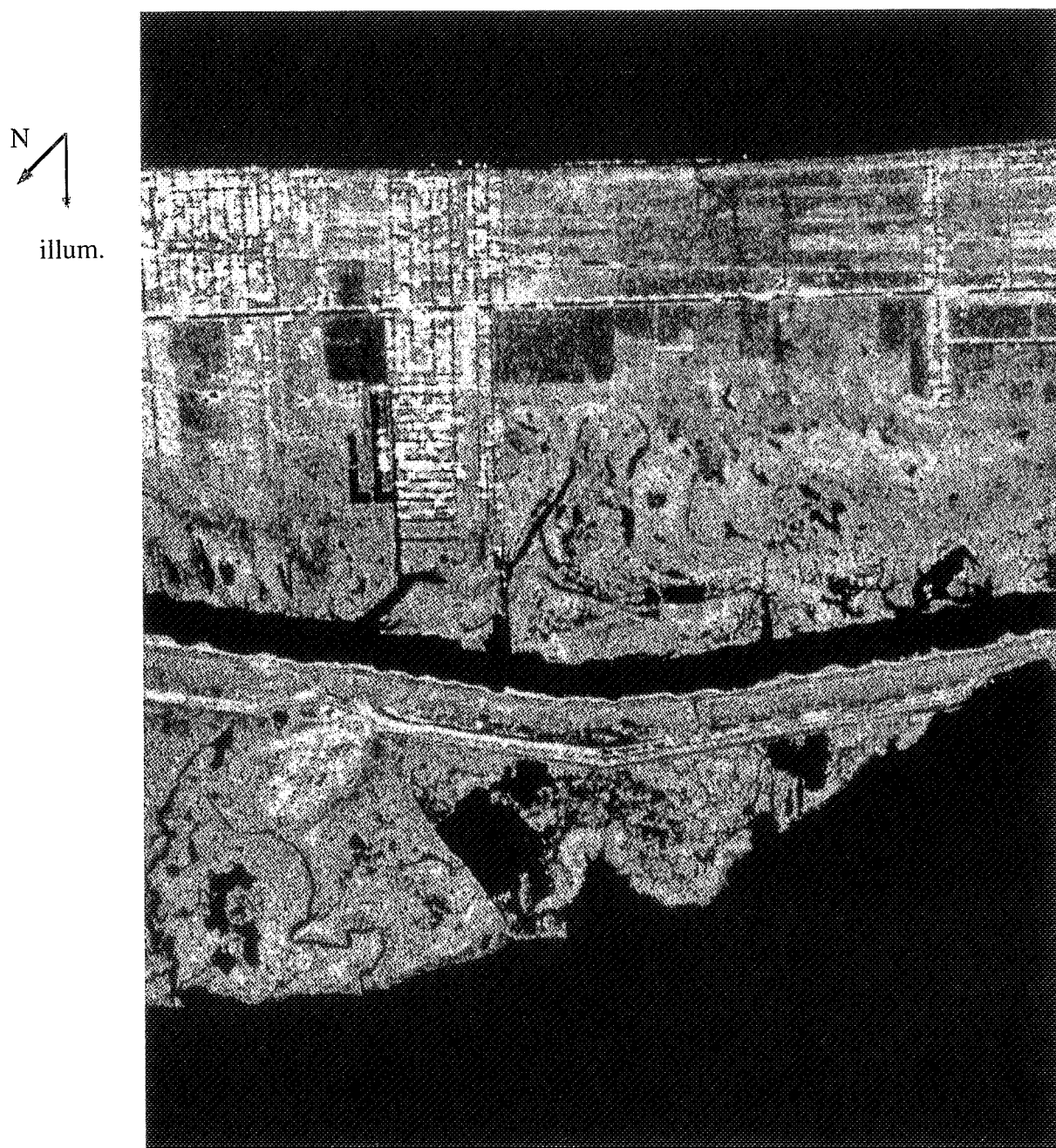


Figure 2 Test site ( C-band total-power image acquired by the NASA/JPL AIRSAR)

**Page intentionally left blank**

## **AIRSAR data for geological and geomorphological mapping in the Great Sandy Desert and Pilbara regions of Western Australia**

Ian J. Tapley  
CSIRO Division of Exploration and Mining  
Wembley, Western Australia 6014  
Phone: +619 387-0263  
Email: i.tapley@per.dem.csiro.au

Enhancements of AIRSAR data have demonstrated the benefits of radar for revealing an additional and much higher level of information about the composition of the terrain than enhancements of either SPOT-PAN or Landsat TM data. With the help of appropriate image-processing technology, surface and near-surface geological structures, hydrological systems (both current and ancient) and landform features, critical to the comprehension of adjacent mineralisation but often obscured by vegetation and unconsolidated materials, have been put plainly in evidence in a diverse range of landscapes.

In the Great Sandy Desert region where spectral variability is minimal (as observed by Landsat TM), radar's sensitivity to the micromorphology of sparse exposures of subcrop and lag gravels has provided a new insight into the region's geological framework, its landforms and their evolution that is unobtainable through conventional methods. Subtle variations in surface roughness of terrain components at scales near the observing wavelengths is the dominant factor contributing to the radar backscatter from the landscape components. Since most of the GSD is masked by a layer of sand and vegetation, and that much of the rock exposure is intermittent, localised and scattered, the unique ability of enhancements of AIRSAR data to highlight new details of this arid landscape is striking when compared to the published geological map and the SPOT-PAN and Landsat TM scenes of the region.

In the Pilbara region, advanced processing of AIRSAR data to unmix the backscatter between and within the three frequencies of data has highlighted sub-surface extensions of greenstone lithologies below sand cover and morphological evidence of past flow conditions under former climate regimes. The identification of palaeolandforms, subtle hidden geological structures, sequences of valley-fill sediments, regolith-landforms and sequences of landform development have all been achieved from enhancements of AIRSAR data.

On the basis of these observations which are described fully in restricted CSIRO-AMIRA reports, it is recommended that radar remote sensing technology involving the use of high resolution, polarimetric data be seriously considered as a viable tool for exploration in erosional and depositional environments located within Australia's mineral and oil-prospective provinces.



**Page intentionally left blank**

## **Improved regolith-landform and geological mapping using AIRSAR data as an aid to mineral exploration in the north-eastern goldfields region, Western Australia**

Ian J. Tapley  
CSIRO Division of Exploration and Mining  
Wembley, Western Australia 6014  
Phone: +619 387-0263  
Email: i.tapley@per.dem.csiro.au

In an exploration program it is important to understand the regolith-landform relationships so as to allow appropriate geochemical sampling methods to be chosen, to permit sampling programs to be optimised and to permit sensible data presentation and interpretation. This presentation discusses the distinctive contribution AIRSAR data can make in characterising the regolith-landforms in a relatively vegetation-free environment

AIRSAR frame-processed data were initially MAF-cleaned to enhance the signal content of the data before geocoding to AMG coordinates. Colours in a three frequency, single polarization combination image CVV/LVV/PVV, and in an enhancement of pedestal height, relate directly to the scale of surface roughness of the various regolith units. Consequently, the AIRSAR images were able to provide excellent discrimination between and within regolith-landform units mapped in a previous study using air photos and Landsat TM data.

Examination of the AIRSAR enhancements reveals that in mafic terrains, and to a lesser extent, in felsic terrains, AIRSAR data provides discrimination between the principal geomorphic regimes, relict, erosional and depositional. An important observation is the ability to consistently interpret the level of stripping of the landscape within the erosional regime from which details of regolith stratigraphy can be inferred. The multi-frequency signals respond differently to the relative abundance and texture of the surficial materials including soil, lag gravels and outcrop, for each unit within the weathering profile. Whilst the C-band response is similar (high) for all units, L- and P-band signals vary significantly from low to high according to the presence and texture of the surface float and outcrop.

A multivariate statistical technique called an all-possible subsets calculation was used to examine the degree of polarimetric separation between selected regolith-landforms for all combinations of the nine-band AIRSAR data. This process uses, as a statistical base, the pixel values of training sites representing the regolith-landforms which are important for the polarimetric separation of the regolith-landform classes. In this study, the process indicated the most significant 3-band subset(s) suitable for enhancing the polarimetric contrast between regolith-landforms on an image processing screen or in a hardcopy image.

An unanticipated aspect of the research has been the identification on the AIRSAR imagery of previously unmapped, structural features. These same features cannot be identified in air photos or other remotely sensed datasets. Their mapping has led to the development of a hypothesis for describing the structural control and development of landforms within this region.

The requirement for a regolith-landform framework and knowledge of the processes of landscape evolution is integral to the planning, execution and interpreting of geochemical sampling programs. Of necessity this entails the recognition and characterisation of regolith units and regolith stratigraphy, and the ability to distinguish between relict, erosional and depositional materials.

**Page intentionally left blank**

## PERFORMANCE OF POLARIMETRIC PROCESSING TECHNIQUES USING NAWC P-3 SAR IMAGERY

J.G. Teti, Jr.\*, R. R.-Y. Lee, J.S. Verdi, and W.-M. Boerner\*\*

\*Lambda Science, Inc.  
P.O. Box 238  
Wayne, PA 19087-0238, USA  
T/F +(1) (215) 957-5354/5494

Naval Air Warfare Center  
Aircraft Division  
Warminster, PA 18974-0591, USA  
T/F +(1) (215) 441-1422/7281

\*\*University of Illinois at Chicago, EECS  
Communications, Sensing & Navigation Lab, M/C-154  
Chicago, IL 60607-7018, USA  
T&F: +1(1) (312) 996-5480

*Abstract*—SAR polarimetric processing has received a great deal of attention for the purposes of enhancing the detection, classification and/or identification of scene scattering features. This paper describes and compares the results obtained from applying the polarimetric processing techniques that have been developed and/or advanced by researchers at MIT Lincoln Laboratory, and basic polarimetric matched filter (PMF) techniques that have been modified to treat distributed scatterers. The paper describes the individual polarimetric processing techniques and the formulations used for their application to polarimetric imagery obtained from the NAWC P-3 SAR. For all cases the polarimetric techniques have been applied to enhance the detection of distributed scatterers in clutter. The motivation for the emphasis arises from considering most complex scatterers of interest (either man-made or natural) as distributed scatterers consisting of multiple scattering centers, and many modern polarimetric radar systems have the resolution performance to resolve the multiple scattering centers. Furthermore, the individual scattering centers of a distributed target can often exhibit different polarimetric scattering characteristics, and consequently do not respond favorably to polarimetric processing techniques that have been derived for individual point scatterers. The treatment of distributed scatterers also includes concepts for tuning the polarimetric ensemble response of individual scattering centers.

**Page intentionally left blank**

# **The Information Content of Interferometric Synthetic Aperture Radar: Vegetation and Underlying Surface Topography**

Robert N. Treuhaft

Jet Propulsion Laboratory, California Institute of Technology  
Pasadena, California 91109  
Telephone: 818-354-6216  
e-mail: bob\_treuhaft@radar-email.jpl.nasa.gov

## **1. Introduction**

While interferometric synthetic aperture radar (INSAR) was primarily developed as a technique for measuring surface topography [Graham, 1974], it is also very sensitive to the vertical structure of vegetation. Parameters describing the vertical distribution of vegetation, the simplest of which is the depth of the vegetation, are of interest for vegetation monitoring and ecological successional modeling. For example, vegetation layer depth and scattering characteristics can be used to infer biomass and age of forest stands [Manning et al. 1984]. Unlike single-aperture synthetic aperture radar (SAR), INSAR is sensitive to the distribution of the altitudes of the returns from a vegetation layer. The altitude distribution of returns depends on both the actual physical vertical distribution of vegetation in the layer, as well as the attenuation level of the radar signal at different depths in the layer. INSAR is therefore primarily sensitive to the physical structure of vegetation layers; it is affected by the chemical structure only through the degree to which attenuation, mainly due to water content, weights the returns from different depths into the vegetation. Because of its dominant sensitivity to physical structure, INSAR is potentially complementary to infrared and optical remote sensing techniques which are primarily sensitive to chemical composition [e.g. Wessman et al. 1988], but can also be used to infer structural changes in vegetation layers [e.g. Vogelmann et al. 1989]. Because radar penetrates the vegetation, INSAR is also sensitive to the surface topography underlying vegetation layers, which is important for hydrology and the study of lateral vegetation distributions.

Drawing from recently submitted work [Treuhaft et al., 1995], this paper first gives a heuristic description of the sensitivity of INSAR to vertical vegetation distributions and underlying surface topography. A parameter estimation scenario is then described in which the INSAR cross-correlation amplitude and phase are the observations from which vegetation and surface topographic parameters are estimated. It is shown that, even in the homogeneous-layer model of the vegetation, the number of parameters needed to describe the vegetation and underlying topography exceeds the number of INSAR observations for single-baseline, single-frequency, single-incidence-angle, single-polarization INSAR. Using ancillary ground-truth data to compensate for the underdetermination of the parameters, forest depths are estimated from the INSAR data. A recently-analyzed multibaseline data set is also discussed and the potential for stand-alone INSAR parameter estimation is assessed. The potential of combining the information content of INSAR with that of infrared/optical remote sensing data is briefly discussed.

## 2. Modeling the INSAR Response to Vegetation Vertical Distributions and Underlying Surface Topography

INSAR consists of transmitting a radio signal from one or both of two antennas and receiving the signal scattered from the surface and/or vegetation at both antennas. The antennas are located at either end of a baseline  $\vec{B}$ , as shown in Figure 1. The Figure shows a horizontal baseline and horizontal ground surface for simplicity, with radar incidence angle  $\theta_0$ . The two receivers and (at least) one transmitter can either be mounted on an aircraft, as in TOPSAR [Zebker et al., 1992], or on dual spacecraft, as in proposed orbiting interferometric missions. The vegetation is pictured as starting at the ground surface altitude of  $z_0$  and extending up to  $z_0 + h_v$ , where  $h_v$  will be called the vegetation layer depth. Returns from the lower edge of the vegetation at  $\vec{R}_0$  and from a vegetation constituent at  $\vec{R}_j$  are shown.

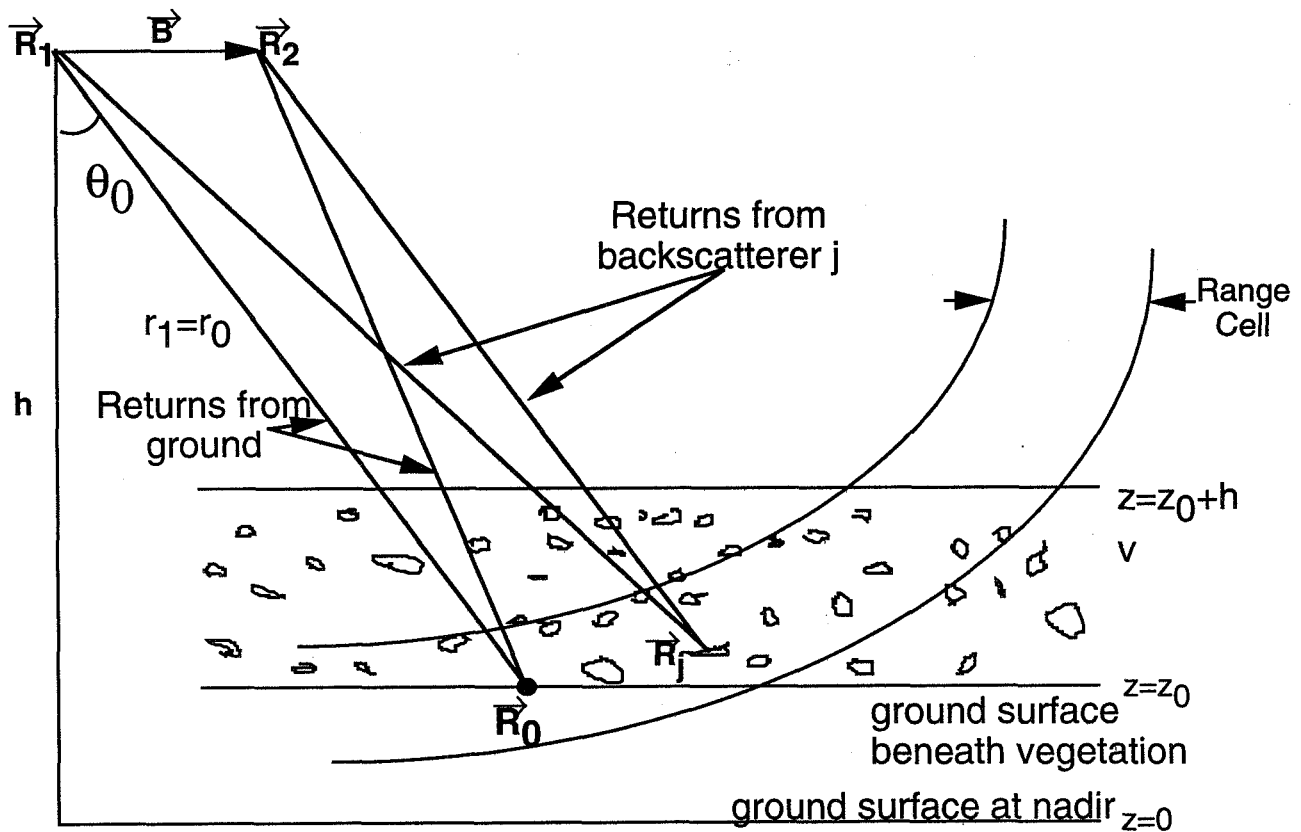


Figure 1: INSAR returns from the vegetation and ground surface.

The fundamental INSAR observations are the amplitude and phase of the complex cross-correlation of the signals from the 1 and 2 ends of the baseline. As shown in Figure 2, the qualitative effect of vegetation on the magnitude of the cross-correlation is to reduce it relative to that induced by bare surfaces. This is because each scatterer at  $\vec{R}_j$  with altitude

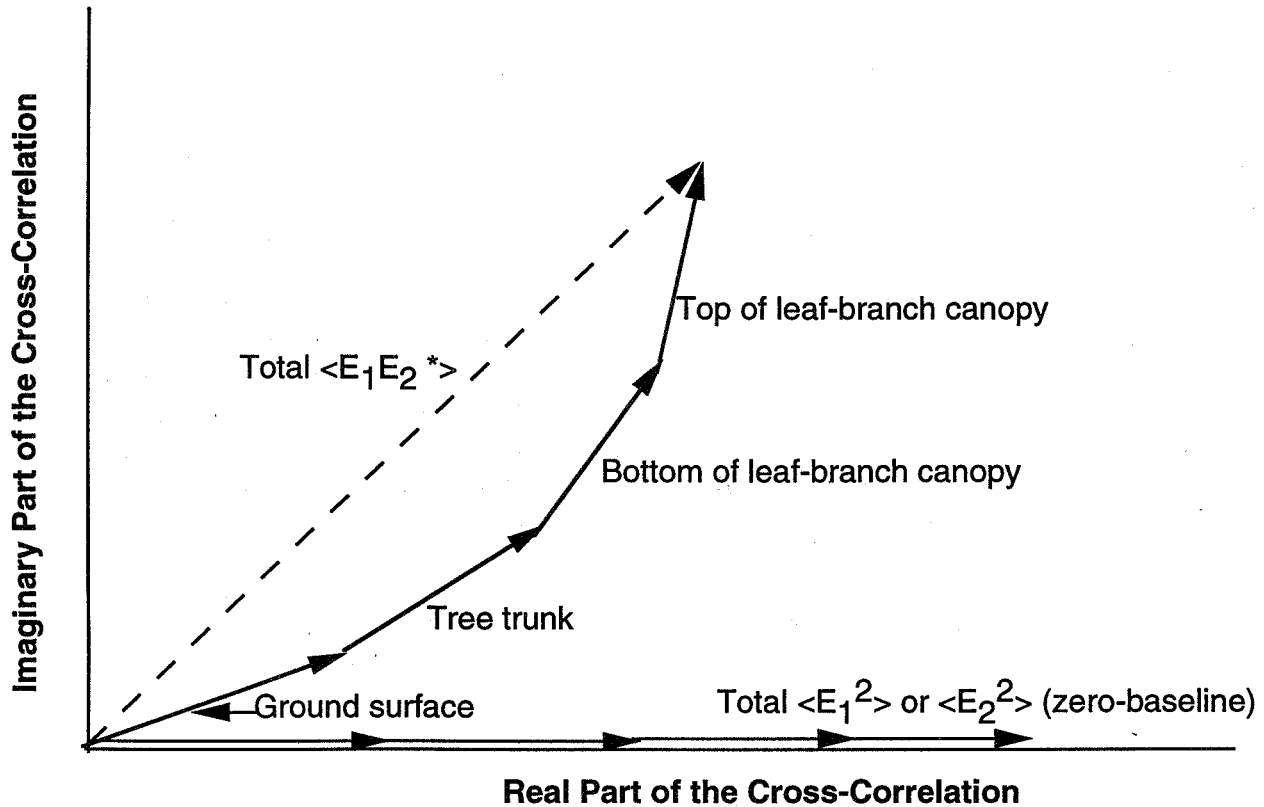


Figure 2: The schematic effect of vegetation at various altitudes on the real and imaginary parts of the INSAR cross-correlation function.

$z_j$  contributes a phasor to the cross correlation proportional to  $\exp(i\phi(z_j, r_{1j}))$  where

$$\phi(z_j, r_{1j}) \equiv k_0(r_{1j} - r_{2j})|_0 \approx k_0 B \sin [\cos^{-1} \left( \frac{h - z_j}{r_{1j}} \right)] \quad (1)$$

where  $k_0$  is the wave number at the center of the bandpass,  $h$  is the altitude of the radar, and  $r_{1j}$  is the range from the 1 end of the baseline to the scatterer  $j$  and similarly for  $r_{2j}$ . The incoherent addition of the phasors at different altitudes will cause the aggregate cross-correlation to be of smaller amplitude than the zero-baseline case, shown along the abscissa in Figure 2. The qualitative effect on the phase, due to the addition of cross-correlation phasors, is to increase it to some value between that observed for bare surfaces and that observed for a surface at the top of the vegetation layer. Expressions for the complex cross-correlation are derived in Treuhaft et al., 1995, on which most of this discussion is based. The expression for the INSAR cross-correlation in the presence of a vegetation layer with



vertical structure is given in an appendix in that reference. It is:

$$\begin{aligned} \langle E(\vec{R}_1)E^*(\vec{R}_2) \rangle &= A^4 e^{ik_0(r_1-r_2)|_0} \int_0^{2\pi} W_\eta^2(\eta-\eta_0) d\eta \int_{-\infty}^{\infty} W_r^2(2r'_1) r_0 e^{i\alpha_r r'_1} dr'_1 \\ &\times \int_0^{h_v} dz' e^{i\alpha_z z'} \rho(z') \langle f_b^2(z') \rangle \exp \left[ \frac{-8\pi}{k_0 \cos \theta_0} \int_{z'}^{h_v} \rho(z'') \text{Im} \langle f_f(z'') \rangle dz'' \right] \end{aligned} \quad (2)$$

where  $A$  is the 1/distance loss due to spherical wave propagation,  $k_0$  is the wave number of the radiation at the center of the bandpass,  $(r_1 - r_2)|_0$  is the difference in path length, between the two ends of the baseline, for signals originating from the point  $\vec{R}_0$  in Figure 1. In (2),  $W_\eta$  is an instrumental azimuthal resolution function, with azimuthal coordinate  $\eta$  (in and out of the paper in Figure 1),  $W_r$  is an instrumental range resolution function,  $r_0$  is the distance from the transmitter 1 to the point  $\vec{R}_0$  in Figure 1,  $\alpha_r$  is the derivative of interferometric phase with respect to the range direction, and  $\alpha_z$  is the derivative of interferometric phase with respect to the vertical  $z$  direction. Both  $\alpha_r$  and  $\alpha_z$  depend on the baseline length  $B$ , the incidence angle, and the frequency of radiation. The vegetation backward scattering amplitude  $f_b$ , the forward scattering amplitude  $f_f$ , and the vegetation density  $\rho$  are all described as functions of altitude. The integral inside the square brackets at the end of (2) describes the attenuation in the medium. The phase in the argument of the first exponential is that typically associated with bare-surface INSAR and is given by

$$\phi_0 \equiv \phi(z_0, r_0) = k_0(r_1 - r_2)|_0 \approx k_0 B \sin \left[ \cos^{-1} \left( \frac{h - z_0}{r_0} \right) \right] \quad (3)$$

where  $z_0$  is the altitude of the underlying ground surface. The ensemble average brackets in (2)  $\langle \cdot \rangle$  represent averages over different configurations of scatterers and different scatterer compositions and orientations. From (2), it can be inferred that although INSAR is sensitive to the vertical distributions in vegetation density and scattering amplitudes (which depend on both scatterer geometry and chemistry), the amplitude and phase of the cross-correlation  $\langle E(\vec{R}_1)E^*(\vec{R}_2) \rangle$  alone are not enough to invert (2) for  $\langle f_b^2(z) \rangle$ ,  $\rho(z)$ , and  $\text{Im} \langle f_f(z) \rangle$ .

### 3. Parameter Estimation Scenarios and Demonstrations

Ultimately, INSAR data from many baselines and frequencies could be used to invert (2) for detailed vertical structure information, but for the limited baselines and frequencies available with TOPSAR, a homogeneous vegetation model is adopted, in which the functions of  $z$  in (2) are assumed to be spatially constant. For the homogeneous model, the complex cross-correlation becomes:

$$\begin{aligned} \langle E(\vec{R}_1)E^*(\vec{R}_2) \rangle &\approx A^4 e^{i\phi_0(z_0)} \int_0^{2\pi} W_\eta^2(\eta-\eta_0) d\eta \int_{-\infty}^{\infty} W_r^2(2r'_1) r_0 e^{i\alpha_r r'_1} dr'_1 \\ &\times \int_0^{h_v} e^{i\alpha_z z'} \rho_0 \langle f_b^2 \rangle \exp \left( \frac{-2\sigma_x(h_v - z')}{\cos \theta_0} \right) dz' \end{aligned} \quad (4)$$

where  $\langle f_b^2 \rangle$ ,  $\text{Im} \langle f_f \rangle$ , and  $\rho_0$  are now taken to be constant. For current baseline-frequency combinations, the homogeneous model is expected to work well for many vegetation layers, as indicated in the reference. Now the three unknown parameters in Equation

(4) are 1)  $h_v$  the vertical extension or depth of the vegetation, 2)  $z_0$  the altitude of the ground surface (taken to be the lower edge of the homogeneous vegetation layer), and 3)  $\sigma_x$  the extinction coefficient, defined as

$$\sigma_x \equiv \frac{4\pi\rho_0 I m < f_f >}{k_0} \quad (5)$$

and is a measure of the power loss per unit length into the vegetation layer.

The amplitude of the normalized cross-correlation, which is

$$C_N \equiv \frac{< E(\vec{R}_1) E^*(\vec{R}_2) >}{\sqrt{< |E(\vec{R}_1)|^2 > < |E(\vec{R}_2)|^2 >}} \quad (6)$$

due to vegetation is shown in Figure 3, for the Seven Mile Island area of the Bonanza Creek Experimental Forest (BCEF). Effects due to noise and correlation loss over the range resolution cell have been removed, as described in the reference. The areas marked "CC" in Figure 3 are clear cuts, those marked "WS" are white spruce, and those marked "BP" are balsam poplar. From Figure 2 and the discussion following it, it is expected that the cross-correlation amplitude should decrease (be blacker in the Figure) with increasing vegetation height. It can be seen that the clear cuts are whiter than the vegetated areas. In order to assess the sensitivity of INSAR to vegetation depth differences, note that the stand WS23 (ground-truth height  $\approx 12\text{m}$ ) is clearly brighter than WS5 (ground-truth height  $\approx 21\text{m}$ ). It is fair to expect that parameter estimation of  $h_v$  may ultimately exhibit few-meter accuracy.

In an analysis in Treuhaft et al., 1995, which used ancillary extinction coefficient data to compensate for the underdetermination of parameters mentioned above, forest layer depths  $h_v$  were estimated from the BCEF data. The large regions, a few hundred meters on a side, shown in Figure 3 were used to estimate vegetation layer depths. Figure 4 shows the  $h_v$  results versus ground-truth tree height for two sets of extinction coefficients, one appropriate for frozen conditions and one for thawed conditions. Although the INSAR data were taken in the summer of 1993, and  $h_v$  estimates should have been more accurate using thawed  $\sigma_x$  values, the opposite is true. Several reasons for the improved results (closer to the  $y=x$  line) with the frozen  $\sigma_x$ 's are given in the reference. These reasons include instrumental correlation losses, which would cause  $h_v$  estimates to be too large, and the tendency of vegetation gaps to lower the effective extinction coefficient. Nonetheless, Figure 4 suggests that few-meter vegetation depth estimation may be possible in the near future. Sensitivity analyses suggest that the same accuracy can be obtained for the underlying surface topography, and that 0.1 db/m accuracy may be achievable for the extinction coefficient estimates, for sufficiently tall vegetation.

In another demonstration which is not yet fully analyzed, multibaseline TOPSAR data were acquired by using the so-called "ping-pong" mode. It can be shown that, while the usual TOPSAR 2.5-m baseline is obtained when a signal is transmitted at one end of the baseline and received at the 1 and 2 ends, an effective 5-m baseline can be obtained if transmission *and* reception occurs at both ends of the baseline. Multibaseline, multifrequency ( $L$  and  $C$  band) data from the BOREAS Southern Test Site near Prince Albert, Canada, and the Kellogg site in Michigan were acquired and processed. Preliminary results indicate that the three parameters  $h_v$ ,  $z_0$ , and  $\sigma_x$  can be estimated from the multibaseline INSAR

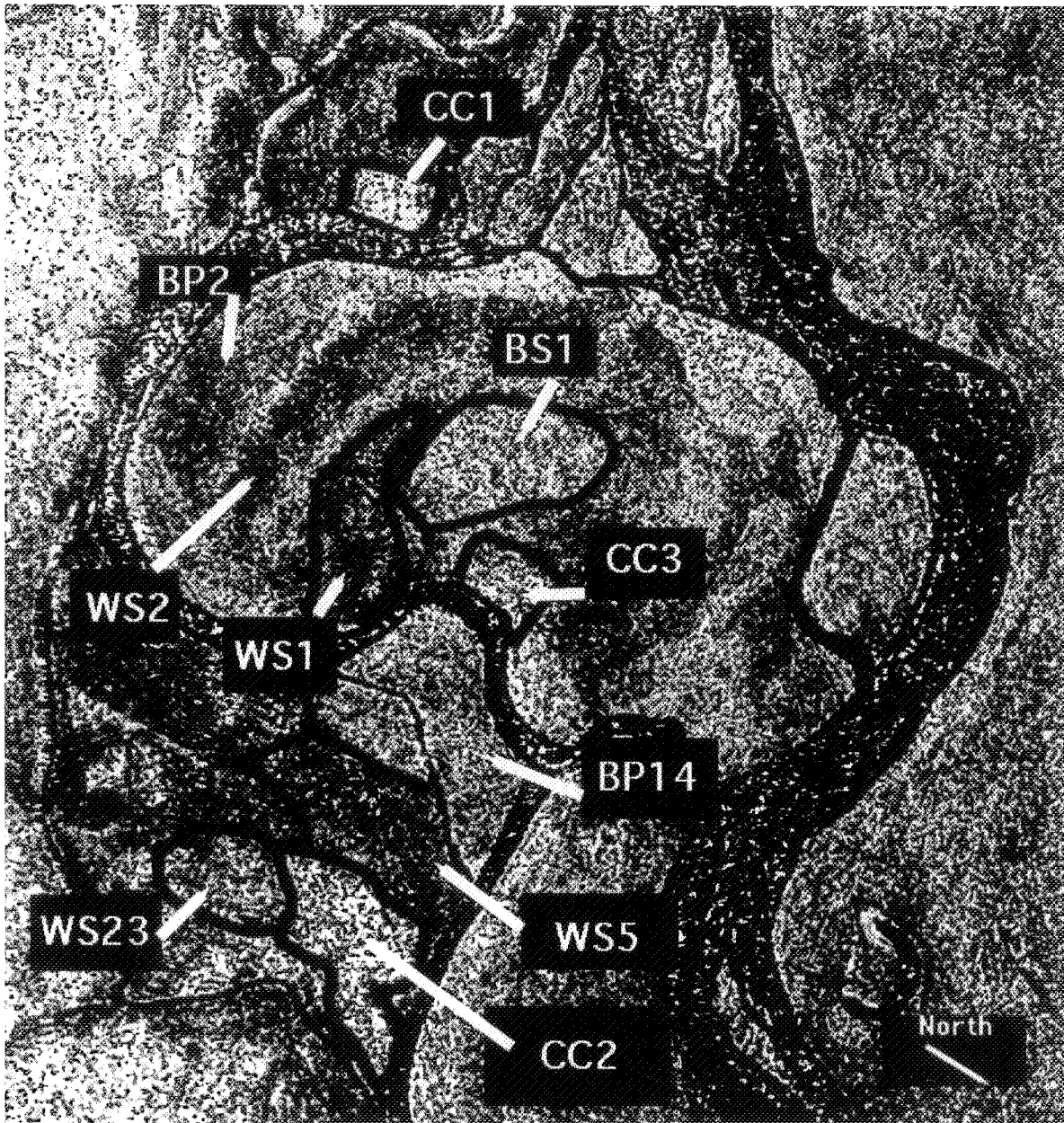


Figure 3: The normalized cross-correlation for the 7-Mile Island Area of the BCEF, corrected for correlation loss due to noise and finite range resolution

data alone, but only for very steep incidence angles  $< 30^\circ$ , and there appear to be systematic errors at the 10-m level for  $h_v$  currently under investigation. Longer baseline pairs, for example 5 and 10-m baselines, may be better suited to accurate parameter estimation. The terrain selected for both demonstrations was flat, in order to avoid the complication of removing the correlation effects induced by surface slopes [Rodriguez and Martin, 1992] before estimating vegetation and surface parameters.

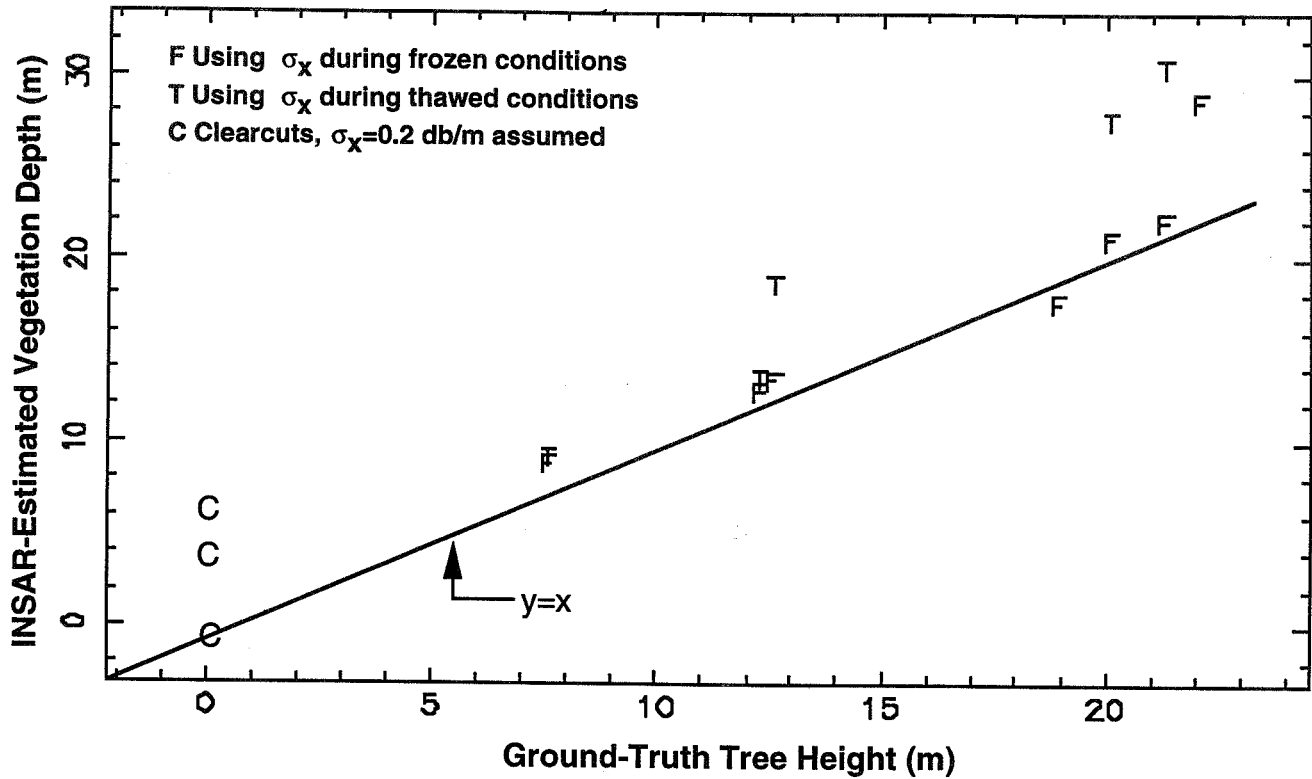


Figure 4: INSAR-estimated vegetation depths versus ground-truth tree height.

#### 4. Combining the Information Content of INSAR and Infrared/Optical Data

INSAR and infrared (IR)/optical data have complementary sensitivities to vegetation characteristics, and may therefore be profitably combined in vegetation parameter estimation. For example, for shallow ( $h_v \leq 10\text{m}$ ) vegetation layers, the INSAR determination of the extinction coefficient and  $h_v$  is poor. This is because INSAR relies on the vertical diversity of returns to determine correlation amplitude and phase, from which the two parameters are inferred. When the vertical diversity is restricted for shallow layers, the extinction coefficient and the  $h_v$  parameters become highly correlated and their accuracy can be compromised. IR and optical techniques are also sensitive to the extinction coefficient [e.g. Myneni et al., 1989], and it is possible that the extinction coefficient could be inferred from spectral rather than geometric signatures. In that case, it may be possible to use extinction coefficient information from the IR/optical data to infer vegetation densities through (5), and also appropriately transform the imaginary part of the average scattering coefficient to radio frequencies. If it were possible to determine the radio extinction coefficient from the IR/optical data as suggested above, introduction of the radio extinction coefficient into the INSAR analysis would enable much more accurate determination of vegetation depth,  $h_v$ . This is an example of a potential combination of INSAR and IR/optical data which would yield more than either data type could supply separately.

## 5. Summary

Homogeneous vegetation layer modeling enables the description of the INSAR response to vegetation in terms of three parameters, the layer depth, the extinction coefficient, and the altitude of the underlying ground surface. With many baselines and frequencies, modeling the INSAR cross-correlation could enable more-detailed extraction of the vertical profiles of vegetation. With current TOPSAR data over the BCEF, a demonstration using ancillary extinction coefficient data showed few to 10 meter agreement in the estimated vegetation layer depth. Another demonstration using multibaseline, multifrequency TOPSAR data over the Boreal forests and over the Kellogg site is in progress. In the future, combining INSAR observations with infrared and optical remote sensing in a unified parameter estimation scenario may yield much more complete information about vegetation layers and underlying topography.

## Acknowledgment

The research described in this paper was carried out by the Jet Propulsion Laboratory, California Institute of Technology, under contract with the National Aeronautics and Space Administration.

## References

- Graham, L. C., "Synthetic Interferometer Radar for Topographic Mapping," *Proc. IEEE*, **62**, 763-768, 1974.
- Manning, G., Massie M., and Rudd, J., "Metric Single-Tree Weight Table for the Yukon Territory," *Information Rept.*, **BX-X-250**, Canadian Forestry Service, Pacific Forest Research Centre, Victoria, B.C., 1984.
- Myneni, R. B., Asrar, G., and Kanemasu, E. T., "The Theory of Photon Transport in Leaf Canopies," in *Theory and Applications of Optical Remote Sensing*, ed. Ghassem Asrar, Wiley and Sons, New York, 1989.
- Rodriguez, E. and Martin, J. M., "Theory and Design of Interferometric Synthetic Aperture Radars," *IEE Proceedings-F* **139**, 147-159, 1992.
- Treuhaft, R. N., Madsen, S. N., Moghaddam, M., and van Zyl, J. J., "Interferometric Remote Sensing of Vegetation and Surface Topography," submitted to *Radio Science*, 1995.
- Vogelmann, J. E. and Rock, B. N., "Use of Thematic Mapper Data for the Detection of Forest Damage Caused by the Pear Thrips," *Remote Sens. Environ.*, **30**, 217-225, 1989.
- Wessman, C. A., Aber, J. D., Peterson, D. L., and Melilo, J. M., "Remote Sensing of Canopy Chemistry and Nitrogen Cycling in Temperate Forest Ecosystems," *Nature*, **335**, 154-156, 1988.
- Zebker, H. A., et. al., "The TOPSAR Interferometric Radar Topographic Mapping Instrument," *IEEE Transactions on Geoscience and Remote Sensing*, **30**, 1992.

**WIDEBAND INTERFEROMETRIC SENSING AND IMAGING POLARIMETRY -- and its  
Relevance to Wide Area Military Surveillance and Environmental  
Monitoring of the Terrestrial and Planetary Covers\***

**James Salvatore Verdi, Otto Kessler\* and Wolfgang-Martin Boerner\*\***

**Naval Air Warfare Center, Aircraft Division, Warminster**

**NAWC-AD-WAR Mission Avionics Advanced Sensors**

**NAWC-P.3-UWB-TOPIF'E-POLSAR Program, Code 45.552**

**Street and Jacksonville Roads, 2018**

**WARMINSTER, PA / USA 18974-0591**

**T/F: +[1](215)441-1422/7281**

**\* Currently with:**

**ONR-European Liaison Office**

**223 Marylebone Road**

**LONDON NW1-5TH, ENGLAND, UK**

**ATTN: Assoc. Dir., ONR-EO/CCS-ST**

**T/F: +[44](171)514-4963/723-6359**

**\*\* Otherwise with:**

**UTC-EECS/CSN, M/C 154**

**900 W. Taylor, SELW-4210**

**CHICAGO, IL / USA 60607-7018**

**ATTN: Dir. Comm., Sens. & Nav. Lab.**

**T&F: +[1](312)996-5480**

**Abstract:** 'WISIP: Wideband ( $\mu$ Hz - PHz) Interferometric Sensing and Imaging Polarimetry' has become an important, indispensable tool in wide area military surveillance and global environmental monitoring of the terrestrial and planetary covers. It enables dynamic, real-time optimal feature extraction of significant characteristics of desirable targets and/or target sections with simultaneous suppression of undesirable background clutter and propagation path speckle at hitherto unknown clarity and never before achieved quality. 'WISIP' may be adopted to the Detection, Recognition and Identification (DRI) of any stationary, moving or vibrating target or distributed scatterer segments versus arbitrary stationary, dynamically changing and/or moving geo-physical/ecological environments, provided the instantaneous  $2 \times 2$  phasor (Jones/Sinclair) and  $4 \times 4$  power density (Mueller/Kennaugh) matrices for forward-propagation/backward-scattering, respectively, can be measured with sufficient accuracy. For example, the DRI of stealthy, dynamically moving and/or camouflaged stationary objects occluded deeply into heterogeneous stationary and/or dynamically moving inhomogeneous volumetric scatter environments such as precipitation scatter, the ocean sea/lake surface boundary layers, the littoral coastal surf zones, pack-ice and snow or vegetative canopies, dry sands and soils, etc., can now be successfully realized. A comprehensive overview is presented on how these modern high resolution/precision, complete polarimetric coregistered signature sensing and imaging techniques, complemented by full integration of novel navigational electronic tools, such as DGPS, will advance electromagnetic vector wave sensing and imaging towards the limits of physical realizability. Various examples utilizing most recent image data take sets of the ~~NAWC/ERIM-P3-UWB-TOPIF'E-CATI/LTBL-~~ **POLSAR** and ~~NASA-JPL-AIRSAR~~ **airborne**, the ~~NASA/DARA/DASI-SIR-C/X-SAR~~ **shuttle**, and the ~~ESA ERS-1/2~~ **satellite** imaging systems will be presented for demonstrating the utility of WISIP.

**Page intentionally left blank**

**GeoSAR**  
**A Radar Based Terrain Mapping Project**

Robert Yoha \*  
California Department of Conservation  
801 K Street, M/S 12-50  
Sacramento, CA 95814  
E-mail: ryoha@consrv.ca.gov

**1. BACKGROUND**

GeoSAR is a project to develop a commercial airborne, radar-based, terrain mapping system utilizing technology originally developed by NASA and ARPA for commercial and defense applications. The project team consists of the Sensor Technology Office within the Federal Government's Advanced Research Projects Agency (ARPA), NASA's Jet Propulsion Laboratory (JPL) at the California Institute of Technology, Calgis Inc. a California business, and the California Department of Conservation (DOC) which brought together the GeoSAR team. GeoSAR has three primary goals.

1. Validation of radar terrain mapping technology developed by NASA-JPL and ARPA.
2. Application of this technology to seismic hazards and environmental mapping for the Department of Conservation and other governmental agencies.
3. Demonstration of commercial marketability via end-user projects using real world problems and applications.

**2. MULTI-YEAR PROJECT**

The work plan is a 4 year end-user driven application and systems development and verification process, with the final goal being commercialization of the technology to serve the end-user community. Year 1 efforts focused on accuracy assessment for both terrain modeling and land cover analysis. Year 2 efforts are now focusing on development of foliage penetrating (FOPEN) capabilities for mapping true ground surface and expanding end-user applications. Years 3 and 4 will concentrate on systems' development and commercialization.

**3. YEAR 1 - OVERVIEW OF ACTIVITIES**

Year 1 began in the spring of 1994 and focused on end-user experiments designed to test and validate interferometric synthetic aperture radar (IFSAR) mapping capabilities using data acquired from JPL's airborne TOPSAR (Topographic Mapping Synthetic Aperture Radar) instrument flown aboard the NASA/JPL DC-8 research aircraft.

A ground campaign was conducted to establish geodetic control, set radar reflectors, and acquire ground truth for four test sites. The sites were chosen to represent environmental mapping problems from DOC programs that could be solved using a GIS (geographic information system) enhanced with radar mapping technology. JPL oversaw flight planning, acquired, and processed the TOPSAR radar data. Calgis led the ground campaign and provided end-user support. DOC provided end-user input, and conducted application and verification tests.

---

\* This paper is in part excerpted from the GeoSAR Year 1 Research and Development Status Report, prepared for the Advanced Research Projects Agency, by the: California Department of Conservation, Sacramento, California; the Radar Sciences Section, Jet Propulsion Laboratory, Pasadena, California; and, Calgis Inc. Fresno, California.



Between May and July 1994, JPL conducted three TOPSAR flights that acquired radar data over five sites.

- Antioch Hills in the Sacramento Delta area serves as a super site for three end-user experiments continuing into Year 2 : (1) digital elevation model (DEM) verification; (2) slope hazards assessment; and, (3) land use and land cover analysis.
- Laurel Quad, north of the town of Santa Cruz; is the primary site for foliated landslide mapping efforts initiated in Year 1. With the bulk of FOPEN image and DEM analysis following in Years 2 and 3.
- North fork of the Gualala River along California's north coast, for slope erosion analysis in a timber harvest site. This data was acquired for work planned to follow in Year 2.
- The abandoned Iron Mountain Mine west of the town of Redding needs abatement of contaminated runoff. Initial data was acquired in Year 1 for work planned to follow in Year 2.
- An unforeseen opportunity developed to acquire a fifth TOPSAR terrain data set over the San Fernando Valley after the January 1994 Northridge earthquake. The mosaiced IFSAR DEM is presently being evaluated for use in a FEMA/DMG seismic hazards mapping effort.

TOPSAR radar data was processed by JPL for the Antioch Hills and Laurel Quad sites. The data were processed into three standard products: a radar-derived DEM with 5m horizontal postings; an orthorectified SAR image; and, a correlation map. The processed data were recompiled by Calgis and provided to DOC for end user experiments and analysis. Calgis developed software to transform the data from its spherical system of radar mapping coordinates used by JPL to the cartographic map projections and GIS format used by DOC.

DOC conducted three end-user experiments, two in the Antioch Hills and one for the Laurel Quad test site, with JPL and Calgis providing technical support. DOC's Division of Mines and Geology (DMG) Seismic Hazards Evaluation and Zonation Project (SHEZP) conducted a non-vegetated DEM and slope hazards experiment in the grass covered rolling slopes of the Antioch Hills and, initiated a vegetated DEM and slope hazards assessment in the heavily forested mountainous Laurel Quad, with analysis of FOPEN technology planned for Year 2. The Farmland Mapping and Monitoring Program (FMMP) conducted a land use and land cover experiment in the urbanized and farmed region of the Antioch Hills that is planned to be continued into Year 2 for a change detection experiment.

#### 4. ANTIOCH HILLS DIGITAL ELEVATION MODEL RESULTS - YEAR 1

The IFSAR-derived DEM for Antioch Hills was found to be have a greater accuracy than the U.S. Geological Survey (USGS) 7.5 minute quadrangle based DEMs currently available for California. Results indicate that a more detailed and more precise analysis of terrain geometry may be possible using a radar-derived DEM than with a public domain USGS DEM. Another benefit that radar-based DEM production may demonstrate is increased production and reduced turnaround time compared to existing methods, this is being studied in Year 2.

A highly precise DEM was constructed using soft copy photogrammetry and 1:10,000 scale aerial photography acquired for a detailed test area, to serve as ground truth and for analysis of the radar-derived DEM. SHEZP and Calgis determined a worst case standard deviation of 4.5m vertical which makes the radar-derived DEM suitable for creating maps with contour intervals of 15 to 20m. Horizontal ground resolution was found to be a factor of 6 times greater or 36 times the data density compared to a standard USGS DEM. These results were obtained according to National Map Accuracy Standards and procedures based on using a planimetric reference frame from an end-user's approach.

In order to evaluate the TOPSAR data from a sensor performance perspective, JPL performed a precise co-registration of a Calgis constructed soft copy-derived photogrammetric reference DEM to the TOPSAR generated DEM. After removal of systematic miss registration errors that resulted from incomplete calibration of the TOPSAR instrument, JPL found a better level of RMSE accuracy by about 1m. This indicates that the TOPSAR instrument was performing as expected and after additional calibration, may ultimately permit attaining the target goal of 2 to 3m vertical accuracy with a 5m horizontal grid.

## **5. ANTIOCH HILLS LAND USE AND LAND COVER RESULTS - YEAR 1**

The IFSAR-derived ortho-rectified image for Antioch Hills was found to have an improved spatial accuracy over that of commercially available satellite imagery. A multi-sensor approach of combining the IFSAR data with spectral satellite imagery showed potential for improved mapping of agricultural land use change and urbanization in California.

The usefulness of radar imagery as an enhancement to multi-spectral satellite imagery was demonstrated in a comparison of four intensity, hue and saturation (IHS) enhanced images developed by FMMP and Calgis. Identification of urban, dry vegetation, and marsh land categories was improved by substituting an average of Thematic Mapper (TM) and radar principle component (PC1) for intensity in an IHS to red-green-blue (RGB) conversion, compared with using TM intensity alone. Discernment amongst dry vegetation categories was 25% closer to true ground control with the combined radar/TM compared to TM alone. However, the radar/TM combination effected a 15% decline in the ability to discern irrigated agricultural categories compared to TM. Enhancement techniques to reduce inherent noise and over saturation effects in the radar magnitude image are being pursued as part of Year 2 efforts.

Precision point placement tests indicate that the Antioch Hills radar imagery had the highest spatial accuracy compared to commercial satellite imagery, and would be suitable for FMMP's registration requirements for mapping farmland and urbanization. The 5m radar pixel makes it possible to discern FMMP's 4 hectare minimum mapping unit which must be measurable in 0.8 hectare increments for mapping and reporting agricultural and urban land use changes.

A five class automated land use and cover classifier (AutoMAP) was developed and demonstrated by JPL. Comparison between control land use and the automated classifier results was inconclusive concerning which band combinations were the most accurate for automated land use mapping. The inherent differences between the land use classes employed by FMMP and the JPL automated classifier classes necessitate further work which is being investigated by FMMP in Year 2.

## **6. YEAR 2 - OVERVIEW OF ACTIVITIES**

Year 2 has an expanded scope of work in conjunction with verifying a broader range of applications while avoiding duplication of effort. JPL is focusing on development of FOPEN techniques for mapping true ground surface using improvements to the TOPSAR instrument and the DC-8 aircraft inertial navigation system. In addition, polarimetric data is being acquired and provided using the JPL AIRSAR instrument. Calgis is continuing to provide ground truth, photogrammetric and remote sensing assistance, along with development of a AIRSAR to GIS convertor.

Efforts continue with Antioch Hills and Laurel Quad, work on Iron Mountain has been initiated. Application expansion and avoiding duplication necessitated discontinuing work on Gualala River. In addition to DOC's internal projects, end-user application has been expanded to include other state and local government agencies, and university researchers.

To broaden the scope of application testing and verification, seven new sites involving ten cooperators have been added under the oversight of DOC. Under ARPA's direction, data from the Environmental Research Institute of Michigan (ERIM) X-band IFSAR-E and the Naval Research Laboratory (NRL) P-3 aircraft UHF/VHF sensors has been made available for use in Year 2.

**Table 1. Year 2 Expanded Applications**

Site	Sensor	End User	Purpose
Camp Creek	JPL-TOPSAR	UC Davis, Sierra Natural Ecosystems Project	forest ecosystem study
Elk Horn Slough	JPL-TOPSAR	Moss Landing Marine Labs, Coastal Commission	estuarine ecosystem study
Big Sur	JPL-TOPSAR	California Department of Transportation	coastal highway slope failure
Camp Roberts	ERIM-IFSAR-E	California Army National Guard	forest fire and range management
Guadalupe Dunes	NRL-P3	DOC Division of Oil and Gas	mapping buried oil pipelines
Upper Santa Clara Rive	ERIM-IFSAR-E	Los Angeles County Dept. of Public Works	flood plain assessment
Lower Santa Clara Rive	ERIM-IFSAR-E	Ventura County Flood Control Department	flood channel erosion control
Callegaus Creek	ERIM-IFSAR-E	Ventura County Flood Control Department	hydrologic runoff planning

Systematic errors due to a byte-slip and multi-path interference were noted in the preliminary shipments of Year 2 TOPSAR imagery. JPL has developed new calibrations and is reprocessing the first data sets that were delivered in 1995. Changes in delivery schedules have lead to modification of planned workflow. The primary components of the project have continued despite slipping the original plans.

As a follow-up to Year 1 DEM investigations in the Antioch Hills, SHEZP will be completing its non-foliated terrain comparison of the TOPSAR DEM to conventional, large-scale mapping products, which include a 1:40,000 scale photogrammetric DEM, a USGS DEM, and a DEM produced by SHEZP using the USGS 7.5 minute quadrangle topographic map. A slope algorithm optimal for use on the TOPSAR DEM in non-foliate terrain is also under development. A time, cost, and effectiveness study of the various available DEMs compared to using radar for DEM construction is being done. Pending progress, SHEZP intends to analyze JPL's preliminary FOPEN DEM and associated data sets for accuracy and suitability for use in slope failure assessment.

Also as a follow-on to its Year 1 land use mapping work in the Antioch area, FMMP is developing an improved automated multi-sensor classification workflow, and is improving on computing the accuracy of automated classification maps vis-a-vis ground truth. This analysis involves the rasterization of ground truth information and a grid-based comparison expanded to the entire study area. Modifications to this workflow allow for an improved assessment of the JPL AutoMap classification results. Refinements to accuracy assessment procedures will provide a more complete perspective on the values of various image enhancement techniques. FMMP will also be working on orthorectification of 1994 and 1995 imagery for improved ground truth maps, generation of land use conversion statistics between the two dates, and a general review of polarimetric data and other products acquired for the Antioch area.

The Office of Mine Reclamation has initiated work for Iron Mountain, intensive ground truth has been accomplished. Calgis acquired close-range photogrammetric images for two areas approximately 100m x 200m each at the base of the large waste rock fan. Close-range photogrammetry stereo-models will be utilized to produce high resolution DEMs as well as for ground truth for RMS height variations -- comparisons will be made to the radar roughness signature. It is planned to compare hydrologic simulation runs using a USGS DEM as a base versus the FOPEN L-band radar DEM. Comparison will be based on adequacy of development of drainage patterns and development of rivers and streams.

## 7. CONCLUSIONS

Results of the first year's efforts have shown that IFSAR can be employed for terrain and land use analysis in an environmental setting. A valuable future topic is the development of automated landslide hazards and land use change detection algorithms using radar-derived DEMs and images. There exists the possibility to train the computer to recognize landslide features using this much more precise radar DEM. Such a capability would significantly expedite the process of landslide inventory, quickly covering large areas, identifying candidate landslide features and allowing the analyst to concentrate on making final judgment calls. Along similar lines, radar-derived automated land use and cover change detection warrants additional investigation. Additional work is necessary to evaluate the economics of cost, time, and accuracy of existing systems be compared to using radar for DEM construction, and as a part of a multi-sensor approach to land use mapping.

## 8. ACKNOWLEDGMENTS

GeoSAR is supported by the Advanced Research Projects Agency, Sensor Technology Office. Dr. Scott Hensley, JPL, deserves special mention for his efforts which exemplify the work of the Radar Sciences Section. Though they are not mentioned here, others of the GeoSAR team such as the DC-8 aircraft crew and TOPSAR staff, along with numerous others in DOC and Calgis participated in this project and also deserve credit. The following contributed to the research described in this paper.

### CA DEPARTMENT OF CONSERVATION

Dr. John Burton

Integrated GeoData Management Unit  
Robert Yoha

Seismic Hazards Evaluation & Zonation Project  
Charles Real  
Rick Wilson  
Tim McCrink  
Emily Oatney  
Wayne Hayden  
Chris Wills

Farmland Mapping & Monitoring Program  
Molly Penberth

Office of Mine Reclamation  
Kit Custis

Timber Harvest Review Project  
Tom Spittler  
MaryAnn McKittrick

### JET PROPULSION LABORATORY

Dr. Scott Hensley  
Dr. Jeff Klein  
Dr. Frank Webb  
Dr. Theierry Michel  
Dr. Ernesto Rodriguez  
Dr. Bijan Houshmand  
Dr. Thomas Thompson

### CALGIS

Gerald Dildine  
Dr. Mushtaq Hussain  
Dr. Riad Munjy  
Dr. Jack Paris  
Jeffery Seib  
Chris Bohain